2012

Microfabrication of conductive polymer nanocomposite for sensor applications

Chaoxuan Liu
Louisiana State University and Agricultural and Mechanical College

MICROFABRICATION OF CONDUCTIVE POLYMER NANOCOMPOSITE FOR SENSOR APPLICATIONS

A Dissertation

Submitted to the Graduate Faculty of the
Louisiana State University and
Agricultural and Mechanical College
in partial fulfillment of the
requirements for the degree of
Doctor of Philosophy

in

The School of Electrical Engineering and Computer Science

by
Chaoxuan Liu
B. E., Huazhong University of Science and Technology, 2006
M. S., Louisiana State University, 2008
December 2012

ACKNOWLEDGEMENTS

I would like to express my deepest gratitude to my advisor Dr. Jin-Woo Choi, who has been a great mentor for me in the past 6 years of my graduate study. I am thankful for his tireless guidance and support that made this research possible.

Also, I would like to thank my committee members Dr. Georgios Veronis, Dr. Michael Murphy, Dr. Sunggook Park, and Dr. Rajgopal Kannan for their valuable time and contribution to my research. I am grateful for my research colleagues Edward Song, Charles Bryan, Adey Abera, Fang Liu, Haichen Zhu, Guocheng Shao, and many others for the valuable discussions, collaborations, and friendship we have experienced.

Above all, I owe everything to God and my beloved family.

TABLE OF CONTENTS

LIST OF TABLES

LIST OF FIGURES

ABSTRACT

This dissertation developed novel microfabrication techniques of conductive polymer nanocomposite and utilized this material as a functional element for various physical sensor applications. Microstructures of nanocomposite were realized through novel microcontact printing and laser ablation assisted micropatterning processes. Prototype devices including large-strain strain sensor and highly-sensitive pressure sensor were demonstrated showing distinct advantages over existing technologies.

The polymer nanocomposite used in this work comprised elastomer poly(dimexylsiloxane) (PDMS) as polymer matrix and multi-walled carbon nananotubes (MWCNTs) as a conductive nanofiller. To achieve uniform distribution of carbon nanotubes within the polymer, an optimized dispersion process was developed, featuring a strong organic solvent—chloroform, which dissolved PDMS base polymer easily and allowed monodispersion of MWCNTs.

Following material preparation, three novel approaches were employed to pattern microstructures of polymer nanocomposite, each of which held respective advantages over previous fabrication techniques. For example, microcontact printing, by using a pre-defined stamp, directly transfers nanocomposite patterns from the ink reservoir to a substrate. Therefore, it eliminates the need of repeated photolithography process for every sample, saving time and cost. For another example, two variations of the laser assisted screen printing technique with micropatterns defined by the programmable laser ablation of a thin polymer film, allowed direct filling of nanocomposite and required only a CAD drawing for each design of sensor sample. Two variations of this fabrication

protocol realized both fully embedded nanocomposite structures in a bulk polymer, as well as protruding relief-patterns of the nanocomposite on a polymer surface.

The sensing capability of the polymer nanocomposite is attributed to the unique combination of mechanical flexibility and electrical piezoresistivity. To demonstrate feasibility for practical sensor applications, two sensor prototypes were constructed. The strain sensor, for example, showed significant resistive response while sample withheld large range tensile strain of over 45%. Also, the fabricated pressure sensor indicated high sensitivity of differential pressure. Each prototype showed distinctive advantages over conventional technologies. Complex hysteresis effects were observed and analyzed regarding the resistance and stress of the nanocomposite, which was followed by discussions of potential polymeric mechanisms.

CHAPTER 1: INTRODUCTION

1.1 Motivation

Microelectromechanical systems (MEMS) technology was primarily developed from microelectronics industry dating back to the 1950s. Over the past 60 years, due to its compatibility with traditional integrated circuit (IC) processes, miniaturization capability, low energy consumption, and high performance as sensors & actuators, MEMS technology has experienced tremendous growth and found various applications in the fields of chemical, biological, electrical and mechanical engineering. Today, the term MEMS applies to all manners of miniaturized devices involving microstructures of one sort or another, often fabricated with techniques derived from the IC industry [1].

1.1.1 MEMS-based sensors

Sensor is a device that measures a physical or chemical quantity (e.g. temperature, pressure) and produces a signal which can be read by an observer or by an instrument. Sensors have been a driving force for the development of MEMS since its very start. In 1954, a stress-sensitive effect in silicon and germanium termed piezoresistance was discovered by Smith [2]. In the following year Paul and Pearson demonstrated the possibility of a pressure sensor using the piezoresistance of silicon [3]. During the early 1960s, a series of papers described the first strain gauge [4] and pressure sensor [5]. From that point forward, the interest of developing sensors has spurred on. To date, the development of sensors has been very successful especially in the physical sensing context, yielding a wide range of small, rugged and inexpensive devices. Exemplary

physical sensors include, but are not limited to, accelerometer, strain gauge, stress sensor, air mass flow sensor, pressure sensor, gyroscope, and so forth. Therefore, it can be concluded that physical sensors have been an essential integral part of MEMS technology.

As successful as silicon-based MEMS sensors have been in the commercial market, there may exist certain inherent limitations to this sensing format. Due to the mechanical properties of silicon and other conventional sensing materials, it could not meet the requirement of certain applications. For example, the sensing of biomechanical strains in biomedical field could mandate the strain gauge to withstand large ranges of strain—over 20% in some cases [6], which is difficult for silicon-based sensors. Also, in this area it would be desirable to use fully biocompatible sensing material as implantable medical devices. Furthermore, the rigidity of material such as semiconductors could limit its sensitivity as minute changes in its sensing parameter may not induce as a significant response as a "soft" material would. To address these issues, a different class of material—polymer nanocomposite could provide potential solutions.

1.1.2 Conductive polymer nanocomposite

MEMS systems are generally composed of metal, semiconductor, polymer and other materials. Compared with other classes of materials, polymer owns distinct advantages as it possesses a great variety of material characteristics (e.g. mechanical flexibility, optical transparency, biocompatibility, chemical stability, etc.) enabling it to be used in diverse applications such as microfluidic systems and bio-implantable systems. Polymer can be produced in huge volumes thanks to the development in its manufacturing industry. Also, MEMS devices can be readily made from polymer by processes such as cast molding, injection molding, hot embossing and photolithography.

However, due to lack of electrical conductivity in most polymers, the role of this material has been limited to a structural component in most applications. Often polymer-based MEMS devices require conductive elements to electrically control or collect signals from systems. While metal suffers coherent incompatibility issues with polymers, a mixture of polymer and nano-scaled fillers—termed nanocomposite provides an alternative of incorporating conductivity into polymer systems. This class of material is unique in the sense that it retains many desirable features of polymers (flexibility, biocompatibility, processability) yet adds electrical conductivity and/or piezoresistivity from the nanofiller which is not an intrinsic property of most polymers. By utilizing polymer nanocomposite, components such as conductive electrodes and sensor elements could be incorporated into conformal all-polymer systems.

1.1.3 Microfabrication of polymer nanocomposite

Although conductive polymer nanocomposite is useful in its bulk form for conventional "large" systems (with feature size > 1 mm), in order to effectively work as functional elements in MEMS systems which have feature size on the microscale, it needs to be capable of being fabricated into 3-D microstructures. Microfabrication of metallic patterns, a popular and well-established technique in microelectronics, is found to be difficult to translate into the micropatterning of polymer nanocomposite. Unlike metal which can be selectively covered by photoresist and readily etched by either physical ions or chemical developer, for instance, solidified polymer nanocomposite lacks chemical agent in which its exposed portion can be selectively dissolved.

In the past few years, several approaches have been explored by researchers to pattern polymer nanocomposite into microstructures. For example, standard photolithography

and manual filling/removing of nanocomposite were utilized to form micropatterns [7–10]. While feasibility was demonstrated, this procedure required repetition of whole lithography process and could not ensure complete removal of excessive nanocomposite. In another approach, photosensitive chemical agents were added into the conductive nanocomposite converting it into a photopatternable resist [11]. Regardless of inspiration idea, the addition of chemical agents and their development during photolithography could alter the properties of polymer nanocomposite. Likewise, repetition of whole steps was still necessary for each new pattern generation.

To overcome these drawbacks, this study aims to introduce alternative approaches to realize reliable micropatterning of conductive polymer nanocomposite. Time consumption and cost are expected to be significantly reduced, as fabrication process is simplified. Using proposed fabrication protocols, lab prototyping of various physical sensor types and designs is to be implemented and characterized.

1.2 Objectives

As mentioned above, conductive polymer nanocomposite could overcome many inherent limitations of conventional semiconductors. With this sensing material, sensors could be produced with biocompatibility, improved sensitivity and operating range. Innovative applications could be explored which would not have been possible with silicon-based sensors, offering new possibilities in fields such as Biomedical MEMS (or BioMEMS which deal with measurement or analysis of biological and biomedical matters), chemical engineering, medical diagnosis, security systems, etc.

1.2.1 Preparation of conductive polymer nanocomposite

The first and foremost step of realizing sensor devices is to prepare a homogenous polymer nanocomposite in which conductive nanofillers are evenly distributed throughout the 3-D space of polymer matrix. This is important for ensuring the consistency of electrical conductivity of nanocomposite. Especially for MEMS-based sensor devices where micropatterns are mandatory, it is crucial to obtain a uniform dispersion of nanofillers. In case of uneven dispersion, the micro-sized clusters formed by the aggregation of nanofillers could affect the current conduction path. For a microstructure, this impact could be more severe than a bulk material.

Because of superior mechanical flexibility and electrical piezoresistivity, the polymer nanocomposite chosen in this study consists of elastomer poly(dimexylsiloxane) (PDMS) as matrix and multi-walled carbon nananotubes (MWCNTs) as filler. A uniform dispersion of carbon nanotubes (CNTs) within polymer is achieved with the assist of a strong organic solvent which dissolves the polymer base easily and allows monodispersion of CNTs. Dispersion process mainly includes the exposure of excessive volume of organic solvent to agitation mechanisms (sonication, mechanical stirring and/or shear mixing, etc.), followed by complete evaporation of the solvent. Efforts are concentrated to optimize processing conditions, such as the selection of common solvent, determining sequence and time of different agitation methods and solvent drying conditions. Nanocomposites containing varying loading percentages of carbon nanotubes are tested, accompanied with characterization of their electrical and mechanical properties.

1.2.2 Micropatterning of conductive polymer nanocomposite

As micropatterning is mandatory for polymer nanocomposite to effectively work as sensor components in MEMS devices, another main goal of this study is to develop novel fabrication protocols to improve upon currently reported approaches. Two different patterning methods are presented in this work each owning its respective advantages. Firstly, the microcontact printing technique, by using a pre-defined stamp, directly transfers nanocomposite patterns from the ink reservoir to a substrate. It eliminates the need of repeated photolithography process for every sample, saving time and cost. Secondly, a laser assisted screen printing process defines micropatterns by the programmable ablation of a focused laser beam on a thin polymer film, thus allowing direct filling of nanocomposite into open grooves. This approach requires only a CAD drawing for each new design of sensor device, ideal for lab prototyping work in which various designs usually need to be tested. Both patterning techniques are fully characterized in terms of their process conditions, pattern uniformity, resolution, etc. Post-patterning steps are also described to achieve final sensor devices.

1.2.3 Novel physical sensors based on polymer nanocomposite

The main motivation of this work is to overcome inherent limitations of traditional sensing materials and explore new sensing possibilities utilizing the proposed polymer nanocomposite. Due to the versatility of this material, numerous sensor types can be potentially realized using the microfabrication techniques proposed in this dissertation. For proof of concept, two sensor types are discussed in detail. The strain gauge, for example, reveals significant resistive response while sample undergoes mechanical strain over 45% --a range much higher than metal or semiconductor-based sensors. Also, the

constructed pressure sensor indicates sensitivity of air pressure change as minute as 100 Pa or less—a resolution much higher than previously reported results. The characteristics of resistive response are analyzed, provided with potential solutions to overcome hysteresis effects that are intrinsic to polymers.

Other novel and diverse sensing formats are aimed to be developed from the framework of technology developed here. For example, with integration of microfluidic channels polymer nanocomposite could serve as a potential flow rate sensor; once patterned into grid-like structures inside thin film, it could work as tactile sensor which is capable of mapping pressure difference locally. Lastly, it should be noted that potential applications of polymer nanocomposite are not necessarily limited to sensors. Thermal heater, electric coating layer, circuitry elements (resistor, capacitor and inductor), and so forth are other directions of developing this versatile material.

1.3 Dissertation outline

This dissertation contains six chapters. Chapter 1 presents the motivation and objectives of this research, and introduces MEMS-based sensors. Microfabrication of polymer nanocomposite as novel physical sensors is proposed. Chapter 2 reviews previous and current research related to the use of polymer nanocomposites, particularly nanocomposite composed of carbon nanotubes and PDMS. It describes the dispersion of carbon nanotubes inside a polymer matrix, microfabrication techniques used to pattern polymer nanocomposite, as well as physical sensors that can be developed using this class of material. Chapter 3 describes experimental preparation of polymer nanocomposites. Various dispersion agents and/or approaches are used to reach

homogenous distribution of carbon nanotubes within PDMS. Dispersion qualities under different conditions are characterized, as are electrical properties of prepared nanocomposite samples. Chapter 4 discusses a variety of novel microfabrication techniques used to pattern polymer nanocomposite. Microcontact printing and two versions of laser ablation-assisted screen printing are used in the fabrication process. The pros and cons of each fabrication approach are discussed. Chapter 5 demonstrates physical sensor prototypes including strain sensors and pressure sensors. Significant resistive responses of strain sensor under large tensile strain are illustrated, and hysteresis effects of resistance, stress and strain are discussed. Further, highly-sensitive pressure sensing is demonstrated to show advantages over current sensing formats. Chapter 6 summarizes results and proposes future work.

CHAPTER 2: BACKGROUND

2.1 PDMS-MWCNTs nanocomposite

2.1.1 Why polymer nanocomposite over metal

Metal is an ideal material to use as electrical interconnections because of its unparalleled conductivity. In the microelectronics industry, metallic patterning is a popular and well-established technique. Even in MEMS devices which are based on rigid substrates (semiconductors, glass), micropatterning of metal electrodes is a routine process. Nevertheless, when applied to polymer-based MEMS devices metal often suffers from incompatibility issues. Especially for mechanically flexible elastomers, metallic patterns often lead to poor adhesion due to the low surface energy of elastomeric substrates.

To introduce metallic patterns into polymer-based MEMS systems, several approaches have been reported using, for example, coupling agent to enhance chemical adhesion [12], surface wetting and heating to promote surface adhesion [13–15], serial and selective etching to stack metal layers on elastomer PDMS [16], or manual injection and solidification of melted metals into PDMS microchannels [17]. However, even with improved adhesion, the incompatibility between PDMS and metals may still cause failure in fabrication processes. Thin metallic films tend to detach from flexible PDMS substrates, and thin layers have potential cracking problem when bent or stressed [16], which is undesirable in many flexible electronics applications [18-19].

Polymer nanocomposite, on the other hand, is a soft material that owns properties similar to the intrinsic form of its matrix. Therefore, when microstructures of nanocomposite are attached to or embedded in the same pristine polymer, the interface is tightly secured by chemical bonds between nanocomposite matrix and surrounding polymer molecules. Conformal all-polymer devices can be realized, eliminating potential incompatibility problems.

Polymer nanocomposite also holds another significant advantage over metal and semiconductor when it comes to working as sensing element. Although metallic or silicon-based strain gauges are commercially available and popular in many applications due to their low cost, their usage in certain areas (e.g. as implanted medical devices in the medical field) is limited because of their relatively large size and lack of biocompatibility to offer long-term implantable monitoring of biomechanical strains. On the other hand, polymer nanocomposite offers an alternative to be used as biocompatible strain sensors. Since polymers, especially elastomers, are much more flexible compared to metals, they can sustain higher level of strains. Therefore, for a given displacement (e.g. interfragmentary motion displacement during the healing of bone fracture could be up to a few millimeters [20]), the required dimension for nanocomposite sensors could be relatively smaller—a desirable attribute for miniaturized sensor devices.

2.1.2 PDMS as choice of polymer matrix

Polymer nanocomposite is composed of a thorough mixture of polymer matrix and nano-scale filling materials. To use as the matrix of nanocomposite, there are numerous polymers of diverse properties to choose from, including both plastics and elastomers which are the main two types of polymers. For the purpose of sensing specifically, a good

deal of research effort has been committed to select an appropriate hosting matrix for the nanocomposite. Various polymers such as poly(methyl methacrylate) (PMMA) [21], [22], polycarbonate (PC) [23], poly(ethylene) (PE) [24], poly(L-lactide) (PLLA) [25], etc. have been incorporated with nanofillers to construct strain sensors, which are capable of holding larger tensile strain than conventional metallic strain gauges [26].

Compared with above polymers, silicone-based elastomer poly(dimethylsiloxane) PDMS owns superior mechanical elasticity as it easily holds over 100% of tensile strain without any structural failure [27], making it an ideal choice for large-range strain sensing applications. Its flexibility allows it to be readily attached to curved surfaces, which is often necessary in biomedical sensors. Moreover, PDMS being a chemically inert and biocompatible material is widely used in microfluidics and biomedical areas [28].

2.1.3 Carbon nanotubes as choice of conductive fillers

Since MEMS-based sensors require feature sizes on the microscale, conductive fillers of polymer nanocomposite typically have feature size on the nanometer scale, so that the conformity of microstructures could be ensured. Common nanofillers include carbon nanotubes, carbon black (nanoscaled carbon particles), metal particles and flakes [29]. Amongst these, carbon nanotubes are particularly interesting candidate for sensing applications.

Ever since the discovery of carbon nanotubes by Iijima in 1991 [30], numerous research has been conducted to explore the potentials of this “magic” material [31]. With a high aspect ratio because of its long tubular structure, as illustrated in Figure 2.1, carbon nanotubes demonstrate relatively high electrical conductivity. For example,

compared with other conductive nanofillers (e.g., metal flakes or particles with lower aspect ratios), carbon nanotubes composites of various polymers reach percolation threshold at a lower weight percentage [29, 32]. Probably, tubular structures allow the formation of a more efficient electron-conducting network in CNT-based composite. Also, the piezoresistivity of CNTs make them a suitable candidate for sensors: when a CNT-based composite is exposed to mechanical deformation, the geometry and interconnections of nanotubes within the polymer matrix vary accordingly, which leads to a change in its electrical resistance. Further, CNTs being one of strongest materials known to man, with tensile strength up to 63 GPa using multi-walled carbon nanotubes (MWCNTs) [33], give them another edge over other materials for fabricating robust sensors.

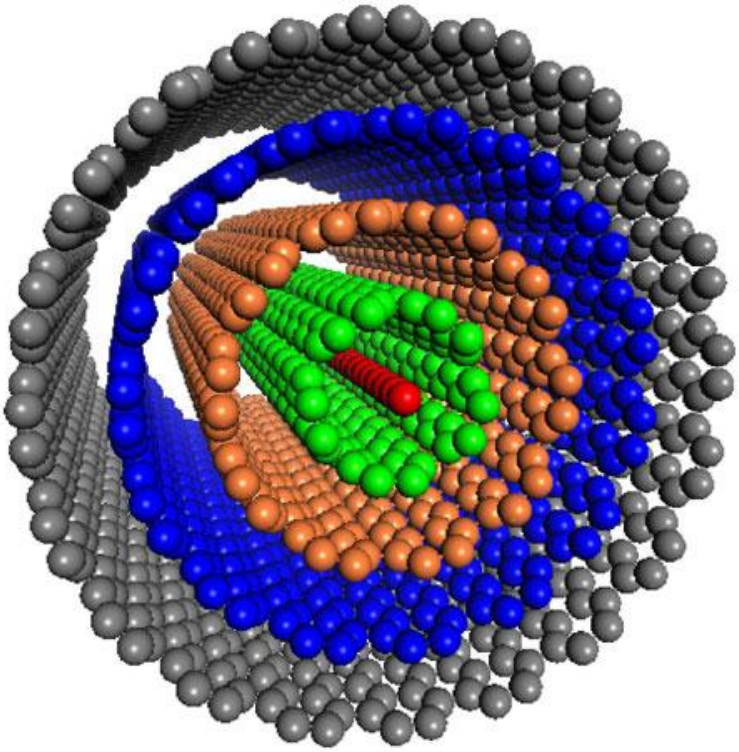

Figure 2.1 Image showing 3-D model of a multi-walled carbon nanotube [34]. Note: a linear carbon chain (red-colored) is inserted in, but not part of, the carbon nanotube.

In this work, multi-walled carbon nanotubes were chosen over single-walled carbon nanotubes (SWCNTs) because MWCNTs generally offer better conductivity [32]. Plus, economic wise MWCNTs generally cost less to purchase (e.g., according to price quote information from Cheaptubes.com on 7/8/2012, 1 gram of 99 wt% SWCNTs costs around $250, while 1 g of similar 99 wt% costs around $25). Thus, MWCNTs were picked as the preferred material over SWCNTs [35].

2.1.4 Dispersion of carbon nanotubes in polymers

Dispersion is a spatial property whereby the individual carbon nanotubes are spread with the roughly uniform number density throughout the continuous polymer matrix. The first challenge is to separate the tubes from their initial aggregated assemblies, which is usually achieved by local shear forces. Direct manual mixing of CNTs with polymer resin, though simplest approach, does not create sufficient local shear force and therefore leads to poor dispersion of CNTs inside polymer matrix.

More effective separation of CNT bundles requires the overcoming of the inter-tube van der Waals attraction [36]. Depending on the tube shape/size and the orientation of nanotubes with respect to each other, such an attraction can act within a spacing of a few nanometers [37]. For closely packed tubes within a medium, the surface adsorption of a dispersant, or the wetting of the polymer/solvents, both require a temporary exfoliation state. Physical approaches such as shear mixing [38], mechanical stirring, sonication [39], ball milling [40] and micro-bead milling [41] processes have been employed for this purpose. Although these techniques may appear very different, they are all governed by the transfer of physical shear stress onto nanotubes which breaks down bundles.

In shear mixing, for example, the separation of individual CNTs from bundles is achieved in shear flow induced by the rotation of an extrusion in a polymer solution or melt. Usually, dispersion via shear mixing is only achievable for specific types of MWCNTs, with a high shear rate in a rather viscous medium. Terentjev *et al.* demonstrated that nanocomposite containing high loading concentrations of CNTs (up to 7wt%) could be dispersed via this technique [42]. However, the processing time significantly goes up as loading concentration rises. More importantly, shear mixing tends to section carbon nanotubes into shorter length scale, thereby reducing their conductivity significantly—an undesired attribute for nanocomposite intended for use as a sensor material.

The dispersion of carbon nanotubes could be assisted by the introduction of a common solvent—an organic solution which dissolves polymer resin easily and at the same time allows monodispersion of carbon nanotubes. In this case, two dispensed solutions sharing common solvent but containing carbon nanotubes and polymer resin respectively, undergoes mechanical stirring or the increasingly popular sonication process. Following that, two solutions are mixed together to further go through stirring or sonication. Finally with the complete evaporation of solvent, CNTs would leave dispersed in polymer. Here the choice of organic solvent is critical for determining the final dispersion quality and depends on the polymer matrix. For PDMS alone, various organic solvents have been reported to assist dispersion of CNTs, such as toluene [43], tetrahydrofuran (THF) [44], chloroform [45-46], dimethylformamide (DMF) [47], etc. While each report claims high dispersion quality of CNTs, there is lack of standard characterization protocol for dispersion of CNTs within polymers [36], leaving room for

subjective judgment. Comparative experimental tests are still needed to verify optimal solvent choice for the dispersion of carbon nanotubes.

It should be noted that even with optimal common solvent to help dispersion, the optimization of process conditions is still critical to ensure final dispersion quality. In the stage of solvent evaporation, for instance, as CNTs concentration continuously increases so does the re-aggregation effect of CNT bundles. Thus, this step needs to be best shortened to minimize the compromise of dispersion.

2.2 Micropatterning of PDMS-CNT nanocomposite

2.2.1 MEMS photolithography

Photolithography (or "optical lithography") is a process used in microfabrication to selectively remove parts of a thin film or the bulk of a substrate. It uses light to transfer a geometric pattern from a photo mask to a light-sensitive chemical "photoresist" on the substrate. A series of chemical treatments then either engraves the exposure pattern into, or enables deposition of a new material in the desired pattern upon, the material underneath the photoresist [48]. As one of the most commonly used techniques in IC and MEMS fields, the procedure of photolithography is well established.

Generally, the process starts with the design and fabrication of a photo mask. Then, substrate (mostly silicon wafer or glass) is cleaned and dried, following by the application of photoresist atop via spin coating. After pre-baking of photoresist to drive off excessive photoresist solvent, wafer is exposed to an intense light (usually ultraviolet light) which is filtered through the designed photo mask. Then, a post exposure bake is typically conducted, followed by the development of photoresist in a chemical bath. Next, in the

etching step the upmost layer of the substrate in areas that are not protected by photoresist is removed either physically or chemically. Finally, when the photoresist is no longer needed it could be removed from the substrate by a photoresist developer. Until now, a complete run of photolithography is finished.

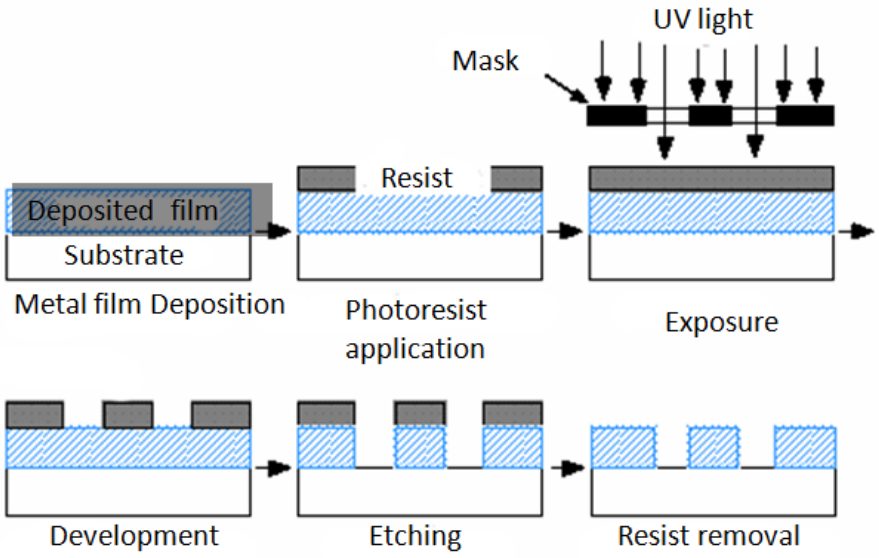

Figure 2.2 Schematic showing the general procedures of a MEMS photolithography process [48].

2.2.2 Nanocomposite patterning techniques

It has been noted that, unlike metal which can be readily etched by either physical ions or chemical developer, solidified polymer nanocomposite lacks chemical agent in which its exposed portion can be selectively dissolved. Therefore, metallic patterning through photolithography is not directly transferrable to polymer nanocomposite.

In the past few years, several approaches have been explored by researchers to pattern PDMS-CNTs nanocomposite into microstructures. In one protocol, standard photolithography and manual filling of nanocomposite were utilized to form micropatterns [3,7-8,10]. The first step was to define photoresist patterns using

photolithography described above and then to manually fill the pattern molds with conductive PDMS composite. Excessive amount of composite was removed from the photoresist mold by a razor blade. While feasibility was successfully demonstrated, this fabrication protocol required repetition of the complicated photolithography processes for each device. In addition, since photoresist was later developed in a chemical bath, any remaining amount of excessive nanocomposite could adhere to micropatterns and affect the functioning of whole device. In another protocol, photosensitive chemical agents were added into the PDMS-CNTs nanocomposite converting it into a photopatternable resist [11]. Standard photolithography was carried out to pattern it. As inspirational as this idea was, the addition of chemical agents and their development during photolithography could alter the properties of polymer nanocomposite. Also, nanocomposite being an optically non-transparent material, its photopatterning thickness could be limited as UV light could not penetrate through the whole depth of material. Finally likewise the above protocol, repetition of complicated photolithography processes was still necessary for each sensor sample.

To overcome these drawbacks, two alternative approaches, microcontact printing and laser ablation assisted screen printing, are introduced in this work to realize reliable micropatterning of conductive polymer nanocomposite.

2.2.3 Basics of microcontact printing

The original version of microcontact printing [49] was mainly used to stamp chemical or biological compounds onto a substrate area to modify surface chemistry [50-51]. Due to its simplicity and high efficiency, this surface patterning technique has evolved into different forms over the last decade broadening its range of application in MEMS [52–

55]. In this work, the application of microcontact printing is further expended to micropatterning of conductive nanocomposite.

This technique uses a pre-fabricated stamp with desired micropatterns to dip into an ink reservoir of polymer nanocomposite and directly transfers conductive patterns to an arbitrary substrate. Since the printing mold can be repeatedly used to generate a large number of new samples in a short time scale, the fabrication process is greatly simplified and reduced in time compared to the aforementioned approaches. Further, without the need for photolithographic facilities and other special work environment (e.g. clean room), this fabrication protocol potentially reduces turn-around time and lab operational cost.

2.2.4 Basics of laser ablation

Although microcontact printing techniques solves many issues in fabrication, a disadvantage it has is that it still requires the fabrication of a new printing stamp for each different design of micropatterns since the printing stamp is pre-manufactured (by micromachining or photolithography). This presents inconvenience for sensor prototyping, which typically mandates testing and optimizing of many different pattern designs. A second protocol—micropatterning via laser ablation assisted screen printing is designed to circumvent this particular issue.

Essentially, laser ablation is a process in which polymer molecules in the exposed area of a highly focused laser beam absorb optical energy and evaporates in gaseous form. Since molecules are stripped off the film layer-by-layer from top to bottom, the ablation depth is closely related to the optical energy received in the exposed spot [56–58]. Usually in the widely used excimer laser systems, optical energy is proportional to the

number of emitted laser pulses. During laser ablation, it is important to precisely control the pulse number so that the exposed polymer thin film would be just burnt through, as under-exposure does not lead to through holes on the film and over-exposure transfers energy and heat to surrounding environment causing undesired surface damage.

In this fabrication protocol, micropatterns are defined by laser ablation of a thin polymer film using a highly focused laser beam. Customizable in its size and intensity, the laser beam ablates through the thin film cleanly following a path that is programmed by software. Nanocomposite is then directly filled into the open grooves with excessive amount removed with the peeling-off of the film screen. In this way, it takes only a new CAD drawing to generate a new sensor pattern design, ideal for saving time and cost in sensor prototyping works.

2.3 Polymer nanocomposite-based sensors

2.3.1 Strain sensor

Strain is defined as a relative measure of mechanical deformation. Mathematically it can be expressed in equation:

$$\varepsilon = \frac{\Delta L}{L} \qquad (2.1)$$

where ε is strain, L is original length of object and ΔL is change in length of object. Strain is referred to as tensile when object is being prolonged ($\Delta L>0$) and compressive when object is being shortened ($\Delta L<0$). Strain sensor is a device used to measure strain.

Having wide commercial applications and low cost, metal and solid-state strain gauges are readily available. However, materialistic limitations such as rigidity and bio-

incompatibility have restricted conventional strain gauges in certain applications (e.g., sensing of implantable biomechanical strain in biomedicine). Polymer nanocomposite, on the other hand, offers an interesting alternative of strain sensors.

According to literature reports, various polymers, as shown in Table 2.1, have been incorporated with carbon nanotubes to construct strain sensors, which are capable of holding strain larger than that of conventional metallic and solid-state strain gauges.

Table 2.1 Examples of strain sensors made from different polymer matrices and their respective performances.

Author	**Year**	**Polymer matrix**	**Strain level**	**Resistance change**	**Reference**
Umbrecht *et al.*	2005	Poly(ethylene) (PE)	0.1%	Optical detection	[24]
Kang et al.	2006	poly(methyl methacrylate) (PMMA)	0.6%	2.7%	[21]
Zhang et al.	2006	Polycarbonate (PC)	1%	7%	[23]
Liu et al.	2007	poly(L-lactide) (PLLA)	0.5%	15%	[25]
Pham et al.	2008	poly(methyl methacrylate) (PMMA)	1%	6%	[22]

Compared with polymers shown above, elastomer poly(dimethylsiloxane) PDMS owns unparalleled mechanical elasticity, making it an better choice for large-range strain (>10%) sensing applications. Its flexibility allows it to be readily attached to curved surfaces, which is often necessary in biomedical sensors. Also, PDMS being a biocompatible material is widely used in biomedical areas [28]. Furthermore, the ability for PDMS-CNTs nanocomposite to be patterned into microstructures provides potential

feasibility for its practical usage as MEMS-based biomechanical strain sensor. Then this sensing format could potentially be implanted into human body as illustrated in Figure 2.3, and integrated with a wireless communication unit.

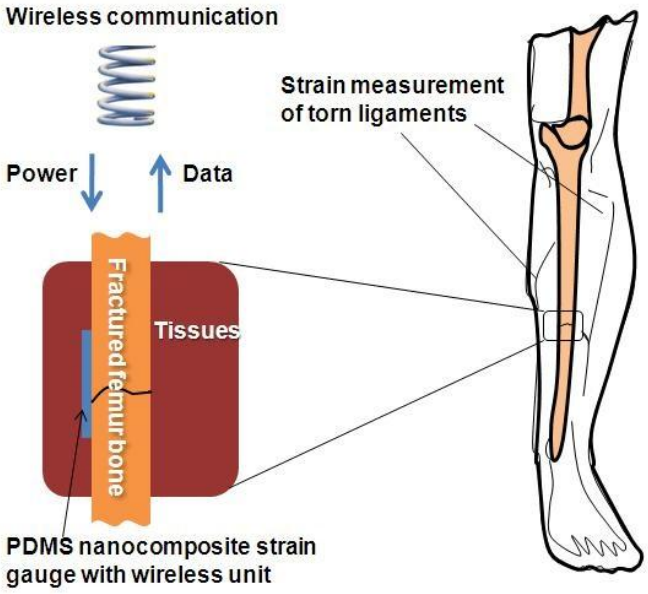

Figure 2.3 A long-term goal of the implantable strain sensor with wireless sensing capability [59].

The basic principle of strain sensing using PDMS-CNTs nanocomposite is quite straight forward. For a polymer to be electrically conductive, nano-scaled fillers must either physically touch to form electron conducting path, or be sufficiently close to each other to allow electron transfer via “tunneling effect” [60]. Therefore, the conductivity of the PDMS-CNTs nanocomposite system is dictated by the number of interconnection nodes and distances between neighboring carbon nanotubes. For tunneling of electrons between CNTs to occur, the distance between neighboring CNTs needs to be on the scale of nanometers (e.g., less than 3 nm). When a uniaxial tensile strain is applied to the

nanocomposite, as demonstrated in Figure 2.4, carbon nanotubes are separated apart, leading to loss of contact points and widening of inter-tubular distances. This impedes the electron transferring ability of the conductive network and causes overall resistance to rise. Similarly, when nanocomposite is relaxed electron conduction paths are restored, therefore resistance drops along with decreasing strain.

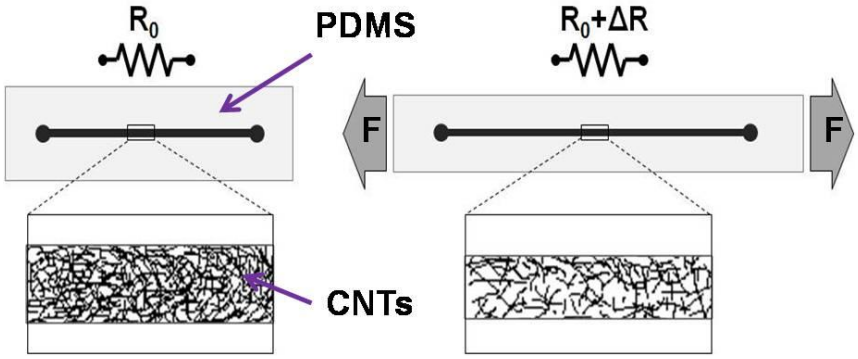

Figure 2.4 Schematic diagram showing the interconnection and spacing change of carbon nanotubes when PDMS-CNTs nanocomposite is exposed to tensile strain.

2.3.2 Pressure sensor

A pressure sensor measures pressure, typically of air/gas and liquid. Pressure is an expression of the force required to stop a fluid from expanding, and is usually stated in terms of force per unit area. A pressure sensor acts as a transducer; it generates an electrical signal as a function of the pressure imposed. A diaphragm based pressure sensor, in particular, is used to sensor the pressure difference between the two sides of a thin film in which the sensing element is included.

Like strain gauge, silicon-based pressure sensors are commercially available today [61-62]. However, due to the rigidity of silicon, it has been challenging to detect minute changes of pressure. Various polymer based sensors have also been explored [63–67].

While interesting feasibilities have been demonstrated, in terms of sensitivity there is still much room for improvement to detect extremely small changes of pressure (< 100 Pa).

Due to the superior flexibility of PDMS, once made into a thin film diaphragm, it could deflect much more significantly than other materials when under the same differential pressure. With PDMS-CNTs nanocomposite embedded in the thin film working as pressure sensing element, even the smallest changes of pressure could lead to significant resistive change, offering possibility of a differential pressure sensor with high sensitivity (100 Pa or less), which is significantly higher than other comparable reports.

2.3.3 Other applications for nanocomposite

Potential applications of polymer nanocomposite are, by all account, not limited to strain and pressure sensors. With similar fundamental principles, a variety of other sensors could be developed. Utilizing the patterning capability of nanocomposite and its sensitive response to normal stress, local differences of pressure could be detected which enables it to work as pressure mapping device—or tactile sensor. To new a few demonstrated examples, stress sensor was described by various groups [68–71], for instance, Kang *et al.* using a composite of SWCNTs and polyimide; epidermal electronics were demonstrated by Kim et al. which included various physical sensors [15], [72] ; flow sensors were illustrated by Hui *et al.* using a composite of MWCNTs and polymers [73–76]. Infrared (IR) light sensor was shown by Pradhan *et al.* [77], thanks to the unique absorption characteristics carbon nanotube have under IR irradiation.

In addition to sensors, other potential applications of polymer nanocomposites have also been demonstrated. Electrostatic discharge and electromagnetic shielding components have been made of polymer nanocomposite, for instance, using its electrical

conductivity [78]. Also, aerospace composites are actively being developed from polymer nanocomposite [79].

CHAPTER 3: PREPARATION OF POLYMER NANOCOMPOSITE

3.1 Introduction

As stated in Chapter 2, a uniform dispersion of carbon nanotubes inside polymer matrix is vital for ensuring the conductivity consistency of polymer nanocomposite. With microstructures, the requirement is even higher than bulk material, as micro-sized CNTs bundles could affect the current conducting path more significantly in microstructures.

The idea of introducing a common solvent to help disperse both CNTs and polymer has been widely used in the preparation of polymer nanocomposites. The choice of an optimal solvent depends on the type of polymer and CNTs, as it needs to dissolve both well to be effective. Also, it should be pointed out that even though a solvent may disperse CNTs alone extremely, the inclusion of polymer could adversely affect the dispersed state of CNTs. This phenomenon was in fact observed in our experiment, and will be discussed later in this chapter.

There are three popular dispersion approaches of dispersing CNTs inside polymer matrices, including shear mixing, mechanical stirring and sonication, each with its respective merits and disadvantages which will be discussed. In our dispersion experiment, we found that a combinatory approach involving several approaches could be used for optimized dispersion.

After obtaining initial dispersion of CNTs and polymer inside the common solvent, the next step—evaporation of the assisting solvent is also crucial for the final dispersion. As CNTs concentration rises during the course of solution drying, aggregation of CNTs

tend to occur which lead to deterioration of dispersion state. Therefore, conditions need to be optimized at this stage to minimize the re-aggregation of CNTs and ensure final dispersion quality of polymer nanocomposite. This chapter mainly addresses these issues.

3.2 Materials and reagents

Pristine multi-walled carbon nanotubes (MWCNTs) used in this work were purchased from Cheaptubes, Inc. (Brattleboro, VT) with a relative purity > 95wt%. The dimension of the MWCNTs was 20-30 nm in outer diameter, 5-10 nm in inner diameter and 10-30 μm in length, as shown in Figure 3.1 which is a tunneling electron microscopy (TEM) image of MWCNTs specified above. To comparatively study the effect of surface functionalization on its dispersion state, MWCNTs treated with carboxylic acid groups (MWCNTs-COOH) were also obtained from the same company (MWCNTs-COOH contains 1.23 w% -COOH groups. The other properties remained the same, with relative purity > 95wt%, 20-30 nm in outer diameter, 5-10 nm in inner diameter and 10-30 μm in length, to affirm the validity of the comparative study.

The polymer matrix used in this work—poly(dimethylsiloxane) (PDMS)—is a silicone elastomer. Specifically, Sylgard 184 silicone elastomer kit was purchased from Dow Corning Inc. (Midland, MI), which had two parts: polymer base resin and curing agent. The two parts are recommended to be mixed at the ratio of 10:1 and exposed to thermal curing in order realize solidified PDMS. In fact, the mixing ratio could be varied in order to tune mechanical properties of PDMS (Young's modulus), making it a versatile material to utilize.

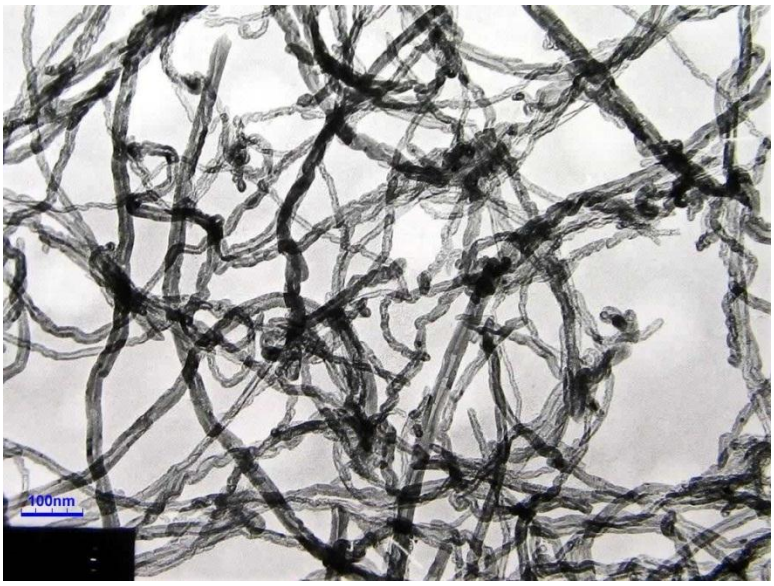

Figure 3.1 TEM image of MWCNTs with purity > 95wt% and outer diameter 20-30 nm from Cheaptubes, Inc. [80].

3.3 Selection of optimal solvent for dispersing CNTs within PDMS

The dispersion assisting solvent depends on the type of polymer and CNTs, as it needs to dissolve both well to be effective. Also, even when a solvent disperses both polymer and filler well separately, the combination of the two could have an adverse effect on the dispersion state. Therefore, the conclusion of an optimal common solvent could only be drawn after careful comparative experimental studies.

3.3.1 CNTs dispersion in different organic solvents

As noted in Chapter 2, a variety of organic solvents have been used to assist dispersion of CNTs in polymers. Solvents including toluene [43], tetrahydrofuran (THF) [44], chloroform [45-46], dimethylformamide (DMF) [47], etc., in particular, have been reported to reach great dispersion. Nevertheless, due to the lack of sufficient dispersion characterization data from these reports, experimental studies are still required to

compare their actual performances and verify optimal choice for the dispersion of carbon nanotubes. An advantage of comparative study is that only relative dispersion quality is required to be evaluated, based on which a best solvent could be chosen from the solutions tested.

To compare the dispersion of MWCNTs in different solvents, four organic solutions including toluene, chloroform, DMF, and THF, as shown in Table 3.1, were used for experimental test in the following manner.

Table 3.1 Important properties of experimentally tested organic solvents.

Organic solvent	**Chemical formula**	**Density (g/ml @ 20^{o}C)**	**Boling point (^{o}C)**	**Vapor pressure (kPa @ 20^{o}C)**
Toluene	$C_6H_5CH_3$	0.86	110.6	2.93
Chloroform	$CHCl_3$	1.48	61.2	21.1
Tetrahydrofuran	C_4H_8O	0.89	66	19.3
Dimethylformamide	C_3H_7NO	0.94	153	0.3
PDMS base resin	**(C_2H_6OSi)**	**1.11**	**N/A**	**N/A**

First, quantities of pristine MWCNTs weighing about 3 mg were added into four vials containing 10 ml of respective solutions, yielding a concentration of 0.3 mg/ml, as shown in Figure 3.2 (chloroform).

Here, a low concentration was desired to offer partial optical transparency in dispersed solutions. Through trial and error, it was found that solution with concentrations higher than about 1 mg/ml, after dispersion, would become completely non-transparent, which was not desirable for direct visual observation. On the other hand,

it was found in experiments that a concentration of 0.3 mg/ml or lower was possible for direct visual observation of dispersion qualities. Although the 0.3 mg/ml threshold was somewhat empirical, MWCNTs dispersed around this concentration were able to be observed clearly and consistently. With this small amount of MWCNTs the inaccuracy of the weight equipment was relatively significant (±1 mg) which might cause variations in the concentration of MWCNTs in different solvents. However, later optical observation would prove, though, this variation was not significant in affecting the dispersion quality of solutions.

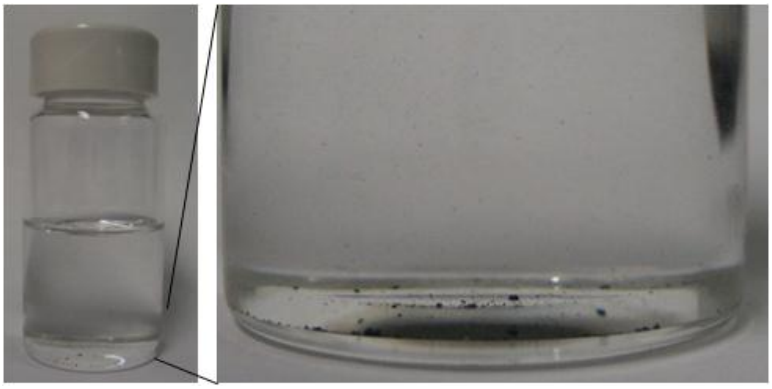

Figure 3.2 Images showing 3 mg of MWCNTs being added into 10 ml of chloroform. In the magnified view black bundles settled on vial bottom were from as-is MWCNTs.

After introducing MWCNTs into four solutions, each mixture was then sonicated using a mild sonication bath (FS20D Fisher Scientific, frequency 42 kHz, output power 70 W) for 30 minutes at nominal power. This process yielded semi-transparent dispersed MWCNT suspensions, as shown in Figure 3.3(a), composed of individual nanotubes and micro-sized bundles which were invisible to the bare eye.

The stability of CNT dispersion state is a valuable indication of its dispersion quality, as CNTs tend to reaggregate into bundles with time in an unstable environment. The

longer dispersion lasts and the fewer/smaller CNT bundles occur, the higher its dispersion quality. Here a simple approach of optical observation of CNT bundles was applied to evaluate dispersion quality. Although this approach could not determine the absolute quality of dispersion, it was well suited for comparative studies, where only relative information was extracted and compared from samples tested under identical conditions.

All 4 vials were held still after their sonication. 70 hours afterwards unstable dispersions showed signs of reaggregation to different extents, as indicated in Figure 3.3(b). Visible MWCNT bundles were observed to settle at the bottom of vials, as shown in Figure 3.3(c) (chloroform) as an example. In the worst case of toluene, suspension showed apparent phase separation, with MWCNTs almost completely settled at the bottom and upper solution void of dispersed MWCNTs. Based on visual observation of the amount of reaggregated MWCNTs in various comparative experiment settings, it was likely that the reaggregation effect had an order of: toluene > chloroform > THF > DMF.

One week after sonication, as shown in Figure 3.3(d), solutions largely remained their dispersion state, other than the now transparent toluene solution. Figure 3.3(e) shows that, even after an extended holding period of 8 months, MWCNTs dispersion in the other 3 solutions maintained its stability, regardless of the fact that part of solutions evaporated causing CNT concentration to rise. In the case of chloroform, especially, the amount of its CNT bundles, as shown in Figure 3.3(f), did not increase notably from the 70 hour mark, which proved it to be also a stable dispersion. Overall, despite minor variations in dispersibility of MWCNTs, all 3 solvents including chloroform, THF and DMF could be considered candidates to help the dispersion of CNTs inside polymer nanocomposite.

3.3.2 Solubility of PDMS base polymer in different organic solvents

As a common solvent to assist dispersion of polymer nanocomposite, another important requirement is its ability to dissolve the polymer matrix. Therefore, the choice of solvent varies significantly depending on the type of polymer matrix. For PDMS specifically, the four organic solvents (toluene, chloroform, DMF, THF) which have been used in previous reports were used here for testing.

It should be noted that since PDMS is a two-part thermal curable polymer, only one part should be used in the dispersion process of CNTs. As dispersion usually takes more than a few hours, the presence of two parts mixed together could render PDMS partially polymerized, which then would not be usable anymore for microfabrication. With a manufacturer-recommended mixing ratio of 10:1, PDMS base polymer resin occupies more than 90% weight of the polymer matrix, thus the base polymer is generally the part used for dispersion with CNTs. Curing agent, on the other hand, would be added after the evaporation of the common solvent, which will be discussed later in this chapter.

Out of the 4 organic solutions tested, toluene was found to have great solubility for PDMS base polymer. However, it was not an ideal candidate as common solvent due to its relatively poor dispersion of MWCNTs. DMF, although had the best dispersibility for MWCNTs, was found to react with PDMS base resin. Upon mixing of the two solutions, a while colored gel-like substance was formed due to chemical reaction. Thus, while it maybe useful to be used for dispersion of other polymer matrices, in the case of PDMS, it would not be useful for the fabrication of nanocomposite due to chemical incompatibility.

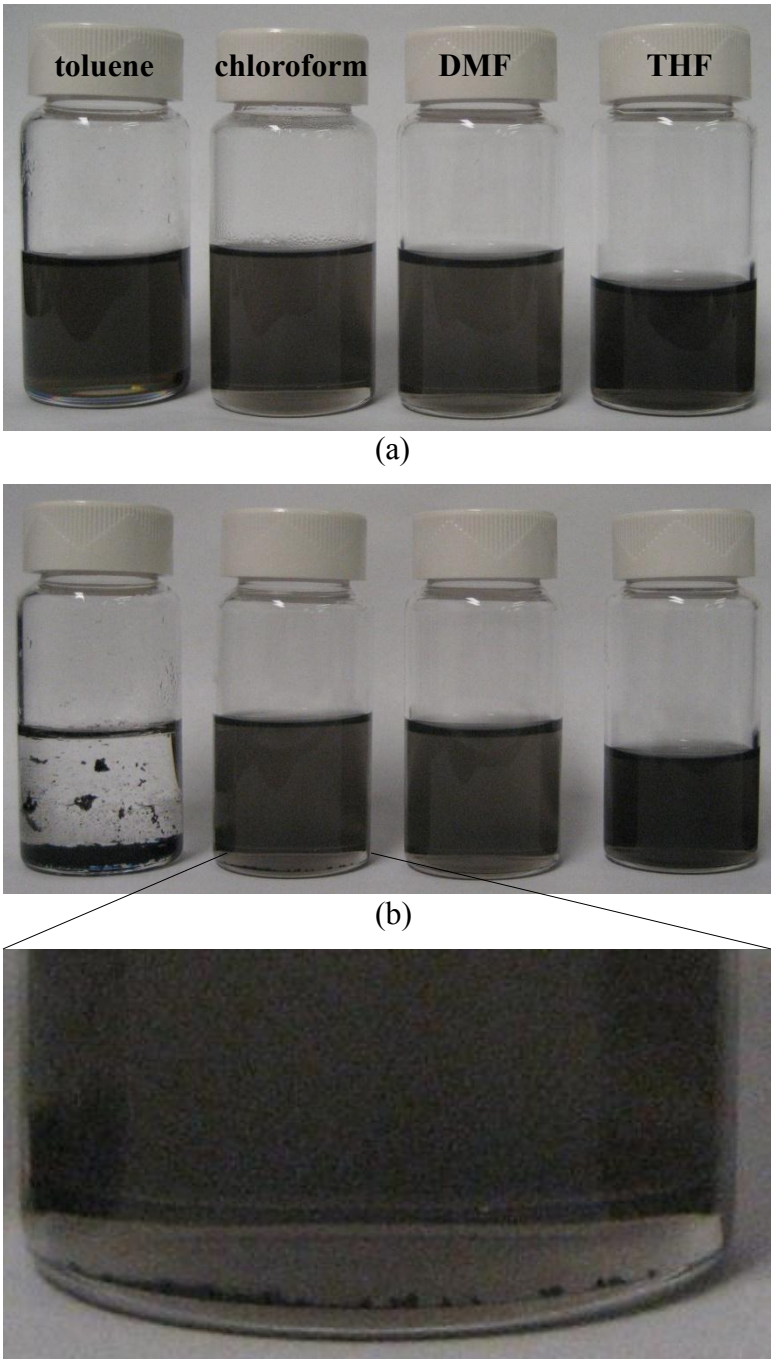

(a)

(b)

(c)

Figure 3.3 MWCNTs dispersed in different organic solvents via 30 minutes of sonication. Solutions from left to right: toluene (0.3 mg/ml MWCNTs), chloroform (0.3 mg/ml), Dimethylformamide (DMF) (0.3 mg/ml), tetrahydrofuran (THF) (0.4 mg/ml). (a) Dispersion state right after sonication, showing no visible MWCNT bundles; (b) Solutions at 70 hours after sonication showing reaggregation effect of MWCNTs in order of toluene >> chloroform > THF > DMF; (c) Magnified view of visible MWCNTs

(Figure 3.3 continued) bundles in chloroform solution; (d) 1 week after sonication. Volume of THF solution was slightly adjusted to match the others after 4 days with no further sonication; (e) 8 months after sonication. Solutions have evaporated to different extents but 3 out of 4 dispersions remained stable; (f) Magnified view of visible MWCNTs bundles in chloroform dispersion, indicating that amount of bundles remained about the same with (c).

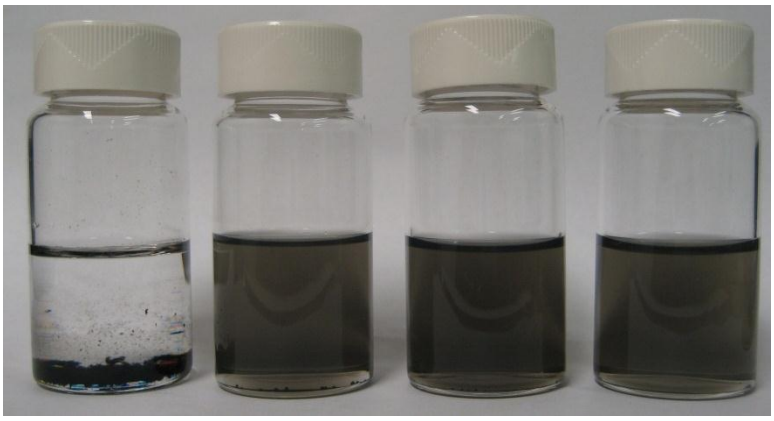

(d)

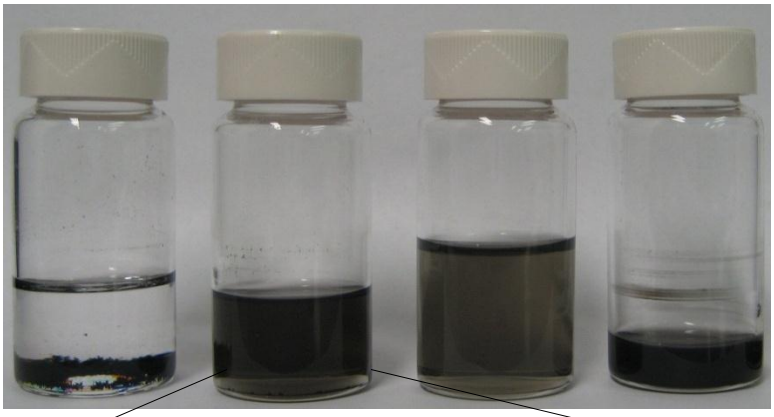

(e)

(f)

Interestingly, chloroform and THF were both found to own high solubility of PDMS base resin, able to dissolve PDMS at concentration higher than 0.3 g/ml. Because of their relatively high dispersion of MWCNTs, both of these could potentially work as common solvents for the preparation of polymer nanocomposite. Further tested were conducted (as follows) as visual observation alone may not be sufficient to distinguish which of the two solutions would work better for PDMS.

3.3.3 The effect of PDMS on dispersed carbon nanotubes in different organic solvents

Supposedly, as long as the common solvent can dissolve MWCNTs and PDMS well separately, it should work for the combination of the two. The two suspended solutions could simply be poured together to go through further sonication in order to achieve high quality dispersion. Surprisingly, that was found to be not the case with certain organic solvents.

From the above section, both THF and chloroform were promising candidates to work as common solvent due to their exceptional ability to disperse MWCNTs and PDMS separately. However, when MWCNTs and PDMS were both present in the solvent, THF and chloroform had dramatically different performances.

In the case of THF, firstly MWCNTs were dispersed at 0.4 mg/ml (±0.2 mg/ml) via sonication for 10 minutes. Then, PDMS base resin at 0.15 g/ml concentration was added into the already-dispersed CNTs, as shown in Figure 3.4(a). From Table 3.1, as the density of PDMS base resin (1.1 g/ml) was higher than THF (0.89 g/ml), PDMS settled at the vial bottom and could be clearly told from the dispersed CNTs. Afterwards, the mixture was sonicated for an additional 30 minutes, resulting in a fully dispensed solution,

as in Figure 3.4(b). However, this dispersion state was not stable with time. MWCNTs almost started reaggregating immediately, forming visible bundles just 30 minutes after sonication was finished, as seen in Figure 3.4(c). Moreover, after a period of 21 hours, originally dispersed MWCNTs had now completely settled at the vial bottom, as shown in Figure 3.4(d), leaving the upper portion of solution fully transparent.

In fabrication of polymer nanocomposite, PDMS base was normally first dissolved in an organic solvent before being added into a CNT dispersion solution, instead of directly being added like in the above process. With the pre-dissolution of PDMS, similar effects also occurred when MWCNT dispersion significantly deteriorated after the introduction of PDMS content. The reason for the adverse effect of PDMS on THF-CNT dispersion has yet to be understood, however, although THF did not alter properties of PDMS base resin when mixed with it, some functional groups on PDMS base molecules could have affected the affinity between THF and MWCNTs.

In the case of chloroform, similar experimental procedures were carried out to test the effect of PDMS on the dispersion state of MWCNTs. Briefly, MWCNTs were first dispersed at 0.4 mg/ml (±0.2 mg/ml) via sonication for 10 minutes. Then, PDMS base at around 0.12 g/ml concentration was added into solution, as shown in Figure 3.5(a). Since the density of PDMS base (1.1 g/ml) was lower than chloroform (1.48 g/ml), PDMS stayed at the solution top separated from CNT. Then, solution was mechanically stirred for 14 minutes (to help expedite dissolution of PDMS) and consequently sonicated for 1 minute, leading to a fully dispensed solution. Unlike THF-CNT dispersion, the chloroform suspension remained much more stable, as shown in Figure 3.5(b), showing no visible deterioration of dispersion state even at 42 hours after sonication.

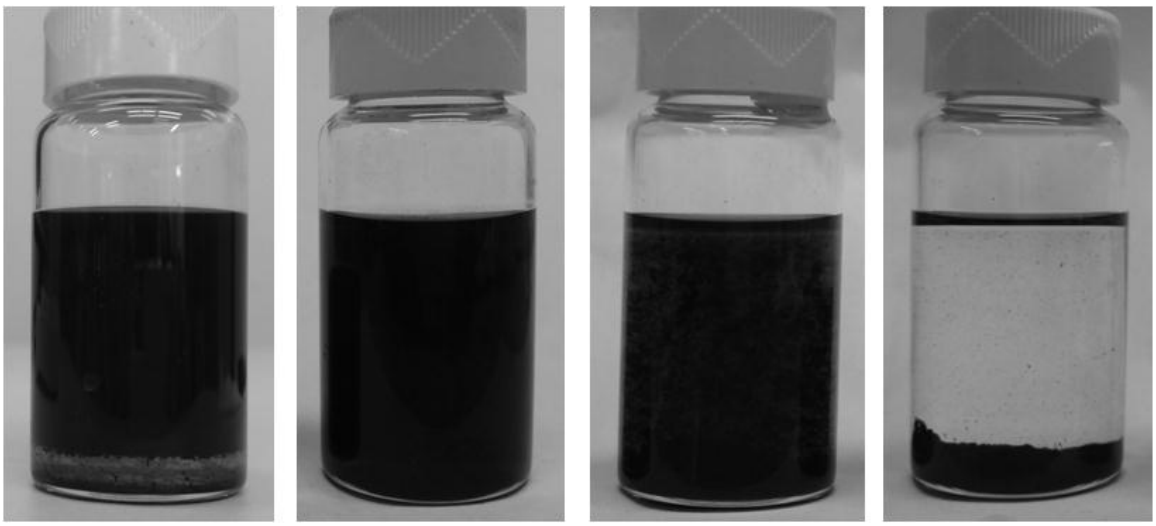

(a) (b) (c) (d)

Figure 3.4 Vial images showing effect of PDMS on dispersion state of MWCNTs in THF solution: (a) PDMS added into dispersed MWCNTs-THF solution; (b) THF solution containing PDMS and MWCNTs right after 30 minutes of sonication; (c) solution at 30 minutes after completion of sonication, showing visible CNTs bundles, and (d) solution at 21 hours after sonication, showing complete phase separation which indicated the instability of dispersion.

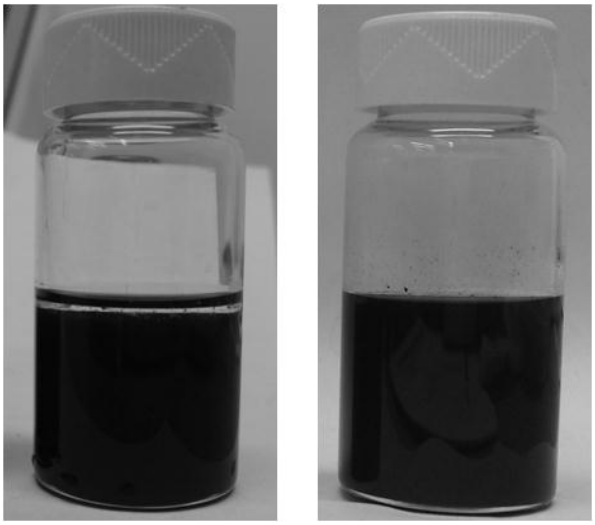

(a) (b)

Figure 3.5 Vial images showing effect of PDMS on dispersion state of MWCNTs in chloroform solution. (a) PDMS added into dispersed MWCNTs-chloroform solution, staying on top portion and (b) Chloroform solution containing PDMS and MWCNTs 42 hours after sonication.

Based on the above visual comparison in Figure 3.5 of THF and chloroform in which PDMS and MWCNTs were dispersed, it can be concluded that, with similar circumstances, chloroform yielded a much more stable—thus higher quality dispersion of PDMS base and MWCNTs. Therefore, the best choice of common solvent among tested solutions should be chloroform.

3.4 Effect of CNT functionalization on dispersion

It has been reported that carbon nanotubes with functionalized surfaces by carboxyl (-COOH) groups, compared to their pristine counterpart, could have better dispersion in polymer matrices [43], [81]. To verify the effect of surface functionalization, comparative experiment was carried out, in which pristine and –COOH carbon nanotubes were dispersed with PDMS base in chloroform solutions in a parallel fashion under similar conditions. Briefly, both pristine MWCNTs (0.14 mg/ml) and COOH-MWCNTs (0.16 mg/ml) were first sonicated inside two vials for 5 minutes. Then, PDMS base at around 0.13 g/ml concentration was added into both solutions, which went through additional sonication for 1 hour and mechanical stirring (magnetic stirrer at 1150 rpm) for 10 minutes. This process resulted in well dispersed solutions, as indicated in Figure 3.6(a). However, due to the adverse effect of mechanical stirring on an established dispersion state which will be discussed in next section, dispersed solutions became unstable 4 hours after stirring, as revealed in Figure 3.6(b), leadings to visible phase separation in the pristine MWCNTs solutions. Relatively speaking, it was clear that the COOH-MWCNT dispersion, after going through the same processing steps, was much more stable than the

pristine MWCNT dispersion. Therefore, it could be verified that carboxyl functionalized carbon nanotubes had better dispersion in polymers than pristine carbon nanotubes.

A potential reason for that was the covenant bond, such as CH-π hydrogen bond [82], formed between CNTs and the polymer matrix due to surface functionalization could help prevent nanotubes from agglomerating and forming bundles. Moreover, it was thought that, the production of robust nanocomposite materials may prefer a strong interface made of covalent chemical bonding between the nanofillers (i.e., carbon nanotubes) and the polymer matrix rather than the much weaker van der Waals physical bonds which occur if the fillers were not functionalized [81]. In addition, there may be static electric attraction between the -COOH groups on the nanotube surface and -CH3 groups on the PDMS (molecular formula: (C2H6OSi)n) backbone structure made of Si-O, since -COOH is an electron withdrawing group exhibiting partial negative charge, while CH3 is an electron donating group exhibiting partial positive charge. Further, extra space occupied by the -COOH groups on the nanotube wall could create a steric effect, which could prevent movement of the nanotubes within the matrix to a certain extent.

3.5 Comparison of dispersion approaches

As aforementioned in Chapter 2, amongst the main forms of physical dispersion methods three are particularly interesting: shear mixing, mechanical stirring, and sonication. In effort to optimize the dispersion process in the preparation of polymer nanocomposite, in this work these 3 approaches were experimentally tested and compared in terms of their performance, and a combinatory approach was proposed for the fabrication process.

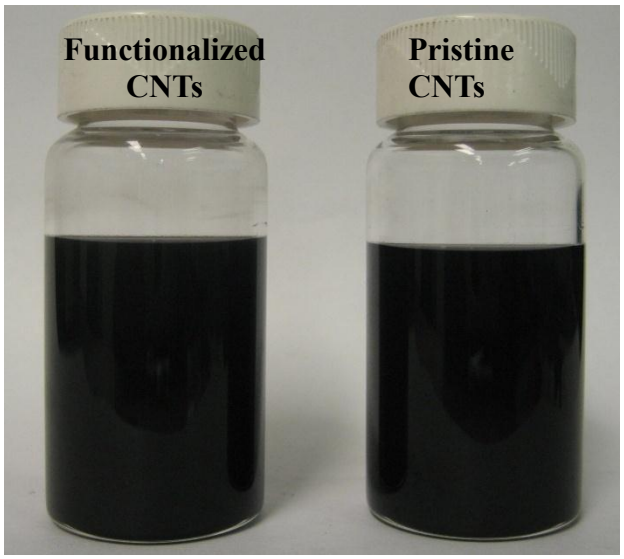

(a)

(b)

Figure 3.6 Comparative studies of functionalized and pristine MWCNTs in their dispersion with polymer matrix in common solvent: (a) initial dispersion of MWCNTs right after sonication and stirring showing non-transparent solutions and (b) dispersion at 4 hours after the stoppage of stirring, with pristine MWCNT case showing clear phase separation.

3.5.1 Shear mixing

Shear mixing separates individual CNTs from bundles via the shear flow induced by the rotation of an extrusion in a polymer solution or melt. Usually, dispersion via shear mixing is only achievable for specific types of MWCNTs, with high shear rate in a rather viscous medium. Therefore, it does not necessarily require any common solvent to assist dispersion, which simplifies the process. Nanocomposite containing high loadings of CNTs (up to 7wt%) have been realized via this technique [42]. However, a major downside is that the processing time significantly goes up as loading concentration rises. More importantly, shear mixing tends to section carbon nanotubes into shorter length scale, thereby reducing their conductivity significantly—an undesired attribute for nanocomposite intended for use as a sensor material.

In our experiments, various loading percentages of MWCNTs (~ 2-8 wt%) were shear mixed with PDMS base polymer using a drilling machine (GMC 10’’drill press stage, rpm 1000-1500 rpm). It was found that, although CNTs could be well dispersed within PDMS directly, the conductivity of the final nanocomposite was simply compromised too much for it to work effectively as a sensing material. The shortening of nanotubes due to shearing caused conductivity to decrease by more than 10 times compared to other approaches, which was undesirable for conductive nanocomposite. Therefore, this method was eventually not incorporated into the process of nanocomposite fabrication.

3.5.2 Sonication

Being the most popular dispersion technique today, ultrasonic agitation exposes CNTs to ultrasonic waves and transfers shear forces to individual nanotubes which break them from agglomerates. There are two frequencies of ultrasonic waves that are used: 1)

low frequency (~20-24 kHz); and 2) high frequency (~42-50 kHz). The sonication bath used in this work has high frequency but relatively low power (FS20D Fisher Scientific, frequency 42 kHz, output power 70 W). Although higher power of the sonication bath (>500 W) is desired as it provides higher shearing force to break down CNT bundles, nevertheless, prolonged exposure could also cause damaging of CNTs (especially shortening) which could significantly decrease the conductivity of CNTs [83]. Considering all factors, a mild sonication bath would be an ideal option as it allowed high quality of dispersion yet avoided severe damaging of CNTs during sonication.

Sonication was an essential process to control because it covered most of the nanocomposite preparation steps. Temperature was an important factor to control and normally needed to be low in the initial dispersion stage. Due to lack of cooling sinks on sonication bath, temperature was maintained relatively constant by changing bath water about every 30 minutes.

3.5.3 Mechanical stirring

Mechanical stirring facilitates dispersion as it creates shearing force through the high speed rotary motion of the stirrer. In this work, a magnetic stirrer was used which could rotate at maximal of 1150 rpm. Experiments found that, for the dissolution of PDMS in organic solvents, magnetic stirring worked more efficiently time wise than sonication. To dissolve 2 g of PDMS base in 15 ml of chloroform, for example, magnetic stirring (1150 rpm) could shorten dissolution time (could be estimated by disappearance of phase separation) from 1 hour (sonication time) to around 8 minutes which was a significant improvement.

In our experiments, however, mechanical stirring was found to be not beneficial for the improvement of CNT dispersion quality. As a matter of fact, it was shown to have an adverse effect on the dispersion state of PDMS-MWCNTs in common solvents. For the pristine MWCNT solution shown in Figure 3.5, the PDMS-MWCNTs dispersion in chloroform was, with 1 hour of sonication, stable when observed 3 days afterwards. But when solution went through 10 additional minutes of mechanical stirring (1150 rpm), the dispersion almost immediately became less stable, showing visible CNT agglomerates in the vial.

After comparing the 3 common dispersion approaches, it seemed that a combinatory approach would provide the optimal process. Mechanical stirring could be used for the initial dissolution of PDMS base in common solvent, as it was more time efficient. Sonication, on the other hand, could be used in the other aspects/steps of material preparation.

3.6 Experimental procedure for preparing polymer nanocomposite

After numerous experimental trials and improvements, the so-far optimized procedure to obtain homogenous polymer nanocomposite is as follows.

In the stage of initial dispersion, first COOH-MWCNTs (e.g., 0.2 g) are added into a solution of chloroform (e.g., 50 ml) inside a metric cylinder (e.g., 100 ml). Note that the CNT concentration here (4 mg/ml) is much higher than that used in the testing section, perhaps even higher than the solubility of CNTs in chloroform, but it was necessary to have a relatively high concentration because the weight of final nanocomposite needs to be at least a few grams to be useable. Plus, the small diameter of cylinder is usually preferred over a wide mouse beaker, because as little as the final polymer nanocomposite

is (e.g. for 5 wt% PDMS-CNTs, 0.2 g MWCNTs could produce only 4 g final nanocomposite), a wide beaker would cause majority of nanocomposite to stick onto the wall and bottom areas, leaving little for later usage.

After initial mixing of COOH-MWCNTs and chloroform, the mixture is sonicated for around 1 hour. Meanwhile, PDMS base resin (e.g. 3.5 g) is added into a separate solution of chloroform (e.g. 10 ml), and stirred with a magnetic stirrer (1150 rpm) for 15 minutes. Then, the two solutions are mixed together to go through 1-2 hours of additional sonication to ensure sufficiently uniform dispersion of MWCNTs and PDMS. Experiments suggest that, on top of this time, further extended time of sonication does not significantly improve dispersion quality anymore.

Next in the state of solvent evaporation, it is highly desirable to minimize the required time to fully dry up the organic solution. As the concentration of CNTs continuously rise (for more than 2 orders) during the solvent drying process, some reaggregation of nanotubes is bound to happen. To minimize the size and amount of CNT agglomerates, solution should be dried as soon as possible. In this work, two techniques have been introduced to help expedite the solution evaporation process.

Firstly, the temperature of the nanocomposite-containing chloroform solution could be raised close to its boiling point (61.2^{o}C). At this temperature, the properties of the nanocomposite stay virtually intact while the drying process dramatically speeds up. Simply, the fastest way to elevate solution temperature is to pour in pre-boiled water into the sonication bath, and carefully mix it to adjust the temperature to be at or slightly over the boiling point.

Secondly, the introduction of a vacuum pump into the cylinder could speed up the evaporation process as well. One problem with the narrow-mouthed cylinder is that it usually takes days for solution (e.g. 50 ml) to fully evaporate even at elevated temperature, since vapor molecules get saturated inside cylinder and could not quickly escape. A Teflon tube connected to a vacuum pump could quickly remove the chloroform vapors from the upper portion of the cylinder, thus reducing evaporation time significantly from several days to a couple of hours (actual time depends on solution volume, CNTs percentage, temperature and vacuum level).

Complete evaporation of the common solvent was important, since any present solvent could alter the mechanical/electrical properties of the nanocomposite. Thus, the dispersion assembly was usually placed inside a vacuum oven for an extra period of time (usually several hours) to ensure complete evaporation of the chemical solvent. Finally, after the complete evaporation of the common solvent and before the microfabrication of polymer nanocomposite, curing agent—another part of PDMS polymer should be introduced into the mixture. Since the mixing of curing agent and base polymer would cause PDMS to gradually solidify, usually in 24 hours at room temperature, it is desired to minimize the mixing time for curing agent. Simple manual mixing for 10-20 minutes is normally carried at here. At the mixing ratio of 10:1 (base to curing agent ratio), experiments suggest that the relatively short manual mixing time does not alter the dispersion quality obviously.

3.7 Dispersion characterization of final nanocomposite

As pointed out in Chapter 2, while the dispersion and clustering of spherical particles has been studied well, for both spherical and highly asymmetrical (platelets, rods and fibers) [84–87], it has remained a technical challenge to directly and reliably observe carbon nanotubes in the bulk of a nanocomposite suspension. All optical methods (e.g. optical microscopy) cut off below a length scale of 0.2-0.5 μm; all electron microscopy methods, though prominent in observations of individual nanotubes, could only provide information about the sample surface, i.e. only representative for the selected fields of view. This leaves reciprocal space techniques and, more importantly, global indirect techniques of characterizing the dispersed nanocomposites; each of these techniques suffers from the unavoidable difficulty in interpretation of results.

Although attempts have been made to quantitatively assess the dispersion characteristics of CNTs inside polymer matrices (e.g. using Minkowski connectivity, radial power spectral density) [88], most reports still have to rely on optical and electron micrographs, despite their shortcomings, to evaluate relative quality of CNT dispersion [43, 45-46, 89].

In an effort to compare relative quality of various CNT dispersions within polymer matrices, this work has also adopted optical microscopy and electron microscopy for observation of CNT dispersion within polymer matrix. For instance, during the dispersion process, a drop of chloroform solution containing dispersed functionalized CNTs and PDMS base (CNT ~ 4 mg/ml) was observed under a stereomicroscope. The optical micrographs shown in Figure 3.7 suggest that CNT cluster sizes generally did not exceed

10 μm. Compared to cluster sizes reported in existing literatures [43, 89], this was indicative of relatively high dispersion quality.

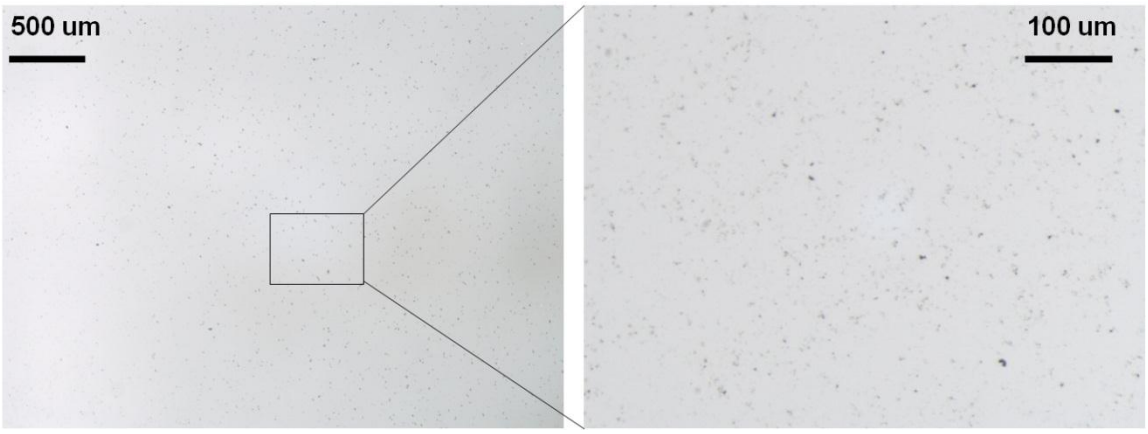

Figure 3.7 Optical micrographs of CNT dispersion inside a solution which contains chloroform, PDMS and functionalized MWCNTs.

In the final polymer nanocomposite, it is difficult to use optical microscopy to directly observe the bulk dispersion of CNTs within polymer matrix, especially for nanocomposites with a high loading percentage (>1%) of CNTs, since the samples normally become optically non-transparent. Scanning electron microscopy (SEM), on the other hand, provides a tool for observing the inside of a bulk sample. For example, a PDMS-MWCNTs composite sample containing functionalized MWCNTs was fractured in liquid nitrogen to obtain a cross section and viewed under SEM, as in Figure 3.8.

After optimization of our dispersion procedure, SEM images demonstrated relatively uniform distribution of nanotubes throughout the fractured surface. Cluster size throughout the nanocomposite remained consistently under about 3 μm. Compared with

previously reported SEM images, this indicates an excellent dispersion quality, especially for nanocomposite containing high percentage of carbon nanotubes (>5 wt%).

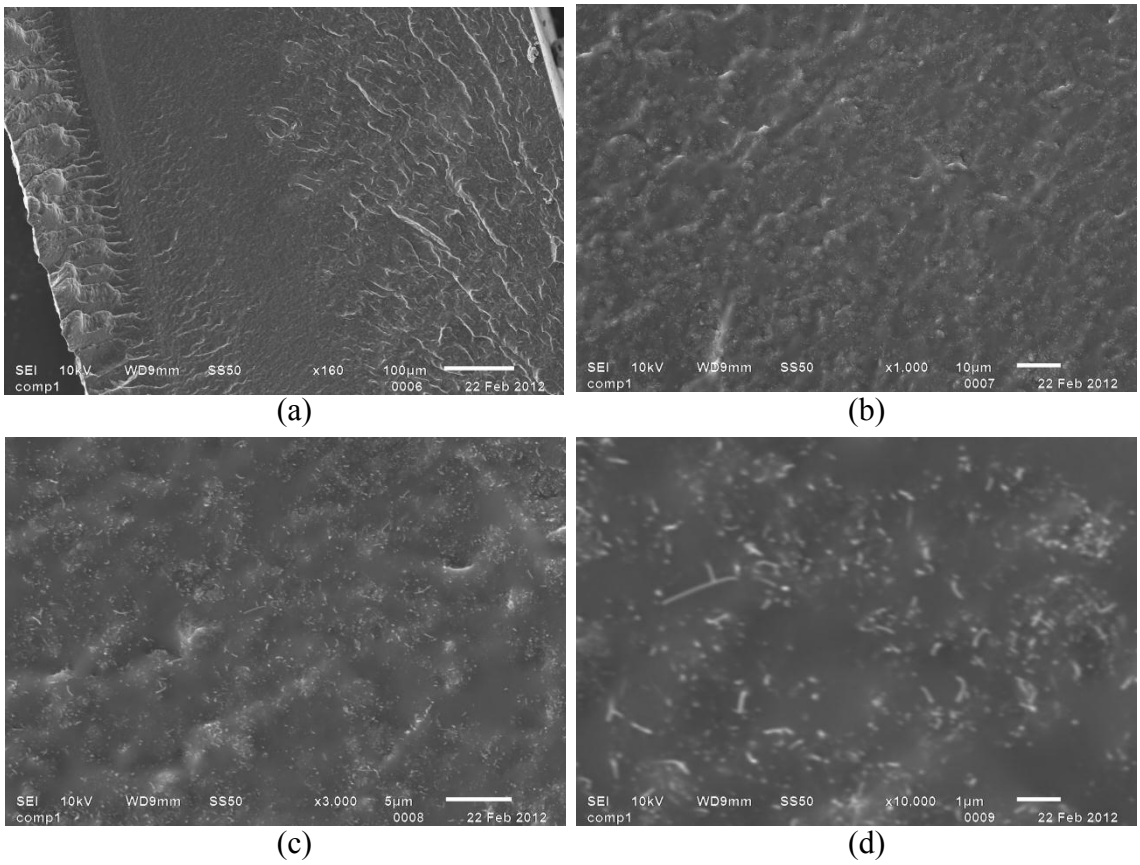

Figure 3.8 SEM images showing dispersed MWCNTs on a cross section of polymer nanocomposite that was fractured in liquid nitrogen. Nanocomposite contains around 7wt% of functionalized carbon nanotubes throughout its matrix. Observation was made on same area of surface with following increasing magnification: (a) 160X; (b) 1,000X; (c) 3,000X, and (d) 10,000X.

Overall, the preparation of polymer nanocomposite with homogeneous distribution of carbon nanotubes throughout the polymer matrix is critical to later steps of realizing sensor devices, as it determines the conductivity consistency of microstructures. It would be shown in later chapters that the dispersion quality achieved with the protocol describe

here, although not perfect on the molecular level, could achieve consistent conductivity in the micropatterned structures.

3.8 Electrical properties of polymer nanocomposite

For nanocomposite to effectively work as electrodes or sensing elements in polymer-based systems, good electrical conductivity is usually desired. Here the conductivity of bulk PDMS composites was characterized with different loading percentages of MWCNTs. To carry out conductivity measurement, a changing direct current (DC) voltage was applied across each conductive PDMS composite pattern. For each DC voltage level, a corresponding DC current was measured. The voltage-current relationship was used to calculate a resistance, which was then converted to a conductivity. Figure 3.9 shows the measurement results of conductive composite patterns with different carbon nanotube loading levels. Various sizes of composite samples were tested during experiments, yielding consistent conductivity data.

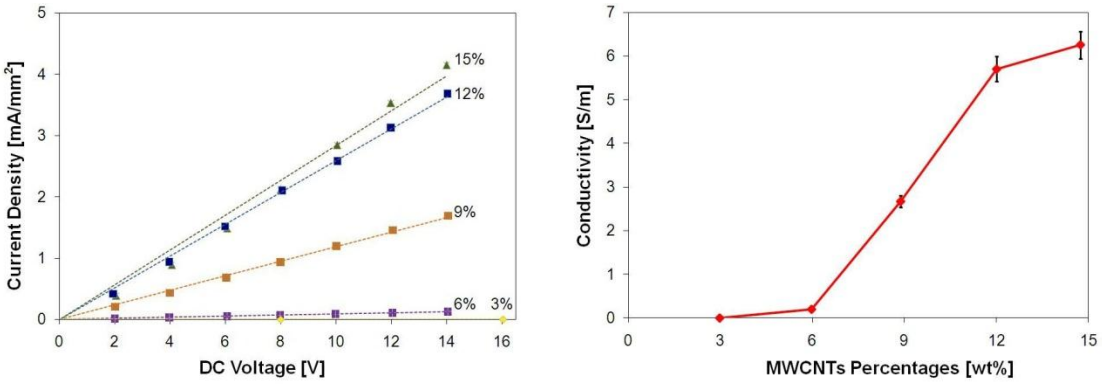

(a) (b)

Figure 3.9 Conductivity measurement results: (a) current density of PDMS composite patterns under increasing DC voltages and (b) conductivity of PDMS composite patterns with different loading levels of MWCNTs [90]. Tested bulk samples were around 22.1 mm long, 25.4 mm wide, between 0.3-0.78 mm thick. Samples were prepared using

sequential sonication and evaporation of a PDMS-MWCNTs mixture in a common solution-toluene.

It was observed that the conductivity of measured samples showed a slight trend of nonlinearity under an electric field. Current density of measured samples rose with an increasing DC voltage in a near parabolic fashion rather than a perfectly linear one although this nonlinearity was negligible under low voltages. Interestingly, since higher voltages could produce more Joule heating and cause sample temperature to rise, conductivity should typically decrease [91-92]. However, the observed increase in conductivity, in spite of the potential thermal effect, could be explained that the applied electric field somehow align the carbon nanotubes inside PDMS in the direction parallel to the electric field resulting in better connections of nanotube networks and higher conductivity. For applications that require a relatively high electrical field across the conductive composites, this nonlinearity effect should be taken into account. After a linear approximation of the V-I curve, the conductivity of the PDMS composites was measured to increase significantly from as low as 0.003 S/m with a loading percentage of 3 wt% to 6.3 S/m with a loading percentage of 15 wt%. For loading percentages higher than 15 wt%, better conductivity could be achieved but PDMS composites then became too viscous to be spin-coated and printed. In practice, carbon nanotube loading of about 6~9 wt% would be preferred because it yields effective manipulation and sufficient conductivity for short range electrodes or sensing elements in MEMS systems. In ideal cases, as the percentage of carbon nanotubes increases, conductivity could continuously arise until reaching an upper boundary. The upper boundary of the conductivity, however,

is potentially limited by tunneling of electrons between carbon nanotubes, which creates an inter-nanotube junction resistance [93].

In I-V tests, when the polarity of DC voltage is reversed, the I-V curve may not be fully reversible (i.e., current levels may vary to a small extent). However, based on literature reports on various CNT-based composites, the I-V curves mostly remain consistent in both positive and negative voltage directions [94-95]. The consistency may especially apply when the DC voltage is small (e.g., less than 2 volts) [94]. When large voltages are applied, current variations may become more significant.

For temperature effect on resistance, the resistances of PDMS-MWCNTs composites were measured at varying temperature, and relative resistance changes were calculated. As shown in Figure 3.10, the relative resistance of a representative sample increased by less than 6% when environmental temperature rose from room temperature 23^{o}C to as high as 80^{o}C. For sensing applications under 50^{o}C, its resistive impact could be regarded as minimal. Further, for applications that need to eliminate the impact of environmental conditions such as temperature and moisture, a differential circuitry configuration could be applied to offset the influence.

For conductive nanocomposite patterns to work as electrodes or sensors, it is also important to establish reliable electrical contacts between the composite patterns and off-chip electronic circuits or instruments. Although metal wires or probes can be directly inserted into the conductive composite after curing or solidifying for electrical contact, it was observed that optimal electrical contacts were obtained when metal surfaces were made to contact the conductive composite before complete curing. While further study is required to fully understand the mechanics of contact resistance, it seems that metal

surfaces and carbon nanotubes in PDMS under curing process reach maximum interface area leading to minimized contact resistance between metal and carbon nanotubes.

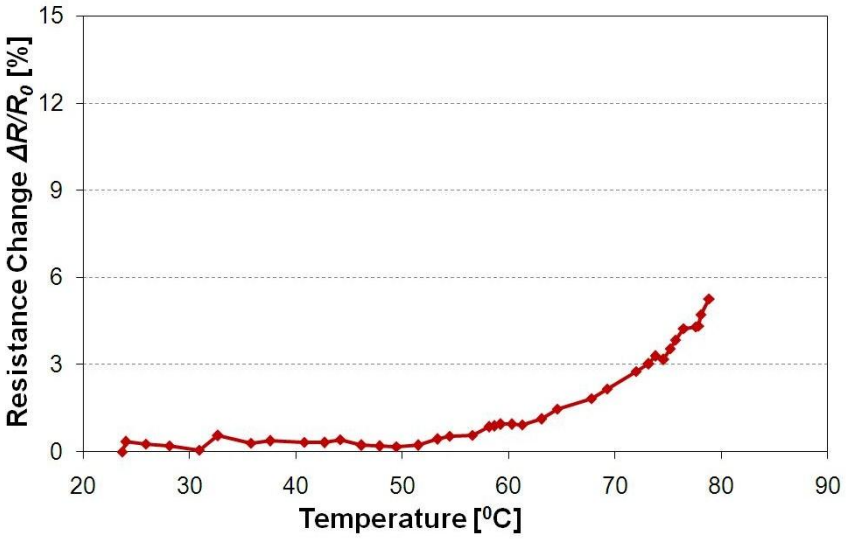

Figure 3.10 Environmental temperature effect on the electrical resistance of a PDMS-MWCNTs composite pattern with around 9 wt% MWCNTs. Tested sample was a composite line (around 44 mm long, 0.9 mm wide, and 50 μm thick) embedded in a bulk PDMS device. Composite was prepared using same method described above in Figure 3.9.

3.9 Summary

In this chapter, to assist the dispersion of MWCNTs inside PDMS matrix and realize a uniform distribution, a common solvent was selected amongst various tested organic solutions. Based on its high solubility for PDMS and MWCNTs respectively, and its ability to retain dispersed state of MWCNTs in presence of PDMS, chloroform was found to be an optimal choice as a common solvent. Also, the surface functionalization of CNTs by carboxyl groups was found to be beneficial for further improvement of dispersion quality.

Through extensive testing of a variety of widely used physical dispersion techniques such as shear mixing, mechanical stirring and sonication, a combinatory approach was developed in which mechanical stirring was used to facilitate the initial dissolution of PDMS inside common solvent, and mild sonication used to as a main tool to disperse MWCNTs within PDMS. Following the dispersion stage of MWCNTs and PDMS within the common solvent, the evaporation process was facilitated and expedited by use of vacuum pump and accurate control of elevated temperatures. Solution drying time was significantly shortened, and thereby initial dispersion quality was largely retained throughout solvent evaporation.

Even at high loading concentrations of CNTs within polymer, high quality dispersion of nanocomposite was achieved, which showed significant improvement over prior approaches. Dispersion quality was studied using various characterization tools such as optical microscopy and electron microscopy. Furthermore, important electrical properties were characterized in detail. Electrical conductivity of nanocomposite was found to be suitable for use as short-range electrodes or more importantly as piezoresistive sensing elements. In addition, temperature dependence of electrical properties was measured to be minimal, which was also a desirable attribute for sensor applications.

CHAPTER 4: MICROPATTERNING CONDUCTIVE POLYMER NANOCOMPOSITE

4.1 Introduction

For conductive microstructures in polymer-based MEMS systems, conductive polymer nanocomposite may carry certain advantages over metallic materials because of their inherent compatibility with polymer materials (e.g., homogenous interface, ability to withstand large strain, etc.). Several approaches have been explored by researcher over the past few years for the patterning of conductive polymers, as discussed in Chapter 2. Although these methods demonstrated interesting feasibilities, there were issues that needed improvement. For example, photolithography-based mold patterning required repetition of the relatively complex photolithography processes for each device. Also, any remaining amount of excessive nanocomposite could adhere to micropatterns and affect the functioning of whole device. For another example, using the addition of photo-sensitive agent could also be limited as UV light could not penetrate through the whole depth of material.

To overcome drawbacks in existing fabrication techniques, two alternative fabrication protocols, microcontact printing and laser ablation assisted screen printing techniques, are introduced in this work to realize reliable micropatterning of conductive polymer nanocomposite. This chapter focuses on detailed discussion of multiple aspects of these two protocols, including their approach, fabrication process, micropatterning characterization, advantages over current techniques and potential limitations.

4.2 Patterning via microcontact printing

4.2.1 Approach

The first approach we take advantage to pattern conductive polymer nanocomposite is microcontact printing technique. As introduced in Chapter 2, the original version of microcontact printing was mainly used to stamp chemical or biological compounds onto a substrate area to modify surface chemistry [50-51]. Due to its simplicity and high efficiency, this surface patterning technique has evolved into different forms broadening its range of application in MEMS [52–55]. In this study, a microfabricated printing mold is employed to define conductive nanocomposite patterns. Various structures have been successfully embedded into unmodified PDMS to form conformal and robust all-elastomer devices, along with characterization of printing uniformity and electrical conductivities. Since the printing mold can be repeatedly used to generate a large number of new samples in a short time scale, the fabrication process is greatly simplified and reduced in time compared to reported approaches. Further, without the need for lithographic facilities and other special work environment, this technology demonstrates great feasibility to pattern conductive electrodes or sensing probes in MEMS systems at low cost.

In order to realize functional regions of conducting PDMS together with structural regions of insulating PDMS, a fabrication process is developed, as shown in Figure 4.1, based on microcontact printing and cast molding techniques. This process has been published, along with characterization and application findings [97].

The overall fabrication process is rather simple. Firstly a printing mold is made through micromachining or photolithography. Next, it is inked into a spin-coated thin

layer of conductive PDMS composites. Then, it is lifted from the ink and stamped onto another substrate, transferring all conductive patterns. Partial curing is conducted to solidify the imprinted patterns, after which additional bulk PDMS is cast atop and fully cured. Finally, whole PDMS block is debonded from the substrate, forming a conformal all-elastomer device. As illustrated in Figure 4.1, the ability to repeatedly use the printing mold significantly simplifies the fabrication process and improves the efficiency of forming conductive PDMS patterns.

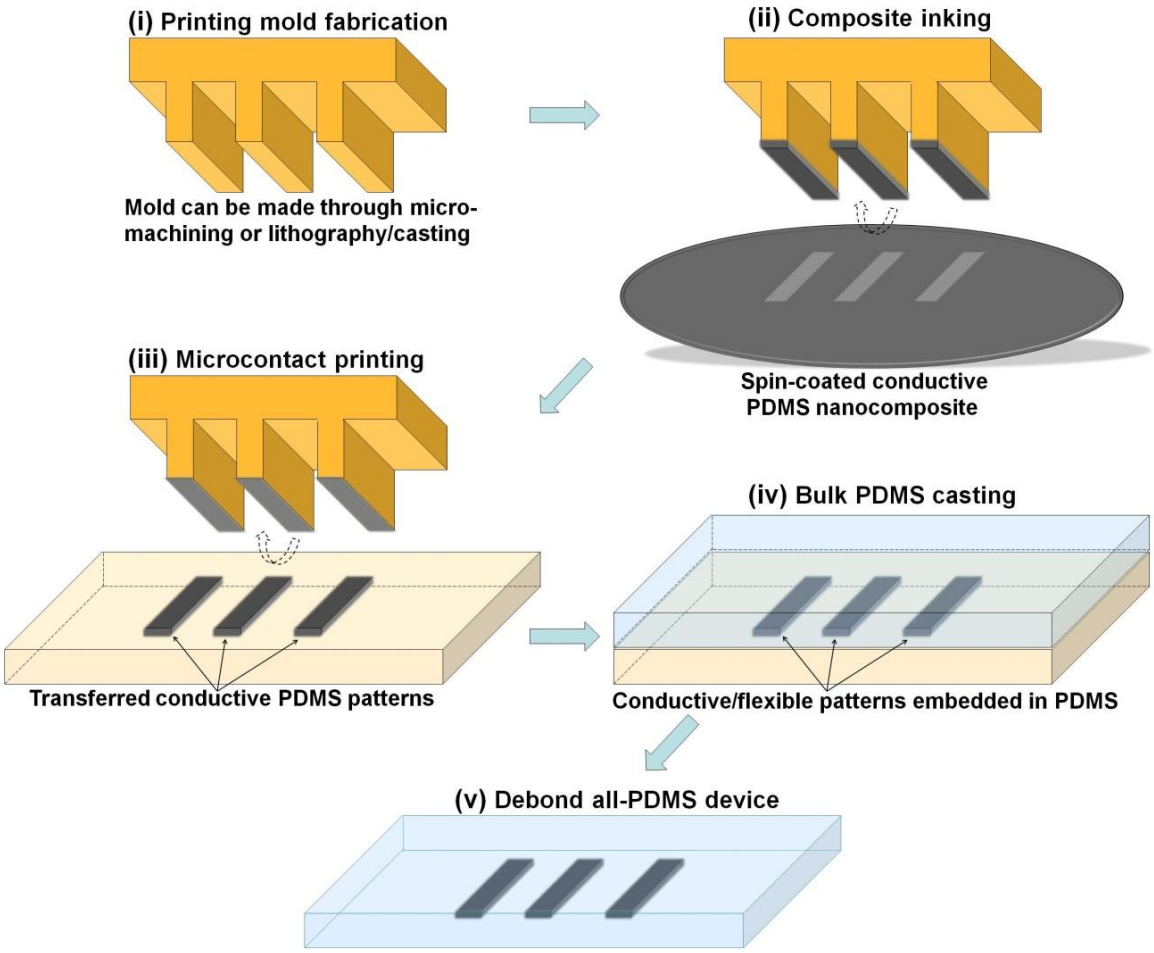

Figure 4.1 Schematic diagram showing the process flow of embedding conductive nanocomposite patterns in PDMS by combining microcontact printing and cast molding techniques.

4.2.2 Preparation of printing mold

The process of embedding conductive patterns started with the fabrication of printing mold. Soft polymers are often preferred as they allow conformal contact between the stamp and the surface to be imprinted. Here, poly(methyl methacrylate) (PMMA) was selected as the mold material for feasibility tests. AutoCAD design of printing mold was processed in a micromachining system (Kern MMP micromilling and drilling machine) down to a resolution of a few hundred micrometers. Although the resolution of patterning obtained in feasibility tests was not particularly high for a MEMS patterning technique, in applications where higher resolution is desired, photolithography and mold casting can be employed to make printing molds. Once fabricated, the mold can be used for multiple times in subsequent steps.

4.2.3 Fabrication process

After the fabrication of printing mold with designed patterns, it was held onto the vertical beam of a wafer prober (Ultrasonic Inc., Model 660) where 3-D position control was available. Meanwhile, conductive polymer nanocomposite was prepared via sonication and mechanical stirring (using a common solution of toluene, MWCNTs between 3-9 wt%, PDMS base to curing agent ratio of 10:1). After preparation, the polymer nanocomposite was spin-coated (spin coater model: WS-650SZ-6NPP/LITE, Laurell Technologies Corp., North Wales, PA) into a thin layer (~ 50 μm) on a silicon wafer which was then placed underneath the printing mold. Next, the mold was carefully dipped into the ink solution and lifted up shortly in a few seconds, leaving a thinner layer of residual ink on the silicon wafer. As the extruding surfaces of the printing mold were covered with conductive ink (i.e., polymer nanocomposite), patterns were transferred by

stamping onto a slide glass substrate which had been previously treated with chlorotrimethylsilane (from Alfa Aesar)—a chemical release agent to help debonding of PDMS from glass. In a subsequent step, the imprinted conductive composites were cured in a hot oven at 60^{o}C for 30 minutes to solidify patterns and avoid any diffusion into bulk PDMS later. After that, additional bulk PDMS mixed with base polymer and curing agent was then poured atop to submerge all imprinted patterns. In the final step, the whole PDMS block was degassed and fully cured at 60^{o}C for 4 hours before debonding from the substrate. Eventually, all-elastomer devices were realized with embedded compatible patterns as shown in Figure 4.2.

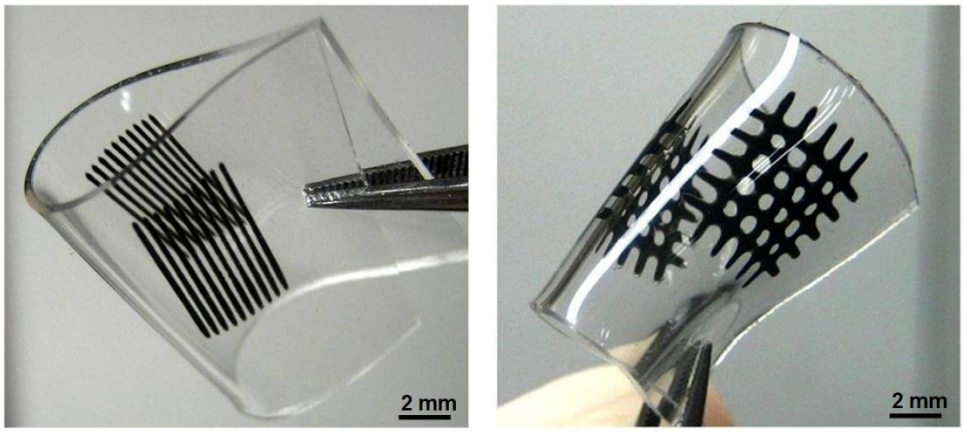

(a) (b)

Figure 4.2 PDMS samples with embedded conductive and flexible patterns fabricated through microcontact printing and cast molding.

In my experiments, the fabricated PDMS samples displayed superior mechanical flexibility upon repeated bending or stretching, which was an attractive attribute for flexible electronic modules and sensors. Actual time needed for pattern transfer was less than 1 minute, and as a result, large numbers of devices were attainable in a short time frame.

4.2.4 Patterning characterization

In order to evaluate the patterning quality of this fast method, a simple pattern was selected to characterize its uniformity. As shown in Figure 4.3, the micromachined PMMA printing mold had a pattern consisting of ten lines of 10 mm-long, 200 μm-wide (± 4 μm, 2% tolerance), and equally spaced by 400 μm gaps.

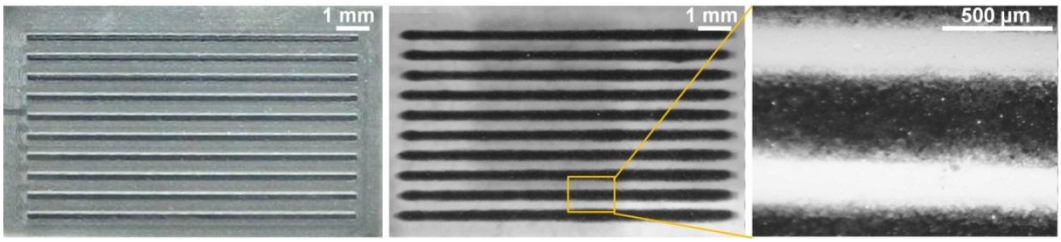

Figure 4.3 Photographs of the sample mold and the embedded patterns: (a) a picture of the PMMA printing mold made through micromachining; (b) a microphotograph of the PDMS sample with 10 embedded line patterns transferred from the PMMA mold, and (c) a magnified section of the embedded pattern.

After microcontact printing, the final average width of the embedded lines was measured to be about 314 μm with an average spacing of 286 μm. The increased pattern size could be resulted from several combinatory factors. For instance, small amount of conductive composites during “inking” could adhere to the bottom edge of side walls of the patterns on the printing mold and these unwanted composites could be transferred to the imprinted substrate. Besides, excessive force exerted between the stamp and substrate during printing could also cause the imprinted patterns to spread to the sides. Another possible factor could be the diffusion of imprinted composites on the substrate before complete solidifying. While the spreading effect could potentially limit the resolution of

microcontact printing, improvements on processing steps would substantially downsize the minimum printing scale.

The illustrated line patterns above were reasonably uniform in their width according to measurement results indicated in Figure 4.4. For each single line, the maximum width variation across the length was found to be less than ±12% of its average width. Taking into account that the printing mold made from micromilling had a variation of ±2% in its width, the tolerance of the imprinted patterns could be as low as ±10%. Moreover, the average width among the ten lines was ranged between 310 and 320 μm, which showed a variation of merely ±2% of its average width. Overall, the measured data indicated reasonable patterning uniformity through microcontact printing.

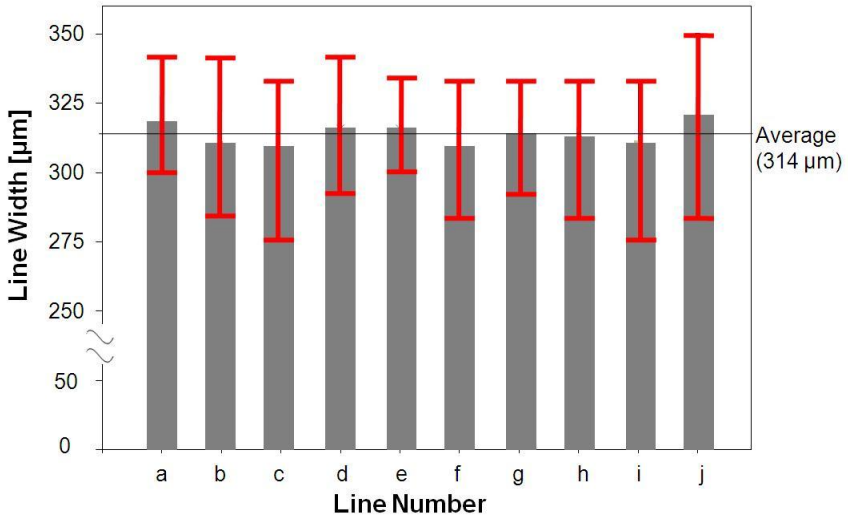

Figure 4.4 Width characterization data of embedded line patterns. To obtain approximate width information across the length of the ten 10 mm-long lines, measurement was conducted at 9 equally spaced points on each line (1 mm between every two points). Top points of each bar represent average width of individual lines, which gave an average line width of 314 μm.

On the other hand, the cross section of embedded nanocomposite patterns was observed under an optical microscope, as demonstrated in Figure 4.5. The manually cut

nanocomposite lines revealed a semi-oval shaped cross section, and their thickness was measured to be 38 μm with a variation of ±10%. Factors contributing to the final thickness included the amount of composite solution being transferred from ink film to the printing surface, which was affected by the thickness of the ink film and surface affinities of the ink substrate, the printing mold and the printing substrate to the composite ink. Further, after printing the flowing of fluidic composites from pattern center to the sides before its solidification also caused a change in the final pattern thickness. While the pattern thickness were not necessarily similar to that of the ink film with the current setup, an improved printing system and optimized processing steps would certainly serve to help stabilize the thickness of embedded patterns.

Figure 4.5 Micrograph showing the cross section of three parallel nanocomposite lines embedded in unmodified PDMS. The bulk PDMS film was about 330 μm thick, and nanocomposite lines around 38 μm thick.

4.2.5 Discussion

There are several important aspects of microcontact printing which directly contribute to the patterning quality. First, a defect-free printing mold is obviously a prerequisite for any ideal pattern generation, as any drawback on the mold would be automatically transferred onto the imprinted substrate. Secondly, an evenly spin-coated thin layer of

conductive composites is crucial as well because any inhomogeneity in the thin layer could translate to uneven attachment of ink on the stamp and poor pattern transfer thereafter. Finally, the surfaces of the printing mold and ink layer need to be properly aligned for them to be parallel with each other in order to ensure good printing reliability. While reasonably uniform and repeatable patterns are attainable with the current setup, in the long run processing parameters can be further optimized to improve printing performance.

One of the common issues with pattern transfer by microcontact printing is the enlargement of imprinted patterns [52], which imposes a potential limitation on the minimal printing size. If patterns are too closely spaced, the gaps between each pattern could be over-flown by uncured composites. Proper measures could to be taken to address this issue and improve the printing resolution. An advanced printing system with accurate control of the space and force exerted between the stamp and substrate, for example, would better control the amount of ink to be transferred, and prevent "ink" solution from spreading to the sides. Another issue is the surface property of printing mold or "stamp." The surface chemistry of printing mold could be selectively modified to avoid undesired attachment of PDMS composites on the side walls. Furthermore, since PDMS composites have different affinities to inking substrates, stamps, and printing substrates, refined selections of materials for those components could allow composite ink to be fully transferred from one surface to another, enhancing the "inking" and "stamping" process substantially. Finally, since the curing conditions of the imprinted patterns, such as curing temperature, time and geometry (e.g. imprinted pattern facing upwards or downwards or with a certain degree) also affect how much the conductive ink

solution flows to the pattern sides, further optimization of these parameters would serve to minimize the tolerance of conductive patterns. Overall, should the discussed measures be adequately taken, the resolution and reliability of microcontact printing would be greatly improved.

4.3 Patterning via laser assisted screen printing

4.3.1 Approach

Although patterning through microcontact printing technique solves many issues in the microfabrication of nanocomposite, one of its disadvantages lies in the fact that since the printing stamp is pre-manufactured (by micromachining or photolithography), it still requires the fabrication of a new printing stamp for each different design of micropatterns. This presents inconvenience for sensor prototyping, which typically mandates testing and optimizing of many different pattern designs. Another protocol—micropatterning via laser ablation-assisted screen printing circumvented this issue and significantly improved other aspects of microfabrication.

Essentially, laser ablation is a process in which a small volume of polymer molecules in the exposed area of a focused laser beam absorb high optical energy, break up their molecular bonds and evaporate in gaseous form [56, 98-99]. In our system, polyethylene terephthalate (PET) was found to be an optimal choice of polymer for the 248 nm KrF excimer nanosecond laser (GSI Lumonics PM-848 UV Pulse Master from LightMachinery Inc., Ottawa, Ontario, Canada). After receiving a homogenous laser beam, the ablation system (RapidX 1000 Series from Resonetics Inc., Nashua, New Hampshire, USA) then uses a beam delivery technique referred to as direct write

machining (DWM) to create patterns on the PET surface. Figure 4.6 illustrates the working principle of this system. Briefly, the square laser beam first goes through a series of directional change by turning mirrors. Then its size and shape are regulated by through holes in an imaging mask. Its dimension is demagnified by optical lenses, after which it radiates onto a polymer film for ablation. The film sits on an X-Y moving stage which is programmed by a computer aided design (CAD). In this setup, micropattern geometries are simply controlled by software. It saves fabrication time and cost by eliminating hardware such as a lithography mask or a printing stamp.

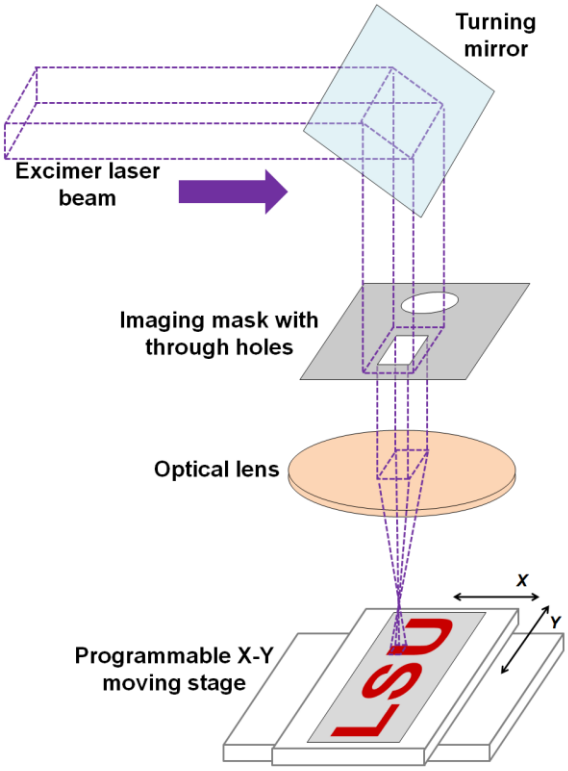

Figure 4.6 Schematic diagram of laser ablation system which uses a beam delivery technique of direct write machining. An arbitrary pattern “LSU” is programmed via CAD software.

4.3.2 Laser ablation conditions

Important parameters of the nanocomposite micropatterns, such as spatial resolution and size uniformity, are largely determined by the laser ablation process. Therefore, the optimization process conditions (film material, laser energy, focus, stage moving speed, etc.) are critical to the realization of high quality microstructures. As discussed in Chapter 2, laser ablation is a process in which polymer molecules in the exposed area of a highly focused laser beam absorb optical energy and evaporates in gaseous form. Since molecules are stripped off the film layer-by-layer from top to bottom, the ablation depth is closely related to the optical energy received in the exposed spot. In our ablation system (Resonetics RapidX 1000 Series with excimer laser Lumonics PM-848 UV, KrF 248 nm), the optical energy is proportional to the number of emitted laser pulses. As demonstrated in Figure 4.6 the scanning data obtained from an optical profiler (CHR 150 from STIL, France) with a 59 μm-thick polyethylene terephthalate (PET) film different number of laser pulses resulted in different ablation depth. It was important to precisely control the pulse number so that film would be just burnt through, as under-exposure would not lead to through holes on the film and over-exposure would transfer energy and heat to surrounding environment and cause undesired surface damage.

4.3.3 Selection of screen material

In order to obtain successful micropatterning of nanocomposite via laser ablation assisted screen printing process, the selection of appropriate film material was a first and foremost critical factor. There are three important criteria concerning film material: 1) it should be able to ablated by laser beam cleanly through without any significant damage to surrounding areas; 2) it can adhere tightly to the substrate but later can be lifted off

easily after the filling of nanocomposite without any damage to the film or substrate; 3) it can be readily available and made into different micron range thicknesses for controllability of nanocomposite pattern thickness.

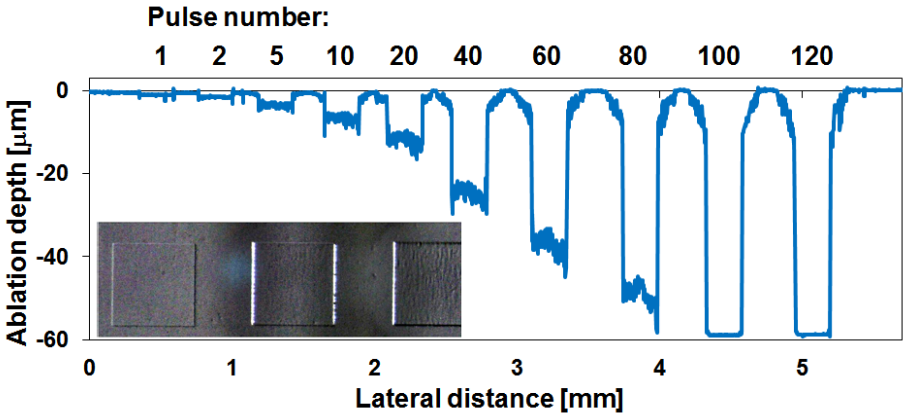

(a)

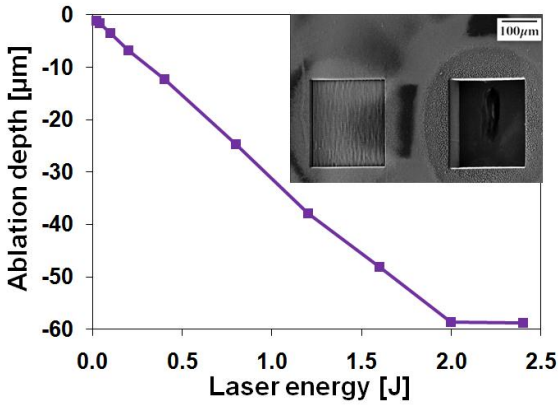

(b)

Figure 4.7 Translational scanning data of an optical profiler reveals different ablation depth of a 59 μm-thick PET film as a result of increasing laser energy/pulse numbers (laser energy per pulse = 20 mJ): (a) When the number of pulses reached 100, PET film was ablated through to the glass substrate and depth remained the same. Inset shows three ablated square patterns (250 x 250 μm^2) with increasing depth from left to right; (b) Ablation depth under different dosage of laser energy. Inset shows two square patterns with left one ablated incompletely and the right one ablated through. Some excimer laser parameters: energy per pulse = 20 mJ; pulse duration = 12~20 ns; repetition rate = 100 Hz; average power = 2 W.

Although the laser system (248 nm KrF) used in this study could ablate through various polymer materials, including PDMS, PC, PET, PMMA and so forth, it sometimes causes topographical damage to areas adjacent to the exposed spot of laser beam (e.g. PDMS). This effect severely affects the patterning resolution of laser ablation, therefore those polymers are not ideal choices. My experiments revealed that polymer PET could be ablated by laser cleanly without topographical damage to the surrounding areas, therefore tested three types of PET-based tapes/films which could potentially be used as the screen material, as shown in Figure 4.8.

The three PET-based materials shown were magic tape (from 3M), removable tape (from 3M) and PET film (common screen protector). These materials satisfied at least two criteria of an appropriate screen printing film, as they could all be ablated cleanly by laser beam (Figure 4.8) and were all widely available commercial products. Compared with magic tape, the removable tape had more durable film layer, but relatively less adhesion with a surface. The magic tape was quite soft, therefore during the screen peeling-off step it would often be torn apart if the micropatterns were complex. As for the removable tape, it was more durable than magic tape, but the loose glue layer at the bottom of the tape prevented tight sealing between the tape and substrate. During the nanocomposite filling stage, the nanocomposite tended to penetrate underneath the film which was undesired. On the other hand, the tested PET film worked outstandingly well, as it offered tight sealing between the film and glass substrate, yet would not be broken during the peeling-off step because of its mechanical strength. Even more, it provided the smoothest surface which was beneficial for removal of excessive nanocomposite with a razor blade.

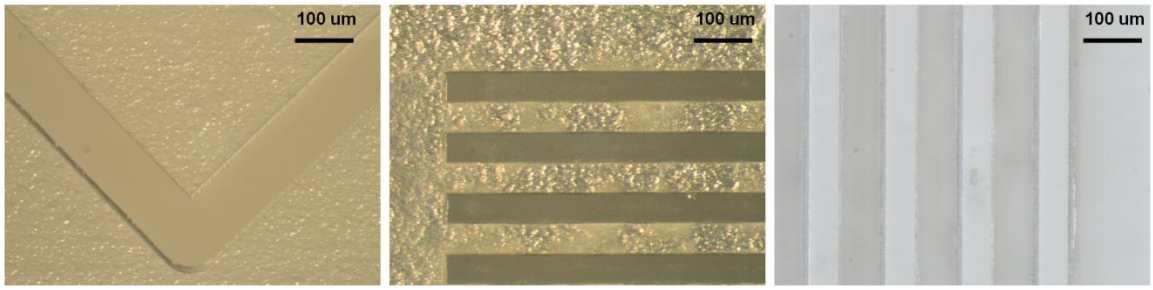

(a) (b) (c)

Figure 4.8 Micrographs of different screen materials tested for micropatterning of nanocomposite via laser ablation assisted screen printing. (a) magic tape; (b) removable tape; (c) PET film which is commonly used as screen protector. PET film was found to be the optimal choice of screen material.

With optimization of screen material and careful manipulation of laser ablation conditions, arbitrary geometries could be readily obtained on the film screen, since patterning was simply implemented by a CAD design and direct laser writing. As illustrated in SEM images in Figure 4.9, different demonstrative patterns were created on the PET film. Figure 4.9 (a) shows an array of evenly spaced square PET blocks (140 μm×140 μm blocks with 60 μm spacing) with a magnified view in 4.9 (b) revealing smooth side walls. Figure 4.9 (c) shows circular holes on PET film with a diameter of 210 μm, and 4.9 (d) an arbitrary path with channel width of 43 μm. These microstructures served as a mold for patterning PDMS-CNTs nanocomposite. Further, they could also be used as casting molds to fabricate microfluidic devices. In fact, when lateral resolution is not critical they proved to be a cost-effective alternative to photoresist molds fabricated by a more complex lithography process.

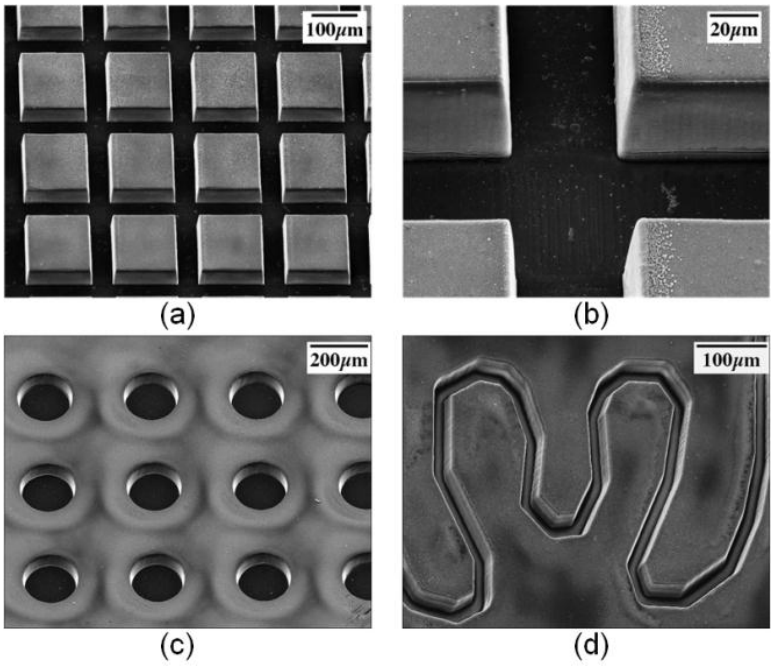

Figure 4.9 SEM images of micropatterns generated on a 59 μm-thick PET film via laser ablation: (a) an array of 140 μm×140 μm square PET blocks separated by 60 μm spacings; (b) magnified view of one intersection of the square blocks; (c) circular holes with 210 μm diameter and 190 μm pitch, and (d) arbitrary pattern with channel width of 43 μm.

4.3.4 Fabrication of embedded nanocomposite patterns

During the course of progressive research in this dissertation, two fabrication approaches were sequentially developed to use patterned PET screen and realize microstructures of polymer nanocomposite with the assist of laser ablation—with the first approach realizing micropatterns embedded in bulk polymer, and the second realizing protruding micropatterns above the surface of bulk polymer. Each of the two approaches held its own merits. In the first case, when compared with relief patterns (patterns above a PDMS surface) that could be formed, embedded patterns (patterns below a PDMS surface) were preferred for certain applications. For instance, the binding strength between the embedded nanocomposite and its host elastomer would be higher due to a

larger interfacial area. The improved adhesion would prove critical for sensor devices such as strain gauge where the deformation of bulk elastomer and conductive pattern needed to be identical. Also, when the embedded nanocomposite acted as an electrical contact pad in a microfluidic channel, it could avoid potential obstruction of flows [9]. Further, on a planar surface with both nanocomposite pattern and bulk elastomer, heterogeneous temperature and/or surface chemistry could be readily generated, if the nanocomposite were heated up [100-101].

4.3.4.1 Fabrication process

The overall process flow of embedding polymer nanocomposite micropatterns within bulk PDMS is illustrated in Figure 4.10. In the first step of laser ablation, a thin polymer film, such as PET film commonly used as screen protectors, was applied on a cleaned glass substrate and a focused laser beam ablated through the film following a path which was programmed using CimCAD software (developed by Cimex Corporation in Belchertown, MA). Then, prepared nanocomposite was filled into the open grooves of the PET film. Extra amount was removed by sliding a razor blade evenly across the film surface. Any remaining residual nanocomposite was removed with the lifting-off of film screen, leaving on substrate only the desired nanocomposite patterns.

The following processes were the same with the microcontact printing process. After partial curing of nanocomposite patterns (e.g., expose at 60^{o}C for 30 minutes) in a convection oven, bulk unmodified PDMS was poured on top of nanocomposite patterns. Since nanocomposite contained the same polymer matrix as the enclosing polymer, the interface was well connected by chemical bonding. After the whole device was fully cured, it was de-bonded from glass substrate, leading to sensor devices with

nanocomposite embedded in bulk PDMS. As mentioned above, since now each new design of pattern can be implemented with simply a 2-D CAD drawing and laser ablation in a matter of minutes, the preliminary testing of sensor with various designs could be greatly expedited.

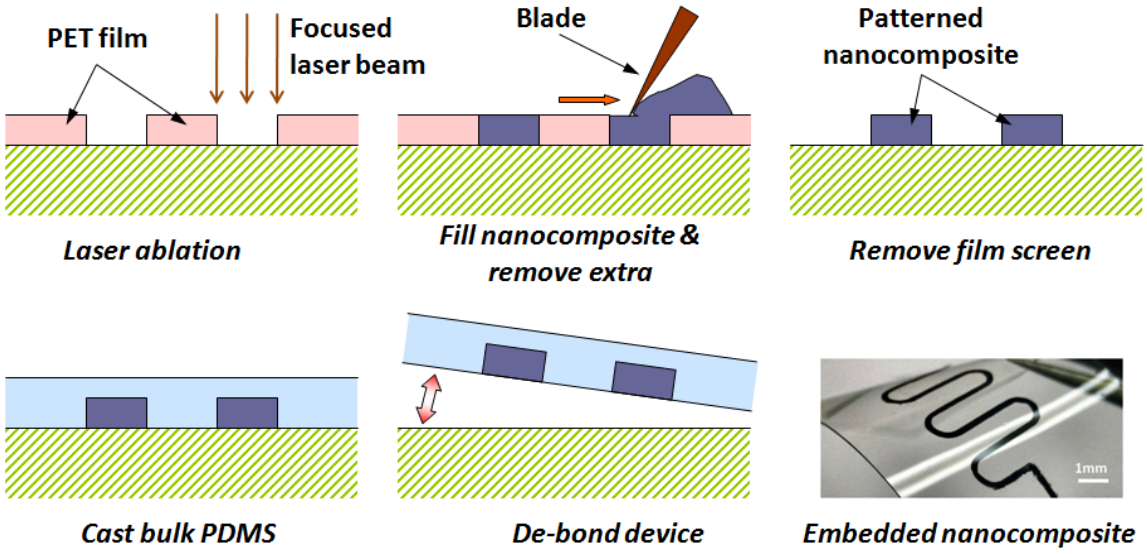

Figure 4.10 Schematic diagrams showing the fabrication process of nanocomposite patterns embedded in an unmodified PDMS block. Final image exhibited great mechanical flexibility of the fabricated all-elastomer device.

4.3.4.2 Patterning characterization

To characterize patterning uniformity, optical surface profiling was conducted on multiple PET screens and nanocomposite samples. To effectively illustrate the size evaluation, a film screen with ten parallel channels (around 100 μm-wide) was selectively shown in Fig. 4.11 (a). A viscous resin of nanocomposite containing about 9wt% of carbon nanotubes was filled into channels, with extra amount removed by a razor blade. After peeling off the PET screen, the correspondent nanocomposite lines was left on the glass substrate and thermally cured. The sample shown in Fig. 4.11 (b) and (c) was not

embedded into bulk PDMS, as its SEM imaging required gold coating on the surface. Also, optical profiling could not have been performed on a flat surface of an embedded sample.

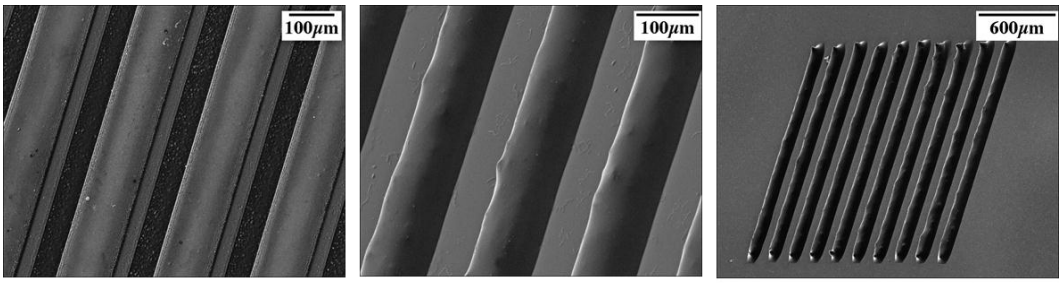

Figure 4.11 SEM images showing: (a) close-up view of a PET film screen with ten parallel open channels created via laser ablation (top width 115 μm and bottom width 96 μm); (b) correspondent view of nanocomposite lines (top width 61 μm and bottom width 151 μm) fabricated from screen on left, and (c) overall view of ten nanocomposite lines.

Surface morphology of the ten-line structures was mapped using an optical confocal profiler. Representative cross sections of the PET and nanocomposite are plotted in Figure 4.12 to compare their vertical geometries. The screen profile shows a smooth PET surface (roughness <0.4 μm) with open grooves, and the pattern profile displays nanocomposite lines matching screen. Also, statistical size information was compiled from all profiling data and summarized in Table 4.1.

The 58 μm-thick PET film was found to possess a slightly tapered sidewall profile (average top width 115 μm and bottom width 96 μm). As laser ablation is a process which strips polymer molecules off the film layer-by-layer from top to bottom, the upper portion of the film receives a higher dosage of photonic energy. Consequently, the top section of PET grooves turned out to be wider than the bottom. On the other hand, the patterned nanocomposite lines were measured to be relatively thinner and wider (average

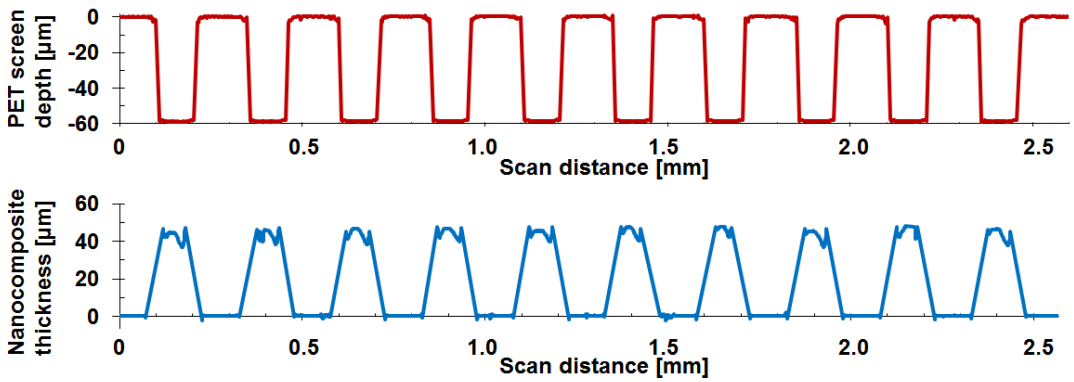

Figure 4.12 Optical profiling data of a representative cross section of the PET film screen with ten recessed trenches and its corresponding nanocomposite lines. Both screen and pattern lines had a pitch of 250 µm. Note: profiling data showed sharp edges at the top of nanocomposite lines, which was not necessarily the actual profile but rather caused by measurement limitations of the optical sensor. As the sensor head required reflected light from the surface to accurately record thickness, highly sloped surfaces and/or sidewalls sometimes could not be read correctly. From the SEM image in Fig. 6, the nanocomposite lines had a mostly smooth rounded top surface.

Table 4.1 Statistical summary on the size of PET mold and embedded nanocomposite patterns using all data obtained from optical surface profiling. Lateral scanning steps during optical surface profiling: X axis (perpendicular to lines) = 1 µm, Y axis (parallel to lines) = 100 µm.

	PET film screen	**Nanocomposite**
Bottom width (µm)	**114.8**	**150.8**
Variation (±%)	2.4	2.6
Top width (µm)	**96.4**	**61.4**
Variation (±%)	1.7	10.7
Thickness (µm)	**58.4**	**44.2**
Variation (±%)	1.6	12.1

top width 61 µm, bottom width 151 µm and thickness 44 µm), which meant that during the thermal curing process of nanocomposite, the viscous resin spread sideways before it was fully solidified. While the spreading effect could potentially limit the patterning resolution, careful tailoring of nanocomposite resin viscosity and curing conditions could

further decrease its minimal feature size. Nonetheless, both the PET screen and nanocomposite exhibited uniformity with all size variation less than 3% and 13% respectively. Profiling of multiple screen-pattern sets confirmed the consistency of the characterization data. Overall, this laser ablation-based patterning approach proved to be a reliable method to embed nanocomposite microstructures.

4.3.5 Fabrication of relief nanocomposite patterns

In the fabrication protocol discussed above, the PET screen was removed after filling of polymer nanocomposite in order to realize embedded micropatterns. Although this approach was simple and reliable, one lingering drawback was its limited lateral resolution due to the spreading of polymer resin during its curing stage. Not only the spreading affected the patterning resolution, it also contributed to variations in nanocomposite dimensions (thickness, width). In order to overcome these issues, the fabrication process was modified to realize not embedded patterns, but relief patterns.

4.3.5.1 Fabrication process

The process flow of fabricating relief patterns was somewhat similar to the previous approach. Briefly, as illustrated in Figure 4.13, a PET film (common screen protector) was first applied onto a glass substrate. An excimer laser beam ablated through the film following a path programmed according to the pattern design. Then, the whole surface was placed over the mouth of a glass beaker filled with chlorotrimethylsilane, and was treated with vapor for around 5 minutes. Afterwards, the prepared PDMS-MWCNTs nanocomposite was filled into the open grooves of the PET film. Extra amount was removed by sliding a thin and smooth-edged object (e.g. razor blade or silicon wafer) evenly across the surface. Here lied the biggest difference between this approach and the

previous one—instead of removing the PET film, it remained on glass surface since its surface was smooth with roughness less than 0.4 μm, the nanocomposite could be easily removed with only a negligible trace left. Then, bulk PDMS resin was poured on top of the micropattern and fully solidified through thermal curing. Finally, device was debonded from the glass substrate. Due to the high compatibility of nanocomposite with bulk PDMS, the relief patterns were firmly attached to the surface of bulk PDMS. An important advantage of this fabrication process lies in the fact that each new pattern design is simply implemented with a 2-D CAD drawing and laser ablation in a matter of minutes, thereby expediting the process of device manufacturing.

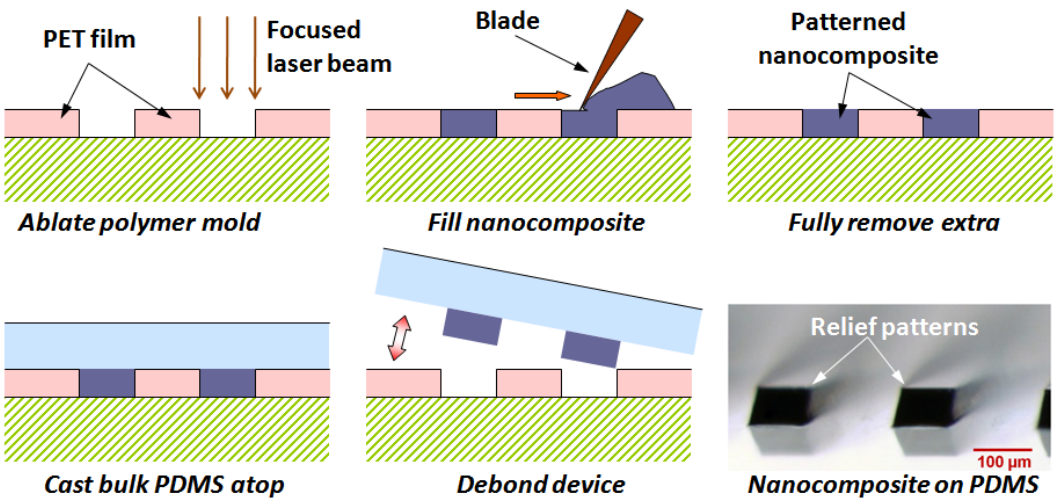

Figure 4.13 Schematic diagram showing the fabrication process of nanocomposite patterns. The micrograph shows relief patterns lying on the smooth surface of pristine PDMS.

4.3.5.2 Patterning characterization

Using the ablated PET film as a filling mold which was not removed, PDMS-MWCNTs nanocomposite containing around 7wt% of carbon nanotubes was patterned at a higher resolution than the embedded approach. Figure 4.14 (a) demonstrates a 34 μm-

wide and 58 µm-thick nanocomposite zigzag line on a pristine PDMS surface. Figure 4.14 (b) shows a closed-up view of turning sections which display excellent side wall profile. Further, as in figure 4.14 (c) a zigzag line with width as small as 19 µm was achieved. This minimal feature size presented a major improvement not only from previous reports of using laser ablation to pattern polymer composite but had resolution topped around 100 µm [99], but also from our own previous version of embedded patterning.

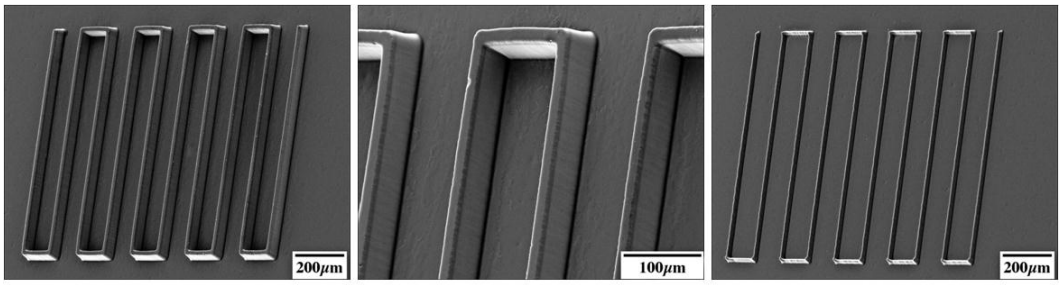

Figure 4.14 SEM images of PDMS-MWCNTs nanocomposite relief patterns on a PDMS surface: (a) zigzag line with 58 µm thickness, 34 µm width, 1 mm long turns and 150 µm short turns; (b) magnified view of a turning section of pattern in (a), and (c) zigzag line with 58 µm thickness and only 19 µm in width.

As mentioned above, complex geometries can be readily patterned on PDMS surface using our presented technique. For visual demonstration, the mysterious pattern of the spider lines in the Nazca Desert in Peru was mimicked on a micro-scale on a PDMS surface, as shown in Figure 4.15. The micro-spider measuring merely 3 mm across easily fit on a fingertip. It had 44 µm-wide skeletons which were composed of polymer nanocomposite.

In addition to demonstration of high resolution patterning of arbitrary geometries, we also performed dimensional characterization of multiple PET film molds and

nanocomposite patterns. We believed that the authenticity and uniformity of micropatterns reflected the reliability of our fabrication technique. In order to effectively illustrate the size evaluation process, a PET mold with ten parallel channels (each 2 mm-long and 106 μm-wide) was selected as shown in figure 4.16 (a)—similar to the previous patterning methodology in Section 4.3.4.2. Its corresponding nanocomposite pattern (figure 4.16 (b)) was manufactured via the aforementioned protocol.

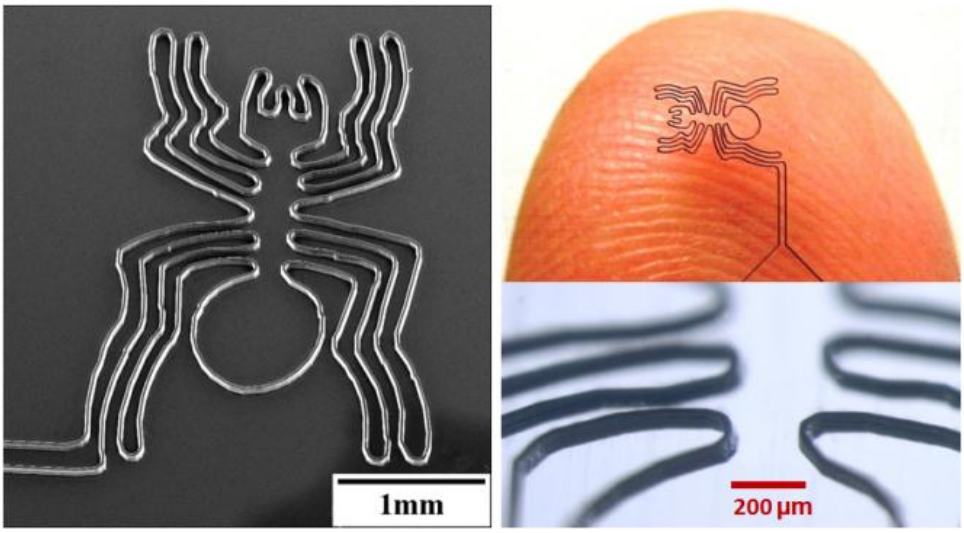

Figure 4.15 Different views of a "Micro Nazca Spider" on a bulk PDMS surface: SEM image showing spider-shaped relief pattern with 44 μm-wide PDMS-MWCNTs nanocomposite lines as its skeleton (left); the 3 mm-long spider pattern fitting on a fingertip (upper right), and micrograph showing details of the skeleton and the sharp contrast between the black nanocomposite and transparent PDMS surface (lower right).

In our experiment, the surface morphology of the ten-line structures was mapped using an optical profiler. Representative cross sections of the PET mold and nanocomposite pattern are plotted in Figure 4.17 to compare their vertical geometries. While the mold profile shows a smooth PET surface with ablated grooves, the pattern profile displays a flat PDMS substrate with nanocomposite relief patterns matching

trenches of the mold. Furthermore, statistical size information was compiled from all profiling data and summarized in Table 4.2. Tapered sidewall profiles were found in both mold (top 106 μm and bottom 93 μm) and nanocomposite (top 92 μm and bottom 113 μm). The average width of nanocomposite patterns was slightly higher than that of the mold with the larger and smaller ends reversed. Also, their thickness/depth was nearly identical (mold 59 μm and nanocomposite 58 μm). The dimensional authenticity from mold to pattern indicated a reliable replication process. Moreover, the size of nanocomposite exhibited excellent uniformity varying less than 4% in width and 2.5% in thickness. Profiling of multiple mold-nanocomposite sets confirmed the consistency of characterization. Overall, this laser ablation-based patterning approach proved to be a reliable method to realize high resolution nanocomposite microstructures.

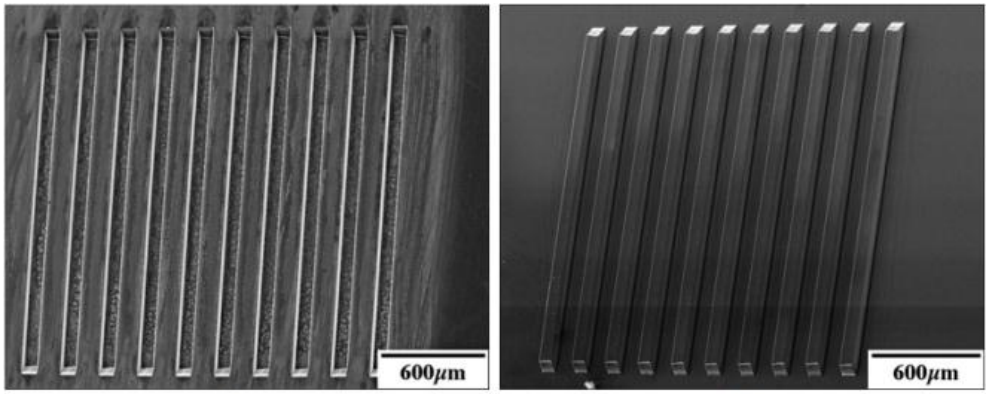

Figure 4.16 SEM images for size characterization: (a) PET film mold with ten recessed channels created via laser ablation and (b) ten relief lines of PDMS-MWCNTs nanocomposite fabricated from mold on left.

An interesting feature of the PET mold, and consequently the nanocomposite pattern, is again its slightly tapered sidewalls—an inherent attribute of laser ablation. Since

ablation is a process which strips polymer molecules off the film layer-by-layer from top to bottom, the upper portion of the film receives a higher dosage of photonic energy. As a result, the top section of PET grooves tends to be wider than the bottom section. Similar effects occur in lithography of photoresist where higher UV exposure in the upper region leads to more cross-linking of negative resist and thereby tapered sidewalls. In fact, compared to a strictly vertical sidewall, the tapered profile is beneficial to the debonding of nanocomposite patterns from the PET mold as it helps to reduce friction along the interface and lower structural stresses [102]. On the other hand, the tapered feature places a potential limit on the patterning resolution. Given a certain PET film thickness, if the desired width of trench were too small, laser may not penetrate through the full depth of the film. In other words, higher resolution of patterning can be obtained with thinner polymer films.

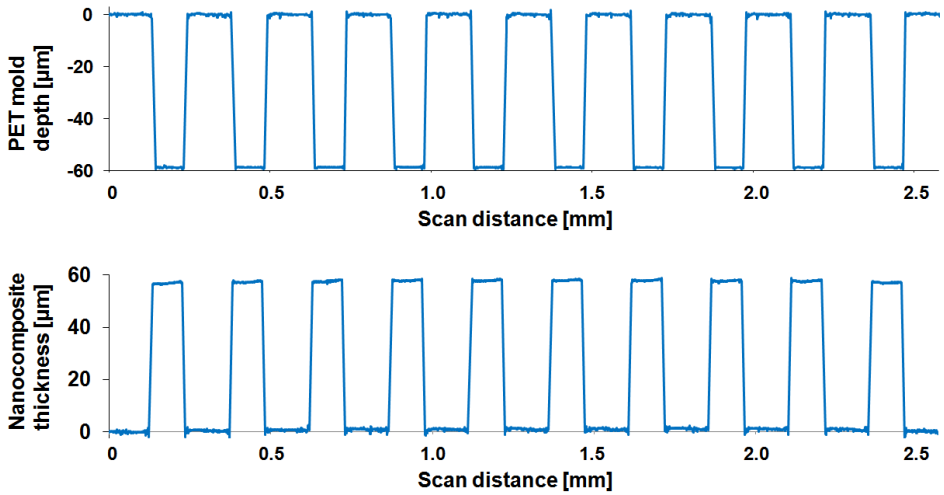

Figure 4.17 A representative cross section of a PET mold and corresponding nanocomposite pattern consisting of 10 parallel lines. Lateral scanning steps during optical surface profiling: X-axis (perpendicular to lines) = 0.25 µm; Y-axis (parallel to lines) = 180 µm.

Compared with embedded patterning, the relief pattering protocol discussed above has improved significantly in lateral patterning resolution. This is due to the fact that polymer resin could not spread outward anymore as PET mold is in place to hold it. Another consequential advantage is the much improved dimensional uniformity, with variation decreased from about 13% to less than 4%. In addition, yield of fabrication was also high using the relief patterning protocol, reaching around 70%-80%. Therefore, in spite of the potential advantages embedded pattering holds over relief patterning, the later should be considered to be an upgraded microfabrication protocol.

Table 4.2 Statistical summary on the size of PET mold and nanocomposite relief patterns using all data obtained from optical surface profiling.

	PET mold	**Nanocomposite**
Bottom width (μm)	**106**	**113**
Variation (±%)	1.0	3.5
Top width (μm)	**93**	**92**
Variation (±%)	2.2	2.3
Thickness (μm)	**59**	**58**
Variation (±%)	1.4	2.4

4.3.6 Resistive uniformity of micropatterns

It has been mentioned that a uniform dispersion of CNTs in PDMS is essential in realizing micropatterns with consistent conductivity. To test the effectiveness of micropatterning technique, the resistance of four microstructures with slightly different dimensions was measured. As summarized in Table 4.1, repeatable resistance was yielded, with a variation of about ±8%, thus proving consistency of conductivity and proving the effectiveness of this patterning technique.

Overall, from the above mechanical and electrical characterization of the laser ablation process, it was proven to be a reliable approach of patterning nanocomposite. With continuous effort to optimize its processing conditions, the overall performance could be further enhanced in terms of patterning uniformity and resolution.

Table 4.3 Comparison of resistances of four micropatterns (thickness 45 μm, width 250 μm, lengths varying from 5-9 mm) [103]. For uniformity computation, resistance was normalized based on a unit length of 1 mm.

Sample number	**#1**	**#2**	**#3**	**#4**
Normalized resistance per unit length	1.05	0.92	0.99	1.04
Variation (%)	5.1	-8.1	-0.9	3.9

4.3.7 Discussion

In addition to patterning of polymer nanocomposite, serving as an alternative to photolithography, laser ablation is a general micropatterning technique which can realize molds on a polymer film instead of a photoresist. Other than fabricating nanocomposite microstructures, it has other interesting applications as well [89, 104–110]. Figure 4.13(a) shows a simple prototype of zigzag microfluidic channel working as a passive mixer for colored dye solutions. This channel was made by double-casting PDMS from a laser ablated PET film mold. Figure 4.13(b) illustrates an arbitrary patterned channel shaped like a “Nazca Spider” and filled with dye solutions. These examples are indicative of the potential applications of the laser ablation patterning technique in a variety of areas such as microfluidics and lab-on-a-chip systems.

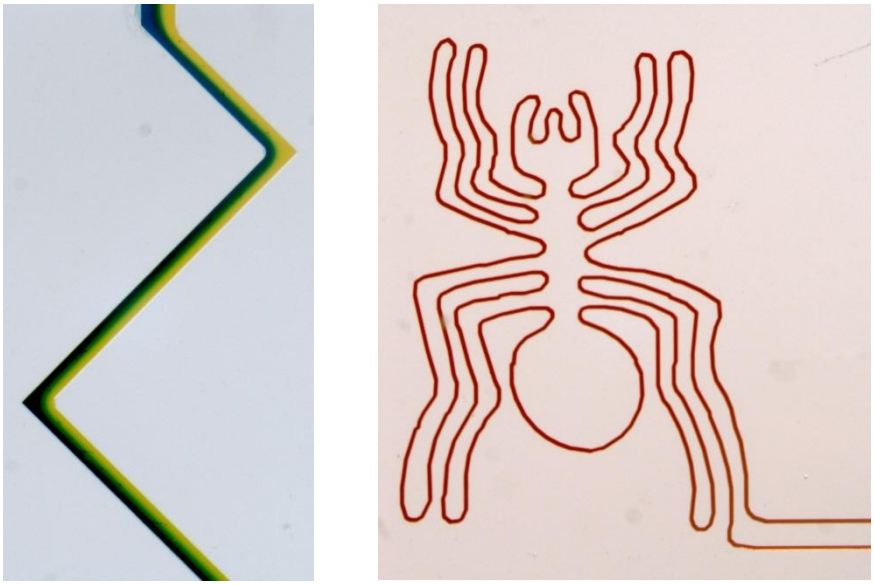

(a) (b)

Figure 4.18 Optical micrographs of microfluidic channels made via laser ablation of PET film. (a) Zigzag PDMS channel (200 μm wide) working as passive mixer of dye solutions; (b) Nazca spider patterned channel (31 μm wide) filled with red dye solution.

4.4 Summary

Overall, the three proposed micropatterning techniques discussed in this chapter were characterized to be reliable protocols of realizing microstructures of polymer nanocomposite. Compared with previously reported techniques, in microcontact printing the ability to repeatedly use the pre-manufactured printing mold significantly simplifies the fabrication process; in laser ablation assisted screen printing new designs of pattern could be readily implemented by CAD software instead of the complicated process of photolithography.

Certainly there are limitations with each of the proposed patterning techniques. For instance, microcontact printing still relies on a pre-manufactured printing mold, therefore

it requires a new mold for each different design of sensor device; laser ablation assisted screen printing still involves a labor intensive process of manual filling and removing of nanocomposite which is undesirable in mass production of devices. Nonetheless, regardless of their respective drawbacks, the proposed protocols display significant improvement over prior techniques and yield promising potentials in the development of microfabrication techniques for conductive polymer nanocomposites.

CHAPTER 5: SENSOR APPLICATIONS BASED ON MICROPATTERNED POLYMER NANOCOMPOSITE

5.1 Introduction

Due to the unique combination of mechanical flexibility and electrical piezoresistivity, polymer nanocomposite composed of PDMS and MWCNTs presents an intriguing material as sensors for a wide range of potential applications. For example, when using PDMS-MWCNTs nanocomposite as a physical sensor, it could be exposed to a variety of different mechanical stimulus or deformations (e.g., a tensile strain, compressive strain, normal stress, shear stress, etc.). Consequently, the geometry (i.e., 3D shape of each carbon nanotube), interconnection, and distribution of carbon nanotubes within the polymer matrix vary accordingly, all of which may lead to a change in its overall electrical resistance. The overall resistance change is a net reflection of a large number of micro or nano-scaled resistance changes of individual carbon nanotubes. Similarly, mechanical stress (e.g., normal stress applied to a sensor surface such as a diaphragm) imposed on the sensor can also impact geometry and/or distribution of MWCNTs within the nanocomposite and thereby alter the overall resistance.

To demonstrate the feasibility of using PDMS-MWCNTs nanocomposite for various sensing applications, in this chapter, prototypes of two sensor types including strain and pressure sensors are selectively constructed and analyzed. In following sections of this chapter, detailed discussions regarding their sensing principles, fabrication process, characterization of their sensing performance will be carried out. Further, in-depth discussion of their advantages and potential limitations will be carried out. Other sensing

formats may apply same or similar principles and techniques employed in developing strain and pressure sensors.

5.2 Large range strain sensor prototype

5.2.1 Sensing principle

The basic principle of strain sensing has been discussed in detail in Chapter 2. Simply, for a polymer to be electrically conductive, nano-scaled fillers must either physically touch to form electron conducting path, or be sufficiently close to each other to allow electron transfer via "tunneling effect" [60]. Therefore, the conductivity of the PDMS-CNTs nanocomposite system is dictated by the number of interconnection nodes and distances between neighboring carbon nanotubes. When a uniaxial tensile strain is applied to a nanocomposite strain sensor, carbon nanotubes are separated apart, leading to loss of contact points and widening of inter-tubular distances. This impedes the electron transferring ability of the conductive network and causes overall resistance to rise. Similarly, when nanocomposite is relaxed electron conduction paths are restored, therefore resistance drops along with decreasing strain.

Since PDMS-MWCNTs composite possesses superior flexibility when compared with other polymers, it is especially fitting for strain sensors which require large range sensing capabilities. In the field of biomedical diagnosis, for instance, some biomechanical strains could mandate the strain gauge to withstand strain over 20% [6], which is difficult for any other types of strain sensor but easily achievable with PDMS-based ones. As shown in Figure 5.1, various micropatterns of strain sensor are designed and manufactured. All of these devices displaying excellent mechanical flexibility, able

to be attached to any arbitrarily curved surfaces which may be necessary in some biomedical sensor applications.

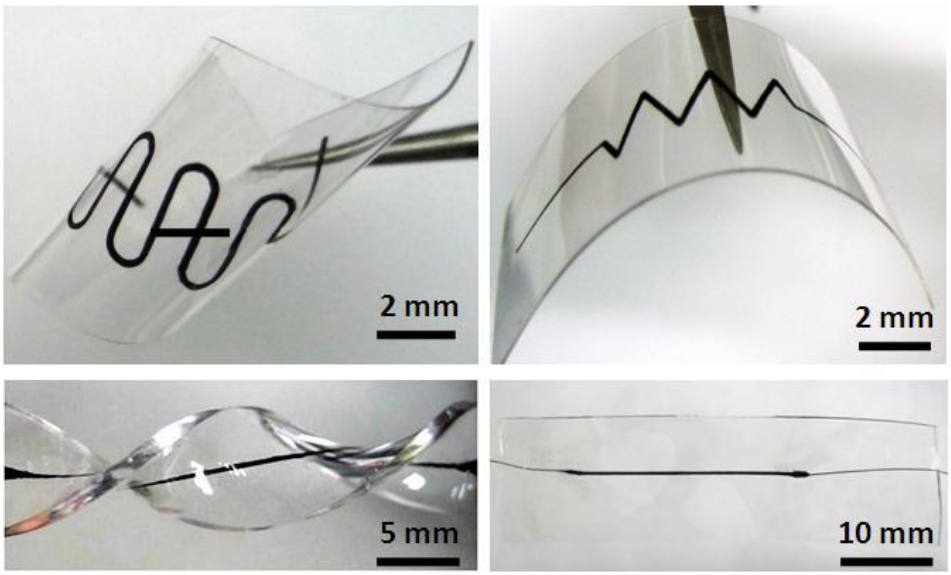

Figure 5.1 Microfabricated PDMS-MWCNTs composite strain sensor samples with different microstructure designs including serpentine, zigzag and single line patterns. Illustrated embedded nanocomposite patterns are around 250 μm-wide, 50 μm-thick, and a few cm in length. PDMS thin films were generally a few hundred μm in total thickness.

5.2.2 Experimental setup

During the initial stage of our experiments, strain sensors were exposed to tensile strains manually. Later improvement was made to the configuration of the experimental setup. As illustrated in Figure 5.2, elastomer samples embedded with nanocomposite patterns were firmly fastened by two metal grips: one end fixed to a static position, and the other to an automated motion stage. The position of motion stage is numerically controlled by a computer, therefore the displacement and strain of samples are known at any given time. Two-probe electrode connections were made at both ends using copper/gold wires or cut-out aluminum films. As samples were stretched and relaxed on

the motion stage, its resistance was measured in real time using a digital multimeter with RS-232 PC interface.

Since resistance does not depend on frequency, the DC resistance measurement offered by the digital multimeter would provide the same result with alternative current (AC) measurement. Further, capacitance of the nanocomposite patterns between two end electrodes was negligible compared to the resistance, which was on the order of mega-ohms. For example, for a strain gauge sample that was 44 mm-long, 500 μm-wide, and 50 μm-thick, according to the capacitance equation: $C = \varepsilon_r \varepsilon_0 \frac{A}{l}$, the capacitance of the strain gauge would be 5 pF (if dielectric constant ε_r equals 1), or 0.5 nF (if $\varepsilon_r$equals 100 which is regarded a high value). Considering the insignificance of the capacitive component compared to the resistance component of the nanocomposite samples, direct resistance measurements were conducted instead of impedance measurements. In addition, to ensure the consistency of testing and prevent buckling of device, the applied tensile strain was kept at zero or positive throughout experiments.

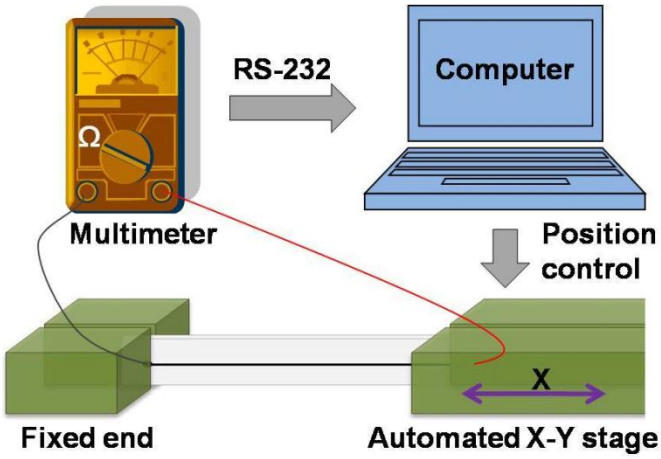

Figure 5.2 Schematic diaphragm showing experimental setup of strain sensor testing which allows simultaneous recording of strain and resistance values on PC.

5.2.3 Resistive response under single rising strain

For demonstration purpose, the simplest pattern of a single line along the strain axis was used for testing and representative responses were plotted in Figure 5.3. In this case, two single line patterns of PDMS-MWCNTs (containing around 9 wt%) shared similar dimensions—both 44 mm-long and around 50 μm-thick. Relatively large widths (sample A ~600 μm and B ~900 μm) were used to fit the measuring range of the ohmmeter (max 44 MΩ). When sample A and B were elongated to as high as 45% of tensile strain, their relative resistance increased by 78% and 103% respectively.

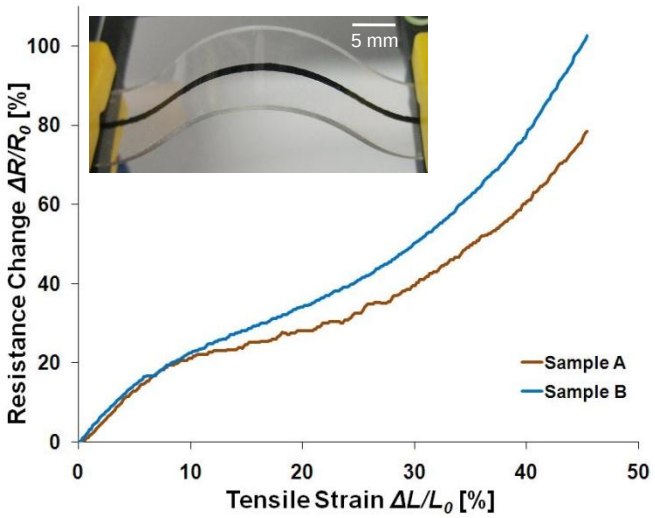

Figure 5.3 Strain-dependent resistance of two nanocomposite samples embedded with single line patterns. Under an applied maximum tensile strain of 45.5%, sample A and sample B had a relative increase of 78% and 103%, respectively, in their resistance readings. Inset shows an image of sample B (~900 μm wide) and sample A is similar but thinner (~500 μm wide).

Other tests of nanocomposite with different dimensions (thickness, width) also revealed similar resistive responses. The variation of response across devices could be attributed to the dispersion quality of carbon nanotubes, which might not be perfect on

the molecular level. Overall, although the resistive responses were not perfectly linear with tensile strain, the overall sensing factor, defined by the ratio of $\Delta R/R_0$ and strain ε, was found to be around 2 which is comparable to that of some conventional strain gauges [26].

5.2.4 Resistive response under cyclic strains

To further characterize the strain-dependent resistance of nanocomposite devices, multiple cycles of stretching and relaxing were carried out on the automated motion stage at a constant strain rate (4 mm/min). During testing some initial time dependence of resistance was observed, which was also reported in literature [111], nonetheless, the resistive response was found to be very consistent when system reached an equilibrium state. Repeatable resistance change occurred over tens of cycles. Figure 5.4 shows 12 cycles extracted out of 30 indicating that upon loadings of tensile strain between 0 - 42%, the resistance varied from about 2.7 MΩ to 4.5 MΩ—a relative change of 63% [96]. It should be noted that the cyclic response was a little less sensitive than the previous case of single rising strain, possibly because in dynamic testing resistance did not have sufficient time to fully settle down to a stabilized value. As mentioned before, the ability of PDMS-based composites to endure repeated large deformations without any mechanical failure presents a potential advantage over other strain sensing materials. The samples were found to reach fatigue after testing for extended cycles (around 250-300 cycles) of loading and unloading. When sample reached fatigue, its resistance change showed erroneous trends. For example, it showed sudden resistive spikes in the middle of the unloading cycles.

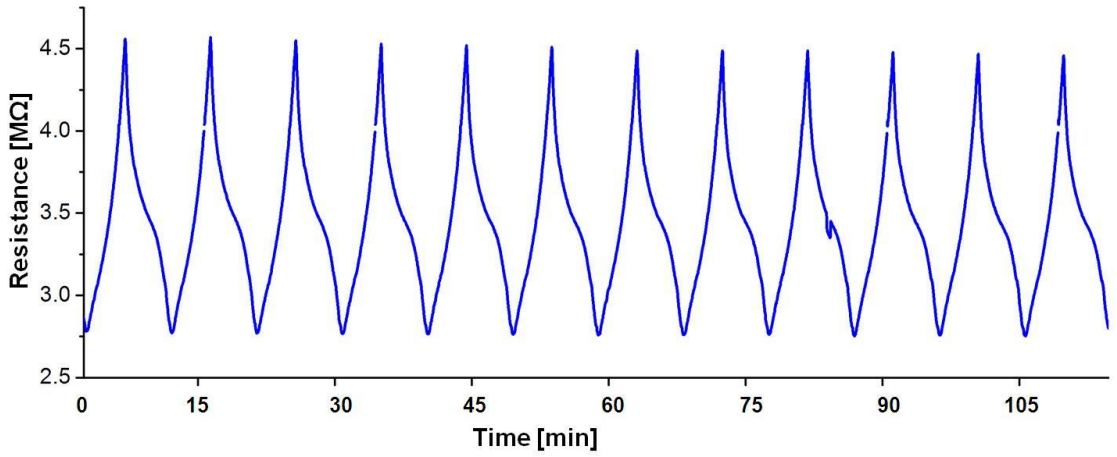

Figure 5.4 Measured electrical resistance of nanocomposite (sample B) over time under cyclic loadings of tensile strain. During each cycle, strain increases linearly from 0% to 42% in 4.5 minutes, and 12 testing cycles are extracted to reveal the repeatability of resistive response.

5.2.5 Hysteresis effect

Through analysis of the strain response curves, it was evident that resistance change in the sample relaxing phase was not the reversal of that in the stretching phase. In fact, an interesting hysteresis effect was found by extracting data from a loading cycle, which is shown in the inset of Figure 5.5 To verify the pattern of hysteresis, sample was exposed to cyclic extensions with same strain rate but increasing levels of maximum strain (7 levels from 2.3% to 42.2%). One cycle of resistive response data from each strain range were extracted and plotted as in Figure 5.5. Measurement results confirmed similar hysteresis patterns regardless of strain range. In additional experiments, different strain rates were applied onto the sample while the strain range was kept constant, and similar hysteresis patterns were still observed, further confirming the validity of this observation.

Of the seemingly peculiar hysteresis patterns, three aspects were easy to notice. One was that, when sample strain just dropped to zero and started to increase again, resistance actually showed a small decrease before it resumed rising. This phenomenon was particular to cyclic tests whereas sample resistance immediately increased following strain change with a single run of increasing strain (or first loading cycle) as shown in Figure 5.3. Although the underlying mechanisms are not well understood at this time, one possible explanation is that carbon nanotubes could not settle down immediately after a strain change. Since the PDMS-MWCNTs nanocomposite is composed of nano-scaled tubular structures entangled in a complex network of polymer macromolecules, carbon nanotubes continue to move around and interact with neighboring nanotubes in the elastomer matrix to minimize the internal stress of the elastomer. This is a reasonable assumption as Junisbekov [112] pointed out that, at any given strain, the internal stress of a viscoelastic material tends to decrease over time—a process referred to as stress relaxation.

Here, to experimentally verify the stress relaxation effect inside polymers, an unmodified PDMS rectangular block was held to a certain strain level, and its stress was recorded with time on a dynamic mechanical analysis system (DMA, TA 2000ex Rheometer), as shown in Figure 5.6. Although there lacked a mathematical model of polymer mechanics to accurately predict the pattern of stress relaxation, the stress was found to decrease with time in a logarithmic fashion.

Meanwhile, a positive relationship between the resistance of nanocomposite and its internal stress has also been reported in other studies [68-69]. Therefore, at any given

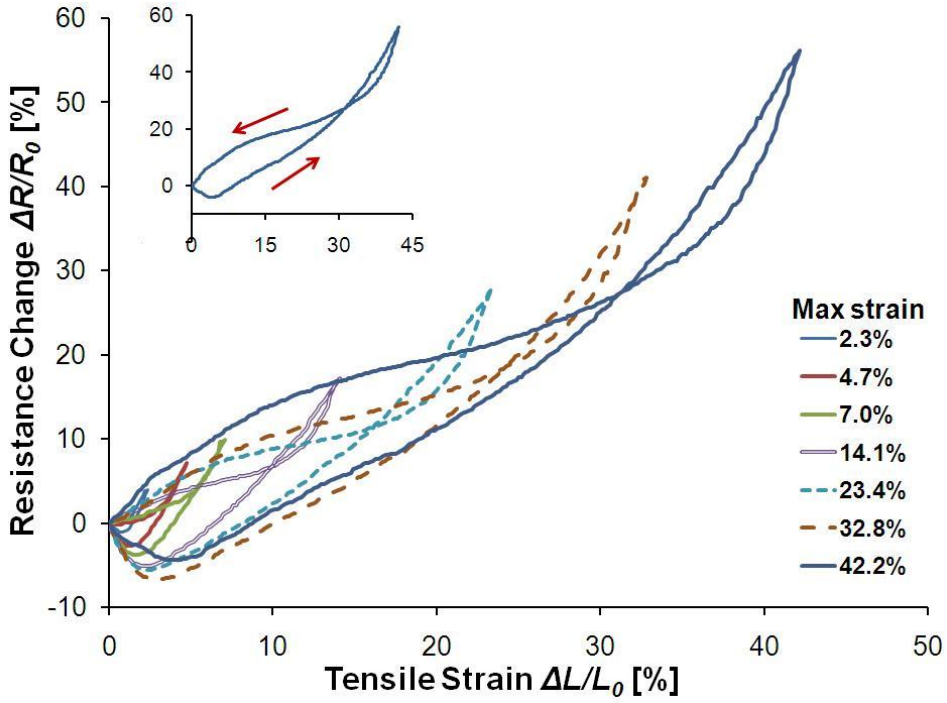

Figure 5.5 Resistive response of nanocomposite under cyclic loadings of different ranges of tensile strain. Consistent similar hysteresis effect was observed from each range. Inset shows the direction of resistance change in the stretching/relaxing phases of testing with maximal strain at 42.2%.

time during our repeated strain tests, the stress relaxation of nanocomposite could have also caused its resistance to drop along with internal stress. In order to test if resistance reveal a similar relaxation effect in regard to time, a strain sensor was fixed at different strain levels while its resistance recorded over time with a multimeter, as shown in Figure 5.7. Interestingly enough, the resistance of strain sensor gradually decreased with time. When the time was changed into log scale, the resistance showed a mostly linear relationship with log of time, which was quite similar to the stress relaxation effect in PDMS. Various other mathematic curves were also tested to fit the time decay of the resistance, which included various forms of linear functions, exponential functions, polynomial functions, hyperbola functions, rational functions, as well as other

appropriate candidate functions. Empirical fitting results revealed that the logarithmic fitting was the only curve that matched consistently with different samples and over different lengths of time periods. As shown in Figure 5.8, the logarithmic decay trend was confirmed to last for as long as 30 hours without settling to a constant point, as continuous monitoring of resistance suggested. However, despite extensive experimental confirmation, likewise the stress in polymer, no reliable mathematical model is yet available to verify the validity of the logarithmic relaxation of resistance. Nonetheless, these empirical observations did suggest a potential strong correlation between the resistance and stress of polymer nanocomposites. Validity of the logarithmic relaxation of resistance will be further discussed later in this chapter.

Using the hypothesis of correlation between resistance and stress, the first interesting feature in the hysteresis pattern could be attempted to be explained. When the sample just entered a stretching phase following a relaxing phase, the external force momentum was reversed at zero strain and the stress relaxation effect could become more significant. On the other hand, the resistance increase caused by separation of carbon nanotubes may be relatively low at small strains. Combining these two factors, a temporary decrease in resistance reading was reasonable to occur. After strain increased up to a few percent, however, the continuing separation effect might eventually outweigh the attenuated stress relaxation leading the overall resistance to resume rising again. Also it was noted in experiment that, when strain rate was higher, the temporary resistance decrease tended to be of less magnitude. The reason behind this could be that the stress relaxation process in this case was outmatched more quickly by the faster separation of carbon nanotubes causing resistance to rise sooner.

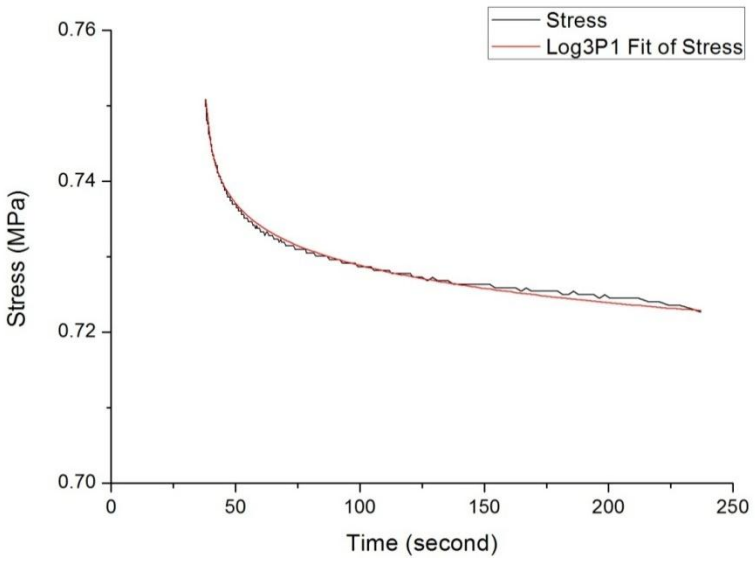

Figure 5.6 The internal stress of a PDMS block with regard to time when held to a constant 36% tensile strain. The logarithmic function used in curve fitting followed an empirical formula in the form of: $\delta = a - b \cdot \ln(t + c)$, where δ denotes stress, t denotes time of stress, and *a*, *b*, *c* are constants.

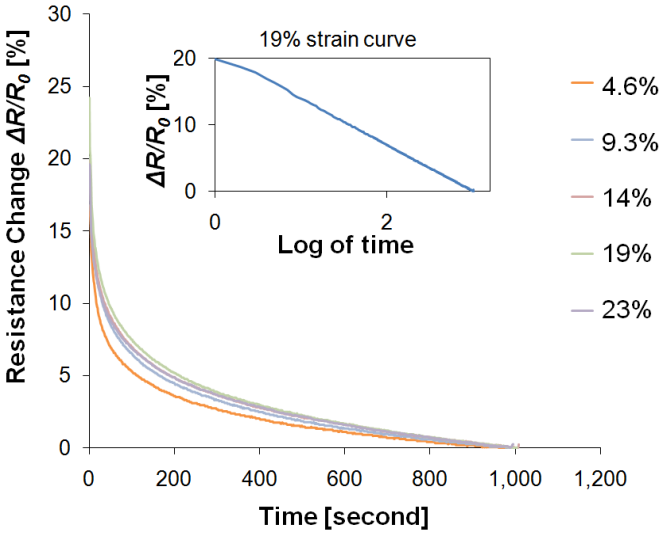

Figure 5.7 The resistance change of a strain sensor when it was fixed to different levels of strain for a certain period of time. Inset: resistance change shows a linear relationship with log-scale time, similar to the stress decay trend in a PDMS block.

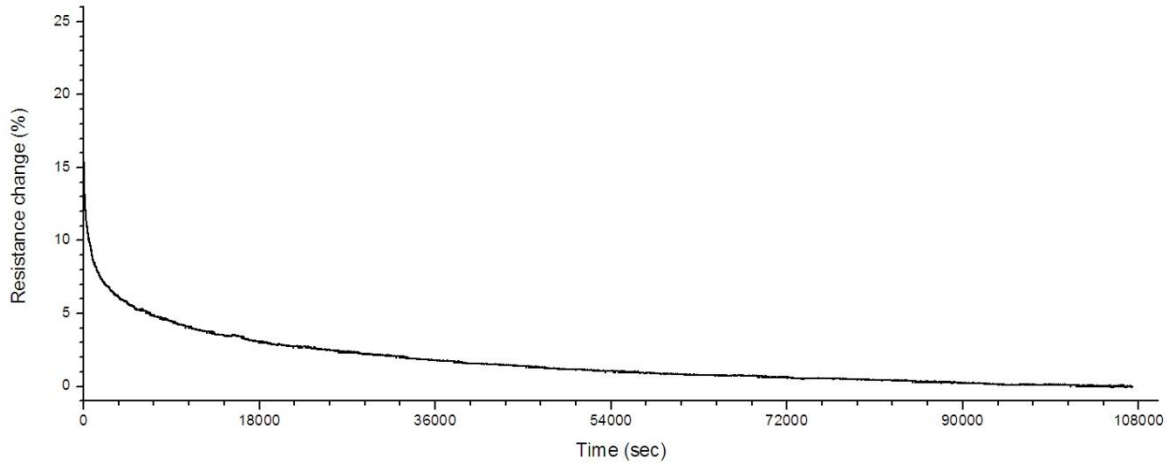

Figure 5.8 The resistance change of a strain sensor fixed to 23% of tensile strain for a period of 29.82 hours. The resistance changed in a logarithmic fashion, dropping from 1.842 to 1.473 MΩ.

Another observation of the hysteresis was the pattern of resistance change during relaxation phase. Resistance tended to drop more quickly right after strain decreased from the maximum level, then after a certain crossing point, it started to decline at a lower rate. While the reason for this pattern is still being studied, the PDMS molecular chains could be under taut condition with an increasing strain [113]. When strain was reversed at its top level, the sudden change in external force momentum could cause the polymeric chain force to decrease almost instantly and lead to a rapid drop in the internal stress. Plus, now that the stress relaxation and space-narrowing effects of carbon nanotubes both contributed to the decline of resistance, a relatively fast drop was reasonable to occur.

Finally, upon repeated tests of nanocomposite, its resistive response seemed to become less sensitive at higher strain ranges. Similar change pattern of stress was also reported, and it was reasoned via the Mullins effect, arguing that repeated tests could partly soften filled polymers [27]. Lower internal stress at same strain levels could be

yielded and, in our case, possibly less sensitive resistance response. With an increasing number of repeated tests at high strain levels, the nanocomposite strain sensors eventually showed signs of fatigue. Resistive response became somewhat irregular, for instance, not returning to base resistance or showing small spikes during the relaxing stage.

5.2.6 Analysis of stress and strain of nanocomposite

Because of the complex nature of the nanocomposite material and the fact that hysteresis could have three sources which are PDMS, carbon nanotubes and its composite form, further experiments were conducted to gain a better understanding of the complicated relationships between the stress, strain and resistance of the nanocomposite.

Firstly, bulk nanocomposite samples were tested using a rheometer (TA 2000ex Rheometer), which was capable of recording strain and stress simultaneously. The bulk samples were used instead of micropatterned nanocomposite samples, because no interface between nanocomposite and pristine PDMS was present in a bulk nanocomposite, therefore stress could be attributed entirely to mechanical deformations of nanocomposite. In addition, a multimeter was connected to two ends of the nanocomposite samples to record its resistance simultaneously. The configuration of measurement system is shown in Figure 5.9, with a bulk composite sample being affixed between two fixtures. After setting up the testing system, firstly a linear tensile displacement (at rate of 0.2 mm/sec, from 0 to 6 mm) was applied from two ends of the nanocomposite sample, resulting in a linear tensile strain from 0 to 32%. Cycles of loading and unloading were tested repeatedly, obtaining time variation of stress and resistance, which will be analyzed below. Firstly, representative results of stress change is shown in Figure 5.10.

Figure 5.9 Image showing the configuration of a testing system for strain, stress and resistance. A bulk PDMS-MWCNTs sample (small black object in center, dimensions: around 18.8×11.9×0.43 mm) was affixed between two fixtures of the rheometer.

As shown in Figure 5.10, the bulk nanocomposite sample was applied with three cycles of loading and unloading before subjecting to stress relaxation at a tensile strain of 32%. Herein, the stress relaxation part will be analyzed firstly, followed by a discussion of the loading/unloading cycles. Figure 5.11 illustrates the decaying trend of the stress relaxation with time, showing a time in logarithmic scale. It can be clearly seen that the stress of the bulk nanocomposite decayed in a logarithmic trend, as it showed a near-perfect match with a linear fitting curve in the Log Time scale. This result is consistent with previous discussions with respect to the stress relaxation of pristine PDMS shown in Figure 5.6, indicating that regardless of the presence of filling materials, PDMS would demonstrate a stress relaxation in a logarithmic fashion.

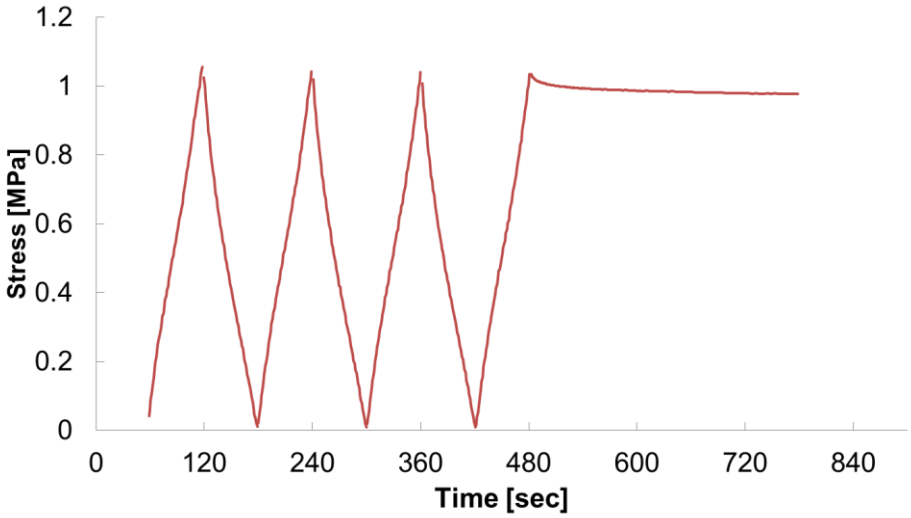

Figure 5.10 Stress change of a bulk nanocomposite sample with time when under repeated loading and unloading of strains. Final section shows stress relaxation at a fixed strain of 32%.

Although somewhat counter-intuitive to imagine the existence of a logarithmic decay with time (instead of an exponential decay which is widely known), this behavior of stress in polymers and other materials has been revealed by various prior studies. R. Andrews *et al.* reported that in an elastoviscous polymer—polyisobutylene, stress decayed in a log-like trend over 10 hours [114]. An empirical log decay function was given, without any theoretic explanation whatsoever. Also, Barnes and Roberts observed that when a human hair was fixed at certain strain, its stress showed a logarithmic decay with time [115]. The stress relaxation was attributed to deformation and relaxation of chemical bonds, polypeptide chains and non-crystalline regions. In addition, R. Weltmann reported that shear stress (not tensile stress but similar) in plastic material decayed logarithmically with time, and an empirical equation was deducted without theoretical elaborations [116]. In another report, Ramaswamy and Basak pointed out that in a stirred yogurt, shear stress also decayed logarithmically with time. Likewise, an

empirical equation was given which included constants that were dependent on the shear rate [117]. Additionally, S. Clarke *et al.* reported that in natural rubber, after initial seconds, normal stress (with strain fixed at 5%) showed linear decay with log-time [118]. It was described that "stress relaxation will continue to drop to zero if one waits long enough". The loss of elastic resistance was attributed to possible irreversible scission of polymer chains during straining. Thus, from extensive prior reports [119–121], it can be seen that a logarithmic decay of stress with time may prove to be possible, thereby validating our repeatedly confirmed experimental findings.

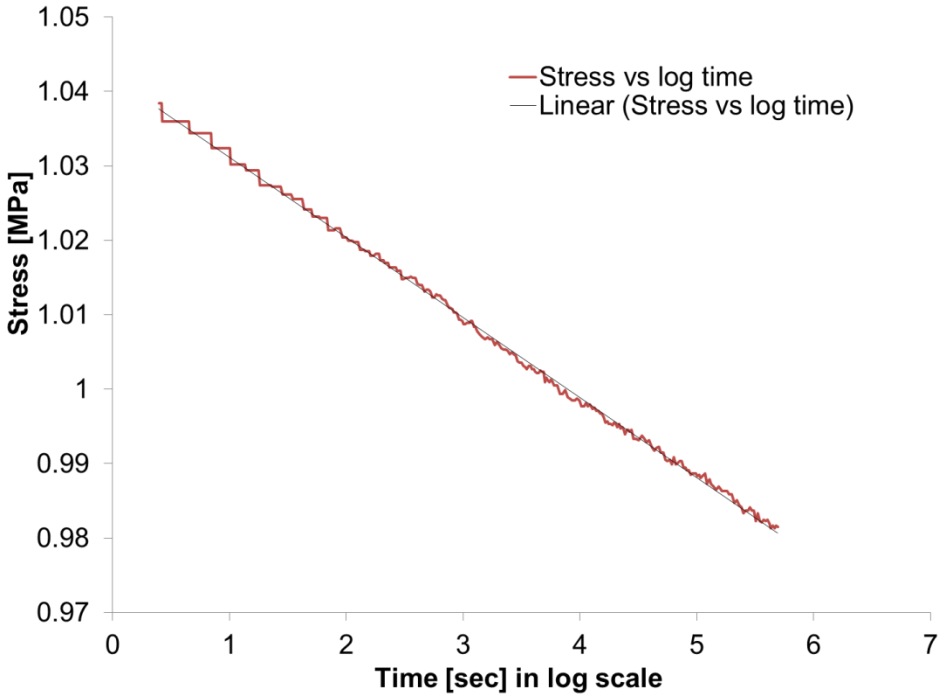

Figure 5.11 Linear trend of stress relaxation in a logarithmic time scale. The close matching of the stress relaxation curve with a linear fitting curve demonstrates the logarithmic decaying trend.

5.2.7 Comprehensive analysis of resistance, stress and strain of nanocomposite

Since the stress of nanocomposite materials may also impact its resistance in a similar way with strain, resistance was simultaneously recorded with stress during tests. In the cyclic testing of a bulk nanocomposite sample, a representative cycle of resistance change is shown in Figure 5.12, together with stress change. It should be pointed out that, the resistance profile of the bulk sample showed some level of measurement fluctuation over time (even under natural condition with no strain/stress), possibly due to irregular shifting of multiple current conduction paths existing in the bulk nanocomposite (with relatively large volume).

As shown in Figure 5.12, the overall pattern of resistance change for a bulk nanocomposite sample was much similar to that of a micropatterned nanocomposite sample (Figure 5.5). On the other hand, the pattern of stress change did not shown as complicated hysteresis aspects (for example, no initial decrease in stress). The loading section of the curve with relatively higher stress levels was clearly separated from the unloading section with relatively lower stress levels, indicating a varying Young's modulus. The difference with the two sections may be accounted by the stress relaxation occurring constantly inside the nanocomposite. During the unloading section, the decrease in stress was positively compounded by stress relaxation, which possibly led to a faster decrease in stress when strain level was high. In fact, throughout experiment, the pattern of stress change was observed to be typical of particle or nanomaterial filled polymers, according to previous report [122]. Further, over multiple cycles, stress change was found to be very consistent, as suggested in Figure 5.10.

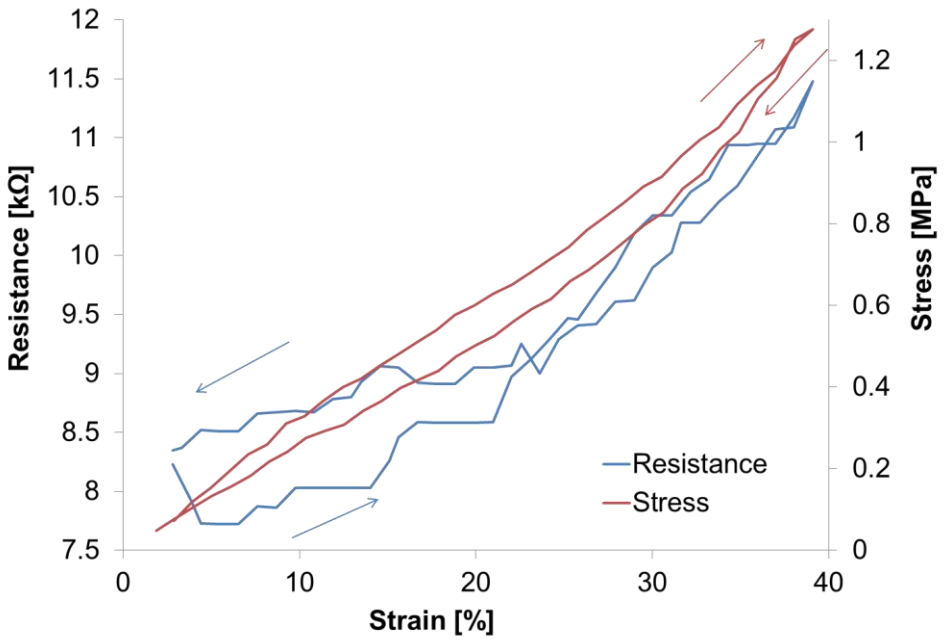

Figure 5.12 Resistance and stress changes during a loading and unloading cycle of strain. Arrows point to the direction of linear strain which was applied from 0 to 39% at a displacement rate of 0.2 mm/s

Moreover, the direct relationship of resistance and stress was also analyzed, as illustrated in Figure 5.13. Instead of a linear relationship, another non-linear relationship was revealed. Although both resistance and stress demonstrated logarithmic decays following a general empirical formula of $\delta = a - b \cdot \ln(t + c)$ as discussed previously, their constants a, b, and c were different. Thus, their relationship was not strictly linear. Experiments confirmed that resistance generally showed significantly faster decay with time in comparison to stress. Therefore, other factors, such as strain rate and strain history could also have impacted resistance and stress.

To gain a more thorough understanding of the polymeric mechanism inside the nanocomposite, the impact of strain rate was also investigated during experiments. Since only nanocomposite could contribute to any resistance change, micropatterned

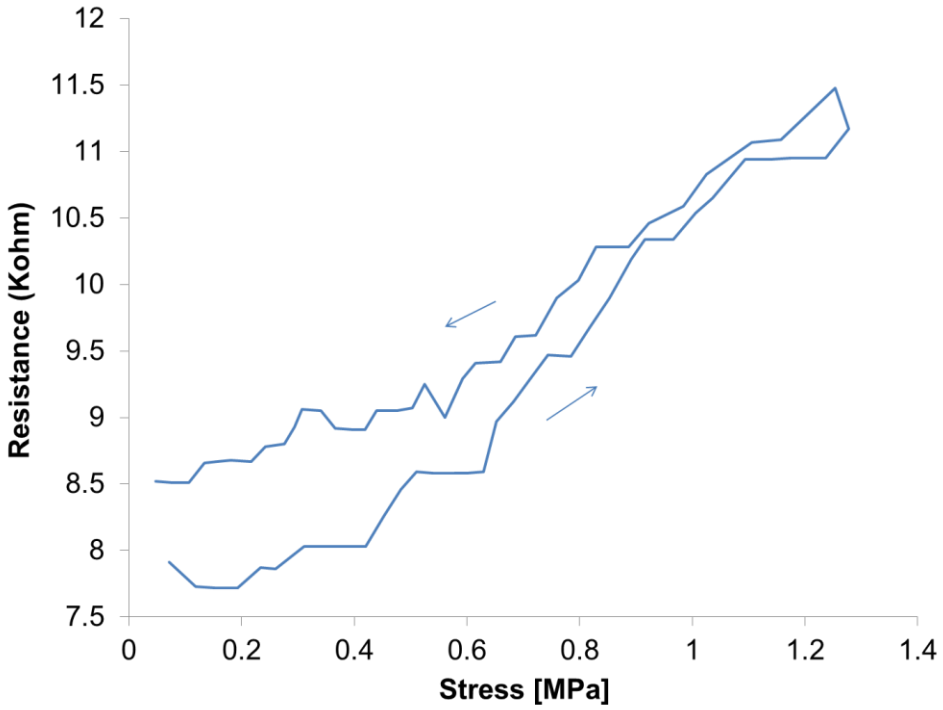

Figure 5.13 Resistance change plotted against stress. Data converted from Figure 5.12 above.

nanocomposite samples were used to record resistance, in order to provide more stabilized measurement results. Figure 5.14 illustrates a micropatterned strain sensor under tens of cycles of loading/unloading at four different strain rates. It can be seen clearly that resistance change was heavily impacted by the strain rate: higher the strain rate, more significant the resistance change. However, the magnitude of resistance was confirmed not to be linear with strain rate.

On the other hand, since both nanocomposite and pristine PDMS could contribute to stress change, bulk nanocomposite samples were used for stress testing. Figure 5.15 illustrates a representative curve of stress change under varying strain rates. In contrast to resistance which was impacted significantly by strain rate, stress did not reveal noticeable

impact by the strain rate. Rather, the magnitude of stress change stayed roughly constant regardless of strain rate. In Figure 5.15, it should be noted that the appearance of the first two cycles having comparatively lower maximum stresses may not be accurate, as the rheometer instrument only had limited sampling frequency topped at 1 Hz. Thus, the maximum stresses in the first two cycles may have not been recorded, could have been much higher.

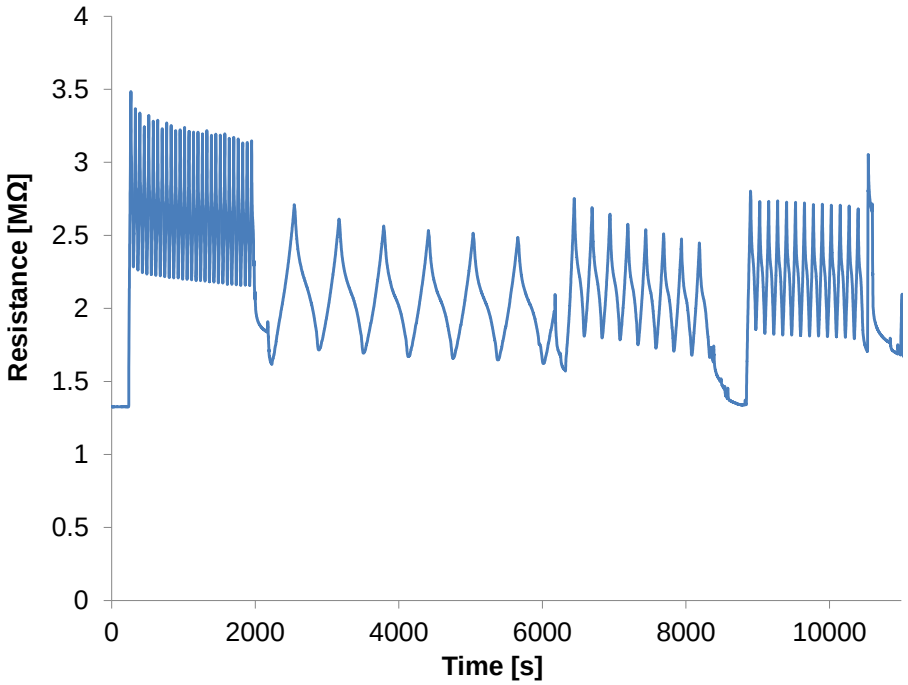

Figure 5.14 Resistance change of a micropatterned strain sensor under four distinct periods of cyclic loading and unloading. Each period has a different strain rate as follows: (first: 58.8 %/min; second: 5.9 %/min, third: 14.7 %/min, and fourth: 29.4 %/min).

Further, experiments using pristine PDMS samples also had similar results. As shown in Figure 5.16 (a) and (b), the Young's modules of a pristine bulk PDMS sample (9.1mm wide, 0.86 mm thick, and 35.9 mm long) only increased from 1.77 MPa to 1.85 MPa when its strain rate increased for over 83 times (from a displacement rate of 1.2

mm/minute to 100 mm/minute, which corresponds to a strain rate change of 3.34 %/min to 279 %/min).

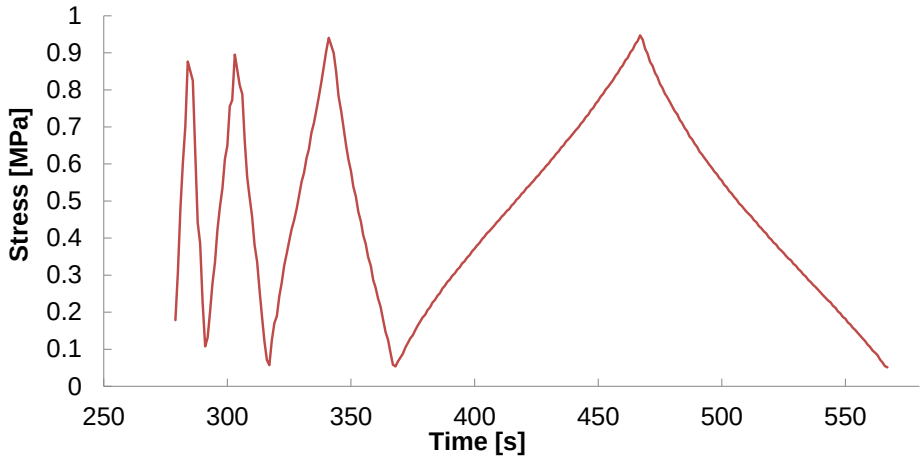

Figure 5.15 Stress change of a bulk nanocomposite sample under four different strain rates (displacement rate (μm/s) from left to right: 800, 400, 200, and 50). The magnitude of stress change remained roughly constant with varying strain rates.

While stress change did not seem to be impacted significantly by strain rate, previous literature reports [122–125] have well established the correlation between stress of polymers and strain rate. Thus, it may be possible that the stress of polymer materials comprises two parts: dynamic stress and static stress. Strain rate could be correlated with dynamic stress, while the strain level and strain time (or history) could be correlated with the static stress [121, 126]. In our tests, the frequency of loading and unloading may be relatively low, so that the dynamic stress component was not significant. Given a different testing system which could record stress change at a much higher frequency, the dynamic stress component may be accurately monitored, and therefore the correlation between dynamic stress and strain rate may be more thoroughly understood.

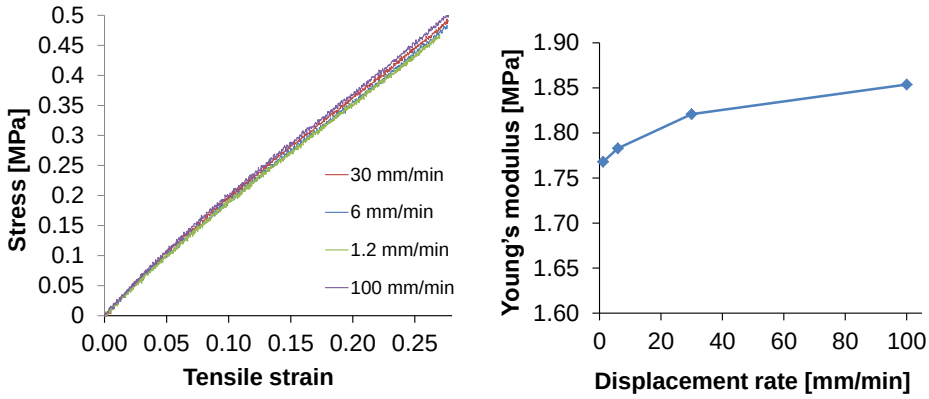

(a) (b)

Figure 5.16 Stress and Young's modulus change of a bulk pristine PDMS sample under four different displacement rates: (a) stress response of the PDMS sample under shown displacement rates; (b) Young's modulus at different displacement rates, which is converted from stress changes in (a).

5.2.8 Discussions

As outlined above in sections 5.2.6 and 5.2.7, although extensive experimental findings have been confirmed by prior studies and by us, it still remains a challenge to fully interpret the underlying micro-mechanics of a nanocomposite regarding its strain, strain rate, strain history, stress, and resistance. When an elastomer such as PDMS is filled with nano-scaled one-dimensional material such as carbon nanotubes, its material modeling could comprise several complicated elements including viscoelastic, thermoelastic, plastic and rubber elastic elements that may be interweaved with each other [127]. Thus, inside the extremely complex PDMS-MWCNTs nanocomposite, hysteresis of resistance change could have three sources which are PDMS, carbon nanotubes and its composite form. Current studies have only shed limited understanding into the complicated relationships between strain, stress and resistance, and further

theoretical investigation of the nanocomposite mechanisms may still be necessary for a complete understanding of the nanocomposite mechanisms.

Based on current understanding of the mechanisms of PDMS-MWCNTs nanocomposite, it may be added to the explanation given above that possible mechanisms of resistance and/or stress change under tensile strain may be accounted by several reasons or factors. The first one is the separation of carbon nanotubes networks and reduction of inter-tubular contact points. This change is mostly reversible at low strains. However, some separation and loss of contact points may be irreversible at high strains as well. The second reason is the resistance change caused by strained carbon nanotubes under stress. Their 3D geometries may be altered under strain and/or stress, leading to change in conductivity. This change may be reversible within tensile strength of carbon nanotubes. The third reason may be the scission of carbon nanotubes and/or breaking of carbon nanotube micro-aggregates (especially under high strains). Unlike the previous two factors, the scission process is irreversible. Moreover, when highly strained network chains are broken, it happens not instantly but over a period of time which contributes to the logarithmic stress relaxation and resistance decay. Also, when a nanocomposite is stretched to high strain and held there, initial stress relaxation or resistance decay is always most significant. After the initial period, subsequent relaxation or decay may not stop but may happen at a comparatively slower rate.

Overall, even though, at this point, the proposed PDMS-MWCNTs composite patterns may be premature for dynamic detection of random strains, this sensing scheme may still prove useful in certain applications. In the biomedical industry, for example, the ability to sense the biomechanical strain of certain heart muscles could be important for

diagnosis of some cardiovascular diseases. In this case, the biocompatible and flexible PDMS nanocomposite strain sensors could potentially be implanted and applied onto a muscle surface to provide long-term health monitoring. Should an abnormal condition occur in the otherwise regular strain profile of heart muscle, say strain amplitude decreases by half, the irregular resistive response could then be picked up by the sensor to help diagnosis.

5.3 Highly-sensitive pressure sensor prototype

5.3.1 Sensing principle

As discussed in Chapter 2, polymer nanocomposite micropatterns can be embedded into a thin polymer membrane and work as a diaphragm based pressure sensor. A simplified setup of a diaphragm-based pressure sensor in a differential configuration is illustrated in Figure 5.17. A thin PDMS film is bonded to another PDMS block which has a cavity in the center to create a diaphragm structure. Differential pressure across the two sides of the diaphragm leads to deflection of the flexible thin film. This dimensional deformation alters the resistance of the embedded nanocomposite.

With a very thin PDMS film and thin conductive patterns, even the slightest change in the differential pressure could induce a noticeable change in resistance. Thus, accurate pressure detection with ultra-high sensitivity can be readily obtained simply by measuring the resistance. In this work, to demonstrate the concept of sensitive pressure sensing, samples with various micropatterns were fabricated as selectively shown in Figure 5.18. At the current stage, however, an optimal design of sensing pattern has yet to be determined.

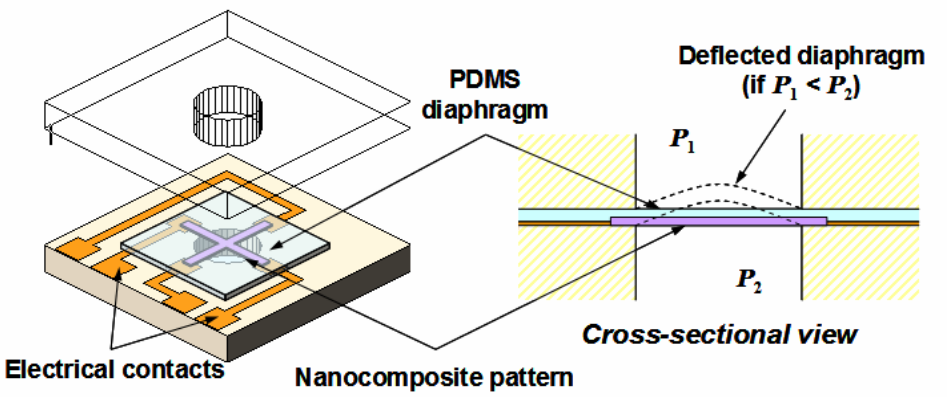

Figure 5.17 A schematic diagram showing a simplified configuration of a diaphragm-based differential pressure sensor.

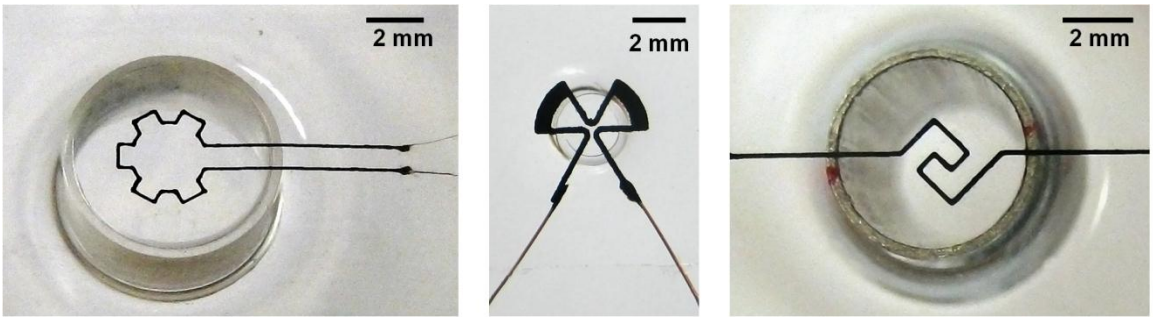

Figure 5.18 Fabricated pressure sensing devices with different microstructures embedded in PDMS diaphragm.

5.3.2 Experimental results

Since the sensitivity of pressure sensor relies on a thin PDMS diaphragm, its thickness needed to be controlled carefully. Unlike the fabrication of strain sensors where bulk PDMS could simply be poured on top of the nanocomposite patterns, here unmodified PDMS needed to be applied atop nanocomposite via a spin-coating process which had much better controllability of its thickness. Since the thickness of PDMS has been known to somewhat vary from batch to batch, our own characterization of thickness was necessary to obtain accurate control of thickness. Utilizing our spin coater (model:

WS-650SZ-6NPP/LITE, Laurell Technologies Corp., North Wales, PA), the relationship between the thickness of PDMS (10:1 standard ratio) and spin speed was tested, as illustrated in Figure 5.19. Thickness profile was found to be similar, though not identical (due to differences in factors such as curing temperature and time), with other literature reports [128-129].

Ideally, the thinner diaphragm is, higher the sensitivity would be. In practical situations, however, an excessively thin membrane could be difficult to be debonded from the substrate during fabrication. Moreover, the minimal thickness of the diaphragm should be thicker than the embedded nanocomposite, which also could not be too thin for conductivity considerations. In experimental tests, the membrane thickness generally varied from around 60 to 100 μm, since at this thickness sensitivity was relatively high while membrane could be de-bonded from the glass substrate.

Throughout our experiments, one side of the PDMS diaphragm was maintained at atmospheric pressure while the other side was connected via tube to an altering pressure source. Also, an ideal gas law was applied to use volume change to estimate the change of differential pressure, as no commercial product was found to be sensitive enough (< 10 Pa) for calibration purpose.

Before dynamic monitoring of differential pressure, the resistance stability needed to be ensured since a constant voltage source was used to provide a measuring current. In order to detect pressure at an ultra-high sensitivity, current measurement needed to be as accurate as possible, therefore any instability factor should be eliminated beforehand. V-I curves of a sensor at both natural state and deflected state were characterized, as shown in Figure 5.20, and stability of resistance was confirmed from the linear relationship

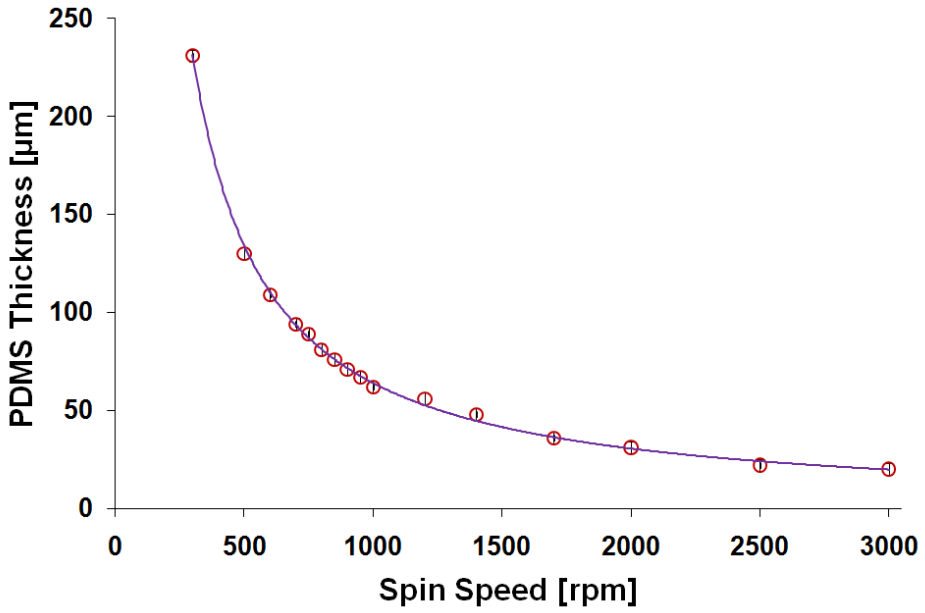

Figure 5.19 Relationship between thickness of PDMS (at standard 10:1 base: curing agent ratio) and spin speed. Spin-coating time is fixed at 60 seconds, with constant ramp rate of 200 rpm/second.

between DC voltage and current regardless of imposed pressure. The shown tested sample was fabricated using the laser assisted screen printing technique in the embedding approach. In tests, to minimize effects of time relaxation of resistance, which was similar to time relaxation of strain sensors described above, V-I values were measured after resistance largely settled.

In addition, to better understand the mechanical behavior of the diaphragm, the deflection of a pressure sensor (3.3 mm in diaphragm diameter and 62 µm in thickness) was recorded while it was exposed to pressure change as shown in Figure 5.21. As high as 1.3 mm of linear deflection (equivalent to 40% of diameter) was observed under less than 50 kPa of pressure difference—a clear indication of the remarkable mechanical

flexibility of the PDMS diaphragm, which makes it possible for diaphragm to detect extremely small change of pressure.

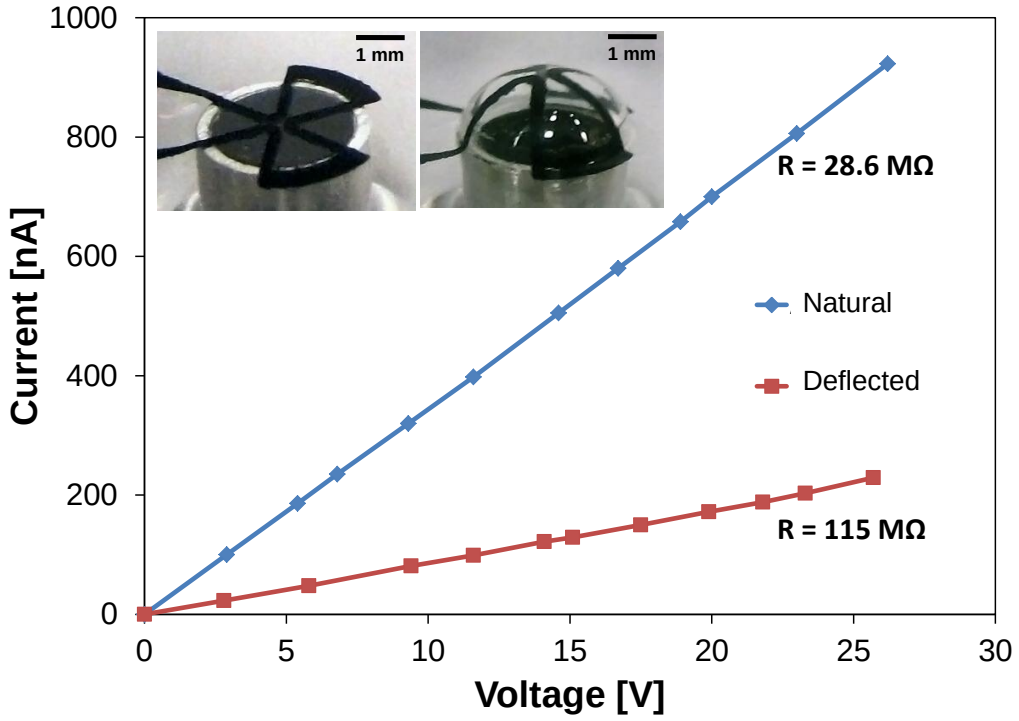

Figure 5.20 V-I curves of a pressure sensor under natural and deflected state showing a linear relationship between voltage and current. Inset shows tested sample in the natural and deflected state. The sample has diaphragm diameter of around 3.3 mm and thickness 62 μm, and embedded nanocomposite contained about 7.8 wt% MWCNTs and had thickness of around 43 μm.

An important novelty of the pressure sensor developed here was to provide accurate monitoring of pressure change across the diaphragm. Figure 5.22 shows the sensitivity of the sensor device (8 mm in diaphragm diameter and 43 μm in thickness) in a best case scenario. With just about 3 kPa of pressure change across the diaphragm, the resistance of the nanocomposite increased for more than 4.8 times. At the upper portion of the curve, as zoomed in the inset, pressure change less than 100 Pa could produce a noticeable

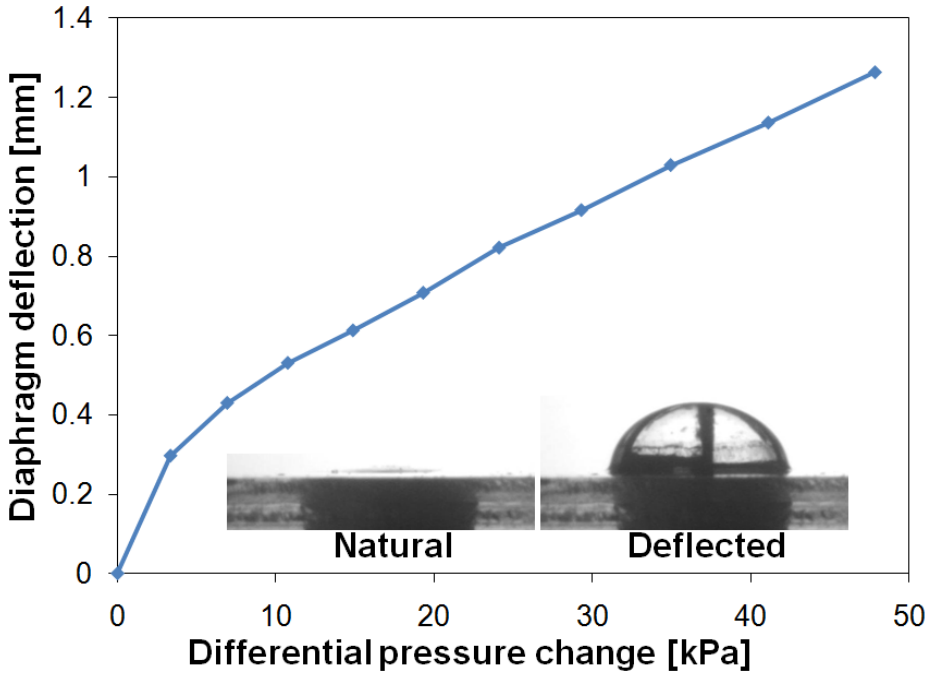

Figure 5.21 Diaphragm deflection under varying differential pressure of a tested sample (same sample with Figure 5.20).

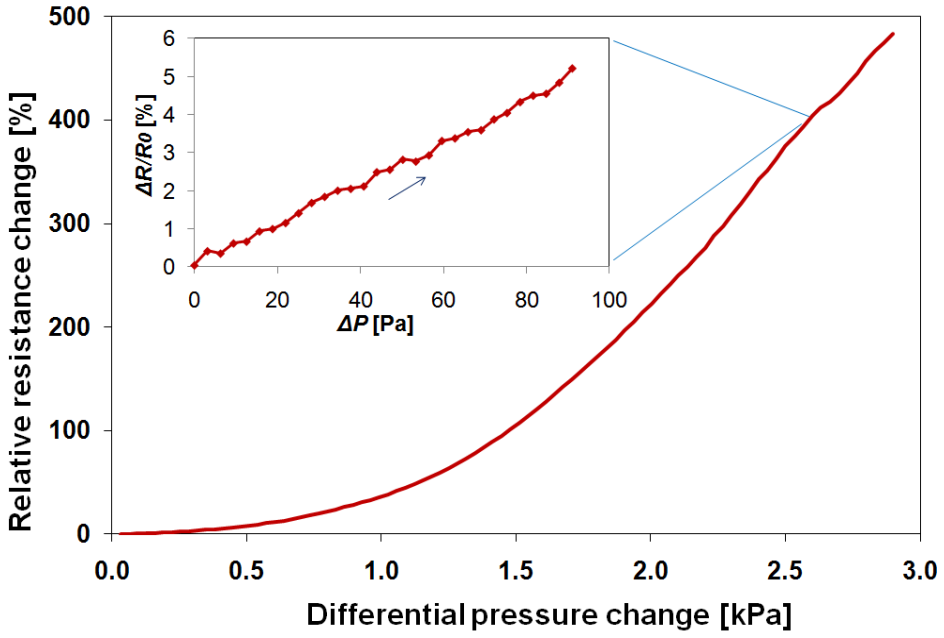

Figure 5.22 Resistance change under differential pressure of 0-2.9 kPa. Inset: minimal pressure change was ~ 3 Pa between adjacent data points. Base resistance R_0 used here was different from overall base resistance.

resistive change. This sensitivity surpassed some previous reported similar works [63–67, 130], which was a significant improvement. However, it should be noted that, at this stage, the resistive response of nanocomposite under differential pressure is not linear over the entire sensing range. When pressure change was above ~1.5 kPa, resistive response was somewhat linear with sensitivity of 288% per kPa. When pressure change was reversed, certain hysteresis effect was still observed similar to the hysteresis phenomena of strain sensors that were discussed above.

5.3.3 Parameter studies

The resistance change of diaphragm-based pressure sensors depended on a variety of configurative parameters, such as diaphragm diameter, thickness, nanocomposite geometry, and so forth. Hence, to gain a better understanding of the characteristics of pressure sensors, some of the parameters were studied in this work. For example, multiple pressure sensors with different diameters were fabricated using laser ablation and micropatterning of relief structures. A representative device is shown in Figure 5.23. This integrated sensing format included two diaphragms with the same thickness but different diameters. A common air channel was connected to both diaphragms as a pressure inlet and outlet. For testing purposes, a sensing pattern of two straight lines were patterned in the radial direction of diaphragms using the aforementioned laser assisted fabrication in the relief patterning approach. An electrode was patterned between the two diaphragms, so that the resistance of each diaphragms could be monitored individually from only one side of the diaphragm.

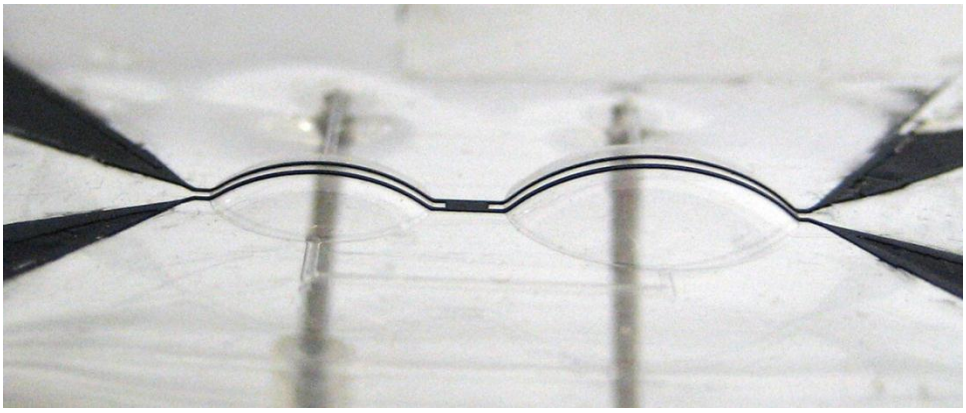

Figure 5.23 An image showing two integrated pressure sensor diaphragms with diameters of 7.8 mm (right) and 5.9 mm (left) deflected under identical differential pressure. Thickness of the two diaphragms was about 50 μm. Width of the nanocomposite relief patterns (containing around 7.8 wt% MWCNTs) was about 200 μm and thickness of the nanocomposite about 58 μm.

The two integrated pressure sensors were connected to a varying pressure source which was realized through a syringe pump (Harvard Apparatus PHD2000) and a length of plastic tubes. During testing, the total volume connected to the pressure sensors was changed, which was then converted to a pressure change following the ideal gas law. Resistance change was recorded simultaneously using a multimeter with the pressure change. Multiple cycles of increasing and decreasing pressures were tested, with some representative results shown in Figure 5.24. It can be seen clearly that the larger diaphragm demonstrated relatively more significant resistive response to a cyclic pressure change of 0 to about 2.8 kPa under atmospheric conditions. Also, hysteresis effects similar to that of strain sensors were observed.

Since the two diaphragms had different base resistances, it was difficult to directly compare the relative sensitivity of the two pressure sensors. Thus, for a more objective comparison, relative resistance changes (instead of absolute changes) were plotted, as

shown in Figure 5.25. Comparison suggested that after converting to a relative scale, the larger diaphragm clearly showed a more significant resistance change in response to an identical pressure change. Further, over the six cycles of pressure changes shown, the magnitudes of resistance change in percentage were calculated, as shown in Table 5.1. Comparison results indicated that the pressure sensor with larger diaphragm was about 1.4 times more sensitive than the pressure sensor with smaller diaphragm. Interestingly, despite the variation in the scale of resistance change for each cycle, the sensitivity ratio between the two diaphragms stayed roughly constant.

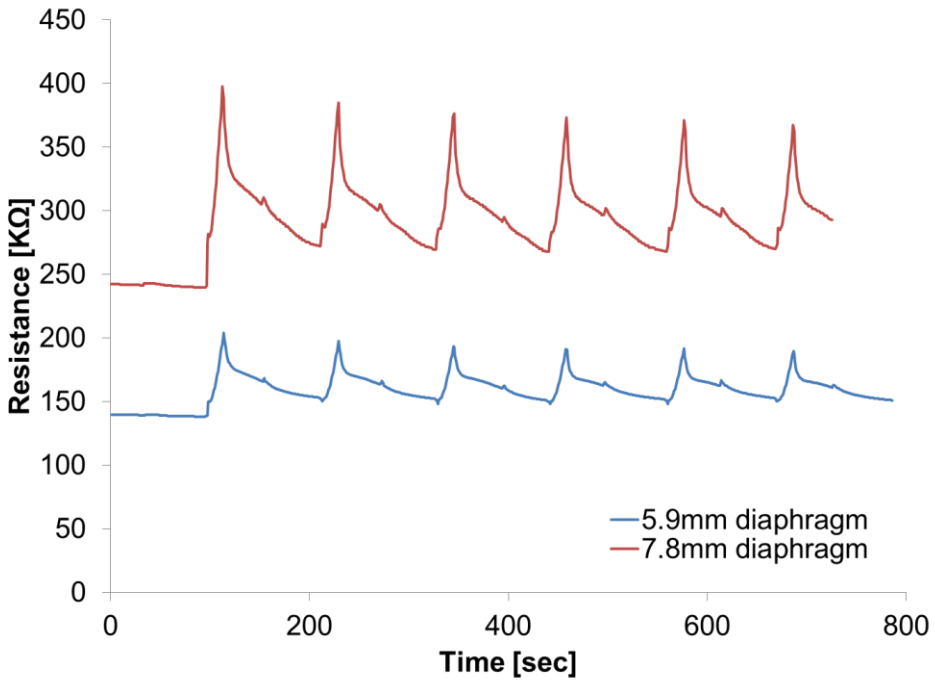

Figure 5.24 Resistance changes of pressure sensors with two different diaphragm diameters. The pressure sensor with larger diaphragm had higher resistance, but also had more significant response to pressure change from about 0 to 2.8 kPa under atmospheric conditions.

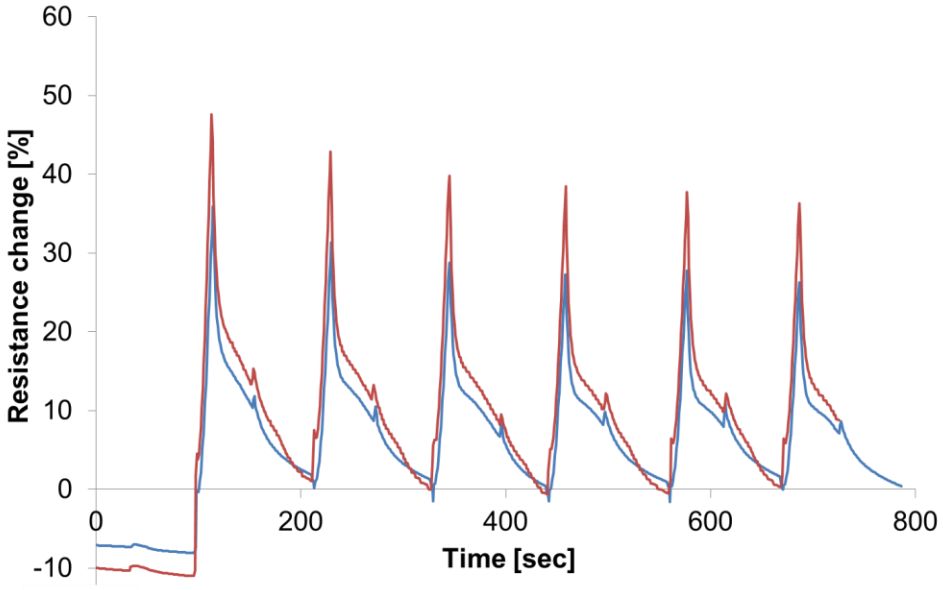

Figure 5.25 Relative resistance changes of pressure sensors with two different diameters. For a more consistent comparison, the base resistance for each diaphragm was selected to be the recovered resistance after each pressure cycle, rather than the initial resistance.

Table 5.1 Examples of strain sensors made from different polymer matrices and their respective performances. $\Delta R_1/R_1$ (%) indicates relative resistance change of the 7.8 mm sample, while $\Delta R_2/R_2$ (%)indicates relative resistance change of the 5.9 mm sample.

Diameter	7.8 mm	5.9 mm	Sensitivity ratio between two diameters
Cycle number	$\Delta R_1/R_1$ (%)	$\Delta R_2/R_2$ (%)	
1	47.6	35.89	1.33
2	42.89	31.36	1.37
3	39.81	28.81	1.38
4	38.51	27.26	1.41
5	37.76	27.75	1.36
6	36.35	26.25	1.38

From testing results shown above, it may be concluded that, when other parameters or conditions were similar, a larger diameter of diaphragm may lead to more sensitive response of the pressure sensor. However, there might be a tradeoff in the design of

pressure sensors regarding diaphragm diameter. On one hand, a smaller diameter would lead to an overall smaller pressure sensor and more miniaturized system which might be advantageous. On the other hand, the smaller diameter may cause a decrease in the sensitivity of the sensor's response to external pressure change. Thus, an appropriate balance between size and performance may be selected. According to experimental findings of this dissertation, diameters between 4-8 mm may prove most sensible for various purposes.

5.3.4 Discussion

As discussed above, hysteresis effects were consistently found in pressure sensors which resembled that of strain sensors. Even with deeper understanding of the nanocomposite hysteresis effect, it would be a difficult task to completely eliminate or overcome it, as the resistive response of sensor devices is a complicated combination of multiple factors such as strain level, strain rate, time, stress etc. However, practical engineering approaches may still be attempted to decrease or minimize the impact of the hysteresis effect. Although limitations may be tied to the pressure sensor in terms of its application, its practical usefulness may still be boosted.

For practical sensor applications certain hysteresis effect could be circumvented or minimized to a certain extent by appropriate system designs. In the case of pressure sensor, during experiments, instead of directing connecting the sensing diaphragm to a varying pressure source, certain valves were introduced within the tubing, as illustrated in Figure 5.26. By opening/closing valves A and B alternatively in a controlled fashion, the sensor diaphragm was reset to its natural state (by exposing it to atmospheric pressure)

after each time of discrete resistance measurement (by exposing diaphragm to pressure source).

Briefly, in tests, valve A was first closed and valve B open before every measurement. Thus, pressure sensor would be under its natural condition. Then, when a pre-defined measurement time interval is met, valve B was closed and valve A opened immediately. Suddenly, the pressure sensor was exposed to the pressure source, leading to a significant and fast spike in its resistance. The maximum resistance level was manually recorded. Then, after a few seconds, valve A was closed again and valve B opened, resetting the pressure sensor again to atmospheric level. Meanwhile, the pressure source may be varied for next measurement. Next, after a fixed time interval which was the frequency of pressure measurement, the whole process was repeated. Now since each measurement is a result of the same procedure except the pressure difference in the pressure source, the polymeric hysteresis effect was found to have significantly reduced.

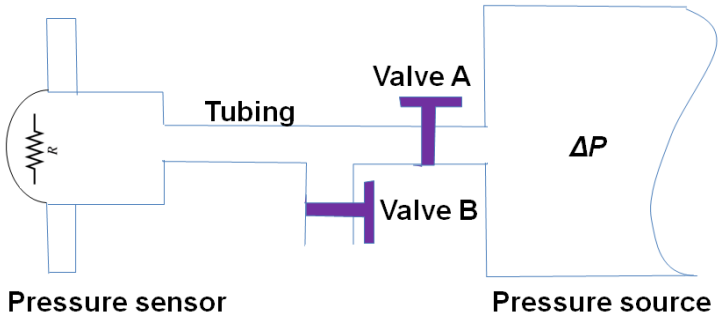

Figure 5.26 A schematic diagram showing a testing setup of a pressure sensor which could potentially minimize the hysteresis effect caused by the polymer nanocomposite.

During experiments, since the resistance spike occurred extremely quickly (usually in less than a tenth of a second), fast sampling was required to record this resistance change which was realized via a picoameter. As the data communication between the picoameter

and a current-recording device (i.e., a computer connected via RS-232) could not meet the requirement of sampling frequency, a camcorder was utilized instead to record the resistance change on the display of the picoameter. Later, the recorded video was manually decoded frame-by-frame, generating individual images, such as the one shown in Figure 5.27. Then, each frame was manually read, and the maximum level of the resistance spike was recorded. Although this manual process proved to be quite cumbersome, for practical applications, the sampling process may be automated by improved equipment.

Figure 5.27 A screenshot of a picoameter measurement extracted from a camcorder. During tests, a large amount of screenshots were read manually, and the minimum level or current (corresponding to maximum resistance spike) was recorded.

Pressure sensors were tested using the procedure outlined above and results were extracted from videos. Figure 5.28 shows a representative testing result of a pressure sensor which had a single diaphragm of about 5.7 mm in diameter and about 70 μm in thickness. The pressure sensor was exposed to about 0 to 13 kPa of positive pressure changes with an atmospheric baseline. The interval of each measurement was set to be 5 minute. Results clearly suggested that the typical pattern of hysteresis in resistance change curves was significantly reduced. In fact, even randomly adjusted pressure in the

pressure source was detected during testing, which closely matched with the overall curve of resistance change.

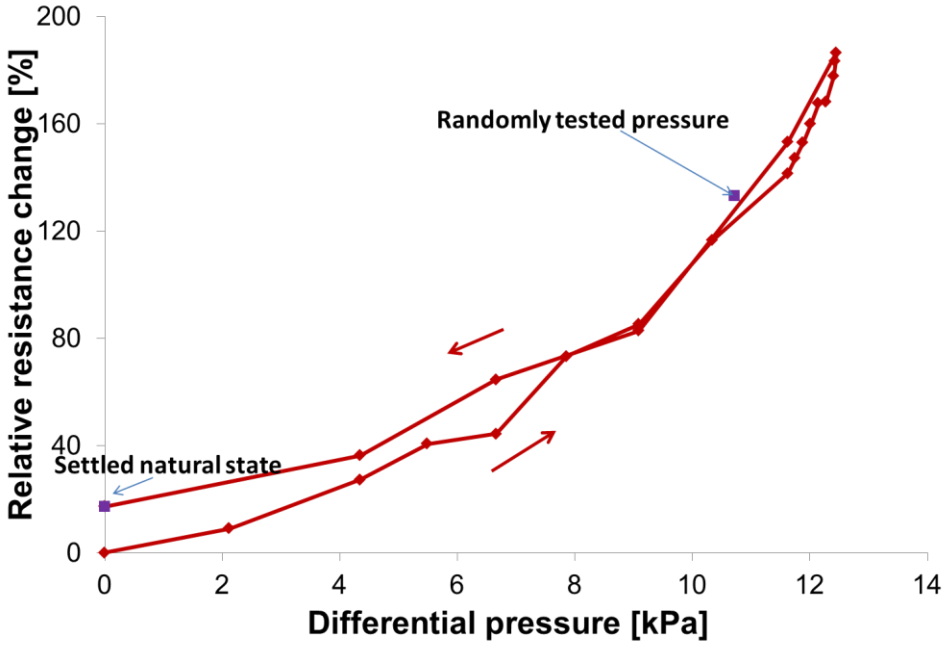

Figure 5.28 Resistance change of a pressure sensor which was measured discretely at every 5 minutes. Compared with continuous measurements, this discrete result suggested a reduced hysteresis effect and more consistent response.

It should be understood that even though the discrete measurement and resetting of pressure sensor may help reduce its hysteresis effect, some limitations of applications were created consequently. For example, since measurement could only be made at a low frequency, it may not be suitable for continuous monitoring of pressure change. Also, since the alternative opening of valve A and valve B would vary the pressure of its measured source, the pressure source would be limited to have significantly larger volume than the tubing connections (e.g., a warehouse, a large container, etc.). Overall, the approach described above may serve as an example of designing applications to minimize hysteresis effect. Although this type of system would impose limitations on the

application area, it may still allow the developed sensor devices to be useful in practical situations before a full understanding of polymer mechanics can be obtained.

5.4 Summary

In this chapter, to demonstrate the feasibility of its sensing applications, prototypes of strain sensors and pressure sensors were manufactured and tested extensively to evaluate their sensing performances.

Fabricated strain sensors revealed significant resistance changes under large range tensile strains over 45%. Resistive response was characterized under both single rising strain and multiple cycles of loading/unloading tensile strain. Some peculiar hysteresis effects of resistance response were observed during the course of characterization, which could relate closely to internal stresses within the polymer nanocomposite. Thus, in order to reveal underlying polymeric mechanisms, stress and resistance of bulk polymer nanocomposite samples were tested under various conditions, such as different fixed strain levels, different strain rates, different strain history (or time). During extensive experiments, an interesting temporal pattern of logarithmic decay was repeated found in stress and resistances, which could be related to a process of stress relaxation within the nanocomposite. As a result, the resistance was found to be dependent on a number of factors such as stress, strain rate and strain history or time. Likewise, stress was also found to be possibly dependent on the same variables. A number of variables were found to be interweaved with one another, indicating the extreme complexity of the polymeric mechanism of the nanocomposite, which involved multiple components including macro-chained polymer, nano-fillller and their interfaces.

Furthermore, fabricated diaphragm-based pressure sensor prototypes also revealed promising potential as a highly-sensitive sensing format for monitoring of differential pressures. Certain aspects of the fabrication process which were specifically important to pressure sensors were discussed in detail. In experimental tests of pressure sensors, parameters such as electrical resistance and mechanical deformation were recorded and characterized. Under a varying differential pressure across the diaphragm at the atmospheric level, sensor devices were found to have capability of detecting minute pressure changes—on the level of 100 Pa or less, which indicated a significant improvement over previously reported similar sensing protocols. Further, parameters such as diameter of diaphragm were studied, and their impact on the sensing sensitivity was discussed. In practice, there may be a tradeoff between different parameters such as sensitivity and size of pressure sensors. Additionally, hysteresis effects were observed to be similar with that of strain sensors. To enable the application of pressure sensor under certain restricted applications, a configuration of sensing system was discussed to reduce the effect of hysteresis on the resistance response.

CHAPTER 6: CONCLUSIONS AND FUTURE WORK

6.1 Conclusions

6.1.1 Dispersion of CNTs in polymer nanocomposite

A uniform distribution of carbon nanotubes throughout the polymer matrix is critical to ensure the consistency of electrical and mechanical properties of polymer nanocomposites. Especially for patterned microstructures, the requirement for dispersion quality is even high than bulk material. As an effort to reach optimal dispersion quality, in this dissertation, a common solvent was selected amongst various extensively tested organic solutions to assist the dispersion of MWCNTs inside PDMS matrix. Based on its high solubility for PDMS and MWCNTs respectively, and its ability to retain dispersed state of MWCNTs in presence of PDMS, chloroform was found to be an optimal choice as a common solvent. Also, the surface functionalization of CNTs by carboxyl groups was found to be beneficial for further improvement of dispersion quality.

Through extensive testing of a variety of widely used physical dispersion techniques such as shear mixing, mechanical stirring and sonication, a combinatory approach was developed in which mechanical stirring was used to facilitate the initial dissolution of PDMS inside common solvent, and mild sonication used to as a main tool to disperse MWCNTs within PDMS. Following the dispersion stage of MWCNTs and PDMS within the common solvent, the process of evaporating the common solvent was also critical to minimize the effect of CNT reaggregation. In this dissertation, the evaporation process was facilitated and expedited by use of vacuum pump and accurate control of elevated

temperatures. Solution drying time was significantly shortened, and thereby initial dispersion quality was largely retained throughout solvent evaporation.

Even at high loading concentrations of CNTs within polymer, high quality dispersion of nanocomposite was achieved, which showed significant improvement over prior approaches. Dispersion quality was studied using various characterization tools such as optical microscopy and electron microscopy. Furthermore, important electrical properties were characterized in detail. Electrical conductivity of nanocomposite was found to be suitable for use as short-range electrodes or more importantly as piezoresistive sensing elements. In addition, temperature dependence of electrical properties was measured to be minimal, which was also a desirable attribute for sensor applications.

6.1.2 Micropatterning techniques

Microfabrication of polymer nanocomposite is essential for its purpose as practical sensor elements in MEMS applications. In order to overcome technical issues in existing patterning techniques which relied on photolithography and wet chemical processes, several novel fabrication protocols, namely microcontact printing, laser ablation assisted embedding, and laser ablation assisted relief-patterning, were developed in this dissertation to improve micropatterning of conductive nanocomposite.

The process of microcontact printing was introduced in detail, from the manufacturing of printing mold, to transferring of patterning through direct printing and to casting molding of PDMS to embed nanocomposite patterns inside all-elastomer devices. Characterization of patterning quality in terms of its resolution, uniformity and reliability was carried out, revealing microcontact printing to be a reliable protocol of microfabrication. Due to its ability to repeatedly use the pre-manufactured printing mold

and direct transfer of patterns in a matter of minutes, microcontact printing avoids the repetition of the lithography process for each sample, thereby significantly simplifying the fabrication process which saves both time and cost.

Laser ablation assisted approaches, as improved alternatives in comparison to microcontact printing, were also introduced. From the optimization of ablation conditions, to the selection of optimal screen film material and to the filling/removing of nanocomposite, the complete process flows of fabrication were discussed in detail. Two variations of protocols were introduced, wherein the first protocol embedded micropatterns of polymer nanocomposite into the bulk polymer, and wherein the second protocol realized relief-patterns of polymer nanocomposite on the surface of the bulk polymer. Depending on application, both approaches hold their respective pros and cons, where were discussed in detail. For both protocols, the patterning performances were characterized in terms of resolution and uniformity. In laser ablation assisted micropatterning approaches, since new designs of sensor patterns could be readily implemented by merely a CAD software rather than a more complex lithography or stamp-fabrication process, it offers an ideal protocol for lab prototyping work where usually a large amount of various sensor devices need to be tested.

Overall, the microfabrication techniques developed in this dissertation demonstrated distinctive advantages over previous patterning methods. Although limitations are still present with room to improve, these novel techniques provide promising approaches for the microfabrication of polymer nanocomposite for a wide variety of applications.

6.1.3 Sensor prototypes using piezoresistive nanocomposite

Thanks to distinctive properties such as mechanical flexibility and electrical piezoresistivity, PDMS-MWCNTs composite as a sensor material offers a wide range of potential applications. Therefore, to demonstrate the feasibility of its sensing applications, prototypes of strain sensors and pressure sensors were manufactured and tested extensively to evaluate their sensing performances.

The fabricated strain sensor revealed significant resistance change under large range tensile strain of over 45% --a range much higher than commercially available products or other polymer based strain sensors. Its sensing factor was found to be in the neighborhood of two, which was comparable to some commercialized products. Resistive response was characterized under both single rising strain and multiple cycles of loading/unloading tensile strain. Some peculiar hysteresis effects of resistance response were observed during the course of characterization, which could relate closely to internal stresses within the polymer nanocomposite. Thus, in order to reveal underlying polymeric mechanisms, stress and resistance of bulk polymer nanocomposite samples were tested under various conditions, such as different fixed strain levels, different strain rates, different strain history (or time). During extensive experiments, an interesting temporal pattern of logarithmic decay was repeated found in stress and resistances, which could be related to a process of stress relaxation within the nanocomposite. As a result, the resistance was found to be dependent on a number of factors such as stress, strain rate and strain history or time. Likewise, stress was also found to be possibly dependent on the same variables. A number of variables were found to be interweaved with one another, indicating the extreme complexity of the polymeric mechanism of the nanocomposite,

which involved multiple components including macro-chained polymer, nano-fillller and their interfaces. Although still yet to attain a thorough understanding of the micro-scaled mechanics, potential mechanisms responsible for resistance and stress changes were discussed.

On the other hand, the fabricated diaphragm-based pressure sensor prototype also revealed promising potential as a highly-sensitive sensing format for monitoring of differential pressures. Certain aspects of the fabrication process which were specifically important to pressure sensors were discussed in detail. In experimental tests of pressure sensors, parameters such as electrical resistance and mechanical deformation were recorded and characterized. Under a varying differential pressure across the diaphragm at the atmospheric level, sensor devices were found to have capability of detecting minute pressure changes—on the level of 100 Pa or less, which indicated a significant improvement over previously reported similar sensing protocols. Further, parameters such as diameter of diaphragm were studied, and their impact on the sensing sensitivity was discussed. In practice, there may be a tradeoff between different parameters such as sensitivity and size of pressure sensors. Additionally, hysteresis effects were observed to be similar with that of strain sensors. To enable the application of pressure sensor under certain restricted applications, a configuration of sensing system was discussed to reduce the effect of hysteresis on the resistance response.

6.2 Future work

6.2.1 Numerical modeling of polymer nanocomposite

As intriguing as the sensor prototypes were in their sensing feasibility, the mechanics of the polymer nanocomposite was not thoroughly understood in this dissertation. Consequently, the hysteresis effects intrinsic of polymer nanocomposites could not be fully overcome. From the perspective of long-term application, this will limit the feasibility of polymer nanocomposite as a practical sensor element. Further, complete understanding of the polymeric mechanisms would be difficult to achieve through mere experimentation, due to the complexity of its structural nature. Intrinsically, micro or nano-scaled structures of polymer molecules and nanofillers may determine large-scale behaviors of the polymer nanocomposite. Thus, the micro-mechanisms of the material may be explored by numerical modeling of polymer nanocomposite.

For example, numerical modeling may establish structural models of polymer molecules as well as carbon nanotubes. Specific pertinent mechanical and electrical properties may be attributed to these structural models. More importantly, interactions of various components within the nanocomposite may be thoroughly studied. After established of numerical models, the overall large-sclae behavior of the nanocomposite may be simulated using finite element analysis (FEA). This study may prove to be a non-trivial task, since various complex interactions may need to be considered including, for instance, interactions between polymer molecules and other polymer molecules, between carbon nanotubes and other carbon nanotubes, and between polymer molecules and carbon nanotubes. Both polymer molecules and carbon nanotubes may have complex three-dimensional structures, and may heavily entangle with other structures. Further,

strain and/or stress changes induced on the nanocomposite may alter structures of all components in various ways, some of which may be irreversible and others reversible. Despite the complexity of the nanocomposite, the numerical modeling of this material could help overcoming its hysteresis effects for improved usage as sensing elements.

6.2.2 Continued development of current sensors

In this dissertation, much effort has been invested in the optimization of the dispersion of carbon nanotubes within polymers, as well as micropatterning of high quality nanocomposite structures. Thus far, although sensors have been shown to respond significantly to external stimulus (strain, pressure), their consistency in response still needs to be improved. Thus, continued optimization and improvement of the device fabrication process may be needed to realize sensor devices with more consistent properties. For example, manual processes, such as filling/removing of nanocomposite inside micro-molds and peeling of PET films, may be automated so that more microfabrication reliability may be further improved. Also, improved testing platforms such as pressure sources may be incorporated so that the resistive responses of sensor devices under stimulus would be more repeatable across a larger number of devices.

Further studies of additional parameters of sensor devices such as geometry of micropattern design may be achieved via experiment and simulation, so that their influence on the sensing performance may be characterized and optimal designs of sensors may be determined. For example, thickness of nanocomposite patterns is another important parameter in determining the sensitivity of diaphragm-based pressure sensors. Although a thinner diaphragm with thinner nanocomposite could lead to higher sensitivity, the overall resistance could increase. Also, with a thinner composite,

dispersion quality could become more critical, as any bundle or void could have a higher chance of blocking current conduction in the nanocomposite. Thus, considering the trade-off, it is important to determine an optimal thickness of diaphragm and nanocomposite patterns.

In addition, more numbers of sensor elements may be incorporated on-chip in differential configurations to increase the sensing performance and reduce hysteresis effects. Other aspects, such as contact resistance between carbon nanotubes and metal electrode at two ends of nanocomposite samples (although relatively insignificant compared to the overall sensor resistance) may be further investigated systematically and quantitatively. It seems possible that, if contact is made prior to PDMS curing, metal surfaces and carbon nanotubes in PDMS reach maximum interface area during the curing process, which leads to a minimized contact resistance between metal and carbon nanotubes.

Before sensors can be used in practical applications, other factors need to be tested in fabrication and operations of the sensors. These factors could include, for example, humidity, which could affect the mechanical properties of the PDMS and nanocomposite. Although the impact of humidity may be non-existent or limited, since PDMS and its nanocomposite are hydrophobic materials [131], this aspects are worth investigating in order to realize robust working sensors that fit various environments.

6.2.3 Development of other sensor formats

Potential applications of PDMS-MWCNTs nanocomposite are by no means limited to strain and pressure sensors. In fact, a variety of additional sensor formats could potentially be developed based on the same basic principle discussed in this dissertation.

For example, the developed air pressure sensor may also work in a liquid environment. Since the essential principle of pressure sensor is to detect pressure difference between two sides of a diaphragm, it could be potentially used in a microfluidic system to measure the pressure drop over a certain channel length. Then, this would allow the detection of flow rate inside microfluidic channel, as the pressure drop and flow rate are closely associated. Due to the chemical inertness of PDMS and CNTs, except for organic solvents which could dissolve solidified PDMS, its contact media could be quite diverse. Accurate measurement of flow rates could prove valuable in various lab-on-a-chip systems.

For another example, localized pressure sensors—or in other words—pressure mapping devices, which allow detection of local pressure on multiple points on a certain area, could also be potentially developed using the techniques developed in this dissertation. Potentially, by overlaying in orthogonal directions two layers of conductive nanocomposite patterns which are insulated by a thin layer of elastomer, a grid of nanocomposite may be formed. Local resistance or capacitance change induced by external pressure/stress inserted on certain points of the layer could be pin-pointed, thereby allowing device to work as a tactile sensor.

6.2.4 Exploration of non-sensor applications

Finally, as an extremely versatile material, polymer nanocomposite is not limited to only function as a sensing element. Aside from sensor applications, polymer nanocomposite still may serve as an attractive material because of its unique properties (e.g., conductivity, light weight, tensile strength, infrared absorption, etc.). In fact, it may serve as a promising material for many other applications, such as protective coating film,

electromagnetic shielding layer, mechanical enhancing ingredient, and so forth. Upon proper development and understanding, polymer nanocomposites may yield promising potential for these applications.

REFERENCES

[1] R. Bogue, "MEMS Sensors: Past, Present and Future," *Sensor Review*, vol. 27, no. 1, pp. 7–13, 2007.

[2] C. S. Smith, "Piezoresistance Effect in Germanium and Silicon," *Phys. Rev.*, vol. 94, no. 1, pp. 42–49, Apr. 1954.

[3] W. Paul and G. L. Pearson, "Pressure Dependence of the Resistivity of Silicon," *Phys. Rev.*, vol. 98, no. 6, pp. 1755–1757, Jun. 1955.

[4] W. G. Pfann and R. N. Thurston, "Semiconducting Stress Transducers Utilizing the Transverse and Shear Piezoresistance Effects," *J. Appl. Phys.*, vol. 32, no. 10, pp. 2008–2019, Oct. 1961.

[5] O. N. Tufte, P. W. Chapman, and D. Long, "Silicon Diffused-Element Piezoresistive Diaphragms," *J. Appl. Phys.*, vol. 33, no. 11, pp. 3322 – 3327, Nov. 1962.

[6] T. H. Marwick, "Measurement of Strain and Strain Rate by Echocardiography," *J. Am. Coll. Cardiol.*, vol. 47, no. 7, pp. 1313–1327, Apr. 2006.

[7] A. Khosla and B. L. Gray, "Preparation, Micro-Patterning and Electrical Characterization of Functionalized Carbon-Nanotube Polydimethylsiloxane Nanocomposite Polymer," *Macromol. Symp.*, vol. 297, no. 1, pp. 210–218, Nov. 2010.

[8] X. Z. Niu, S. L. Peng, L. Y. Liu, W. J. Wen, and P. Sheng, "Characterizing and Patterning of PDMS-Based Conducting Composites," *Adv. Mater.*, vol. 19, no. 18, pp. 2682–2686, Sep. 2007.

[9] J. Engel, J. Chen, N. Chen, S. Pandya, and C. Liu, "Multi-Walled Carbon Nanotube Filled Conductive Elastomers: Materials and Application to Micro Transducers," in *Proceedings of the 19th IEEE International Conference on Micro Electro Mechanical Systems*, Istanbul, Turkey, 2006, pp. 246–249.

[10] V. T. S. Wong, A. Huang, and C.-M. Ho, "SU-8 Lift-Off Patterned Silicone Chemical Vapor Sensor Arrays," in *18th IEEE International Conference on Micro Electro Mechanical Systems*, Miami Beach, FL, 2005, pp. 754–757.

[11] T. Pan and H. Cong, "Photopatternable Conductive PDMS Materials for Microfabrication," *Adv. Funct. Mater.*, vol. 18, no. 13, pp. 1912–1921, Jun. 2008.

[12] K. J. Lee, K. A. Fosser, and R. G. Nuzzo, "Fabrication of Stable Metallic Patterns Embedded in Poly(dimethylsiloxane) and Model Applications in Non-Planar

Electronic and Lab-on-a-Chip Device Patterning," *Adv. Funct. Mater.*, vol. 15, no. 4, pp. 557–566, Apr. 2005.

[13] S.-H. Hur, C. Kocabas, A. Gaur, O. O. Park, M. Shim, and J. A. Rogers, "Printed Thin-Film Transistors and Complementary Logic Gates that Use Polymer-Coated Single-Walled Carbon Nanotube Networks," *J. Appl. Phys.*, vol. 98, no. 11, pp. 114302–114302–6, Dec. 2005.

[14] S.-H. Hur, D.-Y. Khang, C. Kocabas, and J. A. Rogers, "Nanotransfer Printing by Use of Noncovalent Surface Forces: Applications to Thin-Film Transistors that Use Single-Walled Carbon Nanotube Networks and Semiconducting Polymers," *Appl. Phys. Lett.*, vol. 85, no. 23, pp. 5730 –5732, Dec. 2004.

[15] D.-H. Kim, N. Lu, R. Ma, Y.-S. Kim, R.-H. Kim, S. Wang, J. Wu, S. M. Won, H. Tao, A. Islam, K. J. Yu, T. Kim, R. Chowdhury, M. Ying, L. Xu, M. Li, H.-J. Chung, H. Keum, M. McCormick, P. Liu, Y.-W. Zhang, F. G. Omenetto, Y. Huang, T. Coleman, and J. A. Rogers, "Epidermal Electronics," *Sci.*, vol. 333, no. 6044, pp. 838–843, Aug. 2011.

[16] K. S. Lim, W.-J. Chang, Y.-M. Koo, and R. Bashir, "Reliable Fabrication Method of Transferable Micron Scale Metal Pattern for Poly(Dimethylsiloxane) Metallization," *Lab Chip*, vol. 6, no. 4, pp. 578–580, 2006.

[17] A. C. Siegel, D. A. Bruzewicz, D. B. Weibel, and G. M. Whitesides, "Microsolidics: Fabrication of Three-Dimensional Metallic Microstructures in Poly(dimethylsiloxane)," *Adv. Mater.*, vol. 19, no. 5, pp. 727–733, Mar. 2007.

[18] Y. J. Jung, S. Kar S. Talapatra, C. Soldano, S. Curran, and P. M. Ajayan, "Aligned Carbon Nanotube−Polymer Hybrid Architectures for Diverse Flexible Electronic Applications," *Nano Letters*, vol. 6, no. 3, pp. 413-418, Mar. 2006.

[19] M.-C. Choi, Y. Kim, and C.-S. Ha, "Polymers for Flexible Displays: from Material Selection to Device Applications," *Prog. Polym. Sci.*, vol. 33, no. 6, pp. 581–630, Jun. 2008.

[20] H. McKellop, R. Hoffmann, A. Sarmiento, and E. Ebramzadeh, "Control of Motion of Tibial Fractures with use of a Functional Brace or an External Fixator. a Study of Cadavera with Use of a Magnetic Motion Sensor," *J. Bone Joint Surg.*, vol. 75, no. 7, pp. 1019–1025, Jul. 1993.

[21] I. Kang, M. J. Schulz, J. H. Kim, V. Shanov, and D. Shi, "A Carbon Nanotube Strain Sensor for Structural Health Monitoring," *Smart Mater. Struct.*, vol. 15, no. 3, pp. 737–748, Jun. 2006.

[22] G. T. Pham, Y.-B. Park, Z. Liang, C. Zhang, and B. Wang, "Processing and Modeling of Conductive Thermoplastic/Carbon Nanotube Films for Strain Sensing," *Compos. B: Eng.*, vol. 39, no. 1, pp. 209–216, Jan. 2008.

[23] W. Zhang, J. Suhr, and N. Koratkar, "Carbon Nanotube/Polycarbonate Composites as Multifunctional Strain Sensors," *J. Nanosci. Nanotechnol.*, vol. 6, no. 4, pp. 960–964, Apr. 2006.

[24] F. Umbrecht, M. Wendlandt, D. Juncker, C. Hierold, and J. Neuenschwander, "A wireless implantable passive strain sensor system," in *Proceedings of the 2005 IEEE Sensors Conference*, Irvine, CA, 2005, pp. 20–23.

[25] Y. Liu, S. Chakrabartty, D. S. Gkinosatis, A. K. Mohanty, and N. Lajnef, "Multi-walled Carbon Nanotubes/Poly(L-lactide) Nanocomposite Strain Sensor for Biomechanical Implants," in *Proceedings of Biomedical Circuits and Systems Conference (IEEE BIOCAS 2007)*, Montreal, Que., 2007, pp. 119–122.

[26] K. Arshak and R. Perrem, "Fabrication of a Thin-Film Strain-Gauge Transducer Using Bi2O3-V2O5," *Sens. Actuators. A: Phys.*, vol. 36, no. 1, pp. 73–76, Mar. 1993.

[27] D. E. Hanson, M. Hawley, R. Houlton, K. Chitanvis, P. Rae, E. B. Orler, and D. A. Wrobleski, "Stress softening experiments in silica-filled polydimethylsiloxane provide insight into a mechanism for the Mullins effect," *Polymer*, vol. 46, no. 24, pp. 10989-10995, Nov. 2005.

[28] J. P. Heggers, N. Kossovsky, R. W. Parsons, M. C. Robson, R. P. Pelley, and T. J. Raine, "Biocompatibility of Silicone Implants," *Ann. Plast. Surg.*, vol. 11, no. 1, pp. 38–45, Jul. 1983.

[29] D. S. McLachlan, C. Chiteme, C. Park, K. E Wise, S. E. Lowther, P. T L., E. J. Siochi, J. S. Harrison, "AC and DC percolative conductivity of single wall carbon nanotube polymer composites," *Journal of Polymer Science Part B: Polymer Physics*, vol. 43, no. 22, pp. 3273-3287, Nov. 2005.

[30] S. Iijima, "Helical Microtubules of Graphitic Carbon," *Nature*, vol. 354, no. 6348, pp. 56–58, Nov. 1991.

[31] M. Trojanowicz, "Analytical Applications of Carbon Nanotubes: a Review," *Trends Anal. Chem.*, vol. 25, no. 5, pp. 480–489, May 2006.

[32] W. Bauhofer and J. Z. Kovacs, "A Review and Analysis of Electrical Percolation in Carbon Nanotube Polymer Composites," *Compos. Sci. Technol.*, vol. 69, no. 10, pp. 1486–1498, Aug. 2009.

[33] M.-F. Yu, O. Lourie, M. J. Dyer, K. Moloni, T. F. Kelly, and R. S. Ruoff, "Strength and Breaking Mechanism of Multiwalled Carbon Nanotubes Under Tensile Load," *Sci.*, vol. 287, no. 5453, pp. 637 –640, Jan. 2000.

[34] X. Zhao, Y. Ando, Y. Liu, M. Jinno, and T. Suzuki, "Carbon Nanowire Made of a Long Linear Carbon Chain Inserted Inside a Multiwalled Carbon Nanotube," *Phys. Rev. Lett.*, vol. 90, no. 18, p. 187401, May 2003.

[35] L. Bokobza, "Multiwall Carbon Nanotube Elastomeric Composites: A Review," *Polym.*, vol. 48, no. 17, pp. 4907–4920, Aug. 2007.

[36] Y. Huang and E. Terentjev, "Dispersion and Rheology of Carbon Nanotubes in Polymers," *Int. J. Mate. Form.*, vol. 1, no. 2, pp. 63–74, Jul. 2008.

[37] L. A. Girifalco, M. Hodak, and R. S. Lee, "Carbon Nanotubes, Buckyballs, Ropes, and a universal Graphitic Potential," *Phys. Rev. B*, vol. 62, no. 19, pp. 13104–13110, Nov. 2000.

[38] R. Andrews, D. Jacques, M. Minot, and T. Rantell, "Fabrication of Carbon Multiwall Nanotube/Polymer Composites by Shear Mixing," *Macromol. Mater. Eng.*, vol. 287, no. 6, pp. 395–403, Jun. 2002.

[39] H. Sato and M. Sano, "Characteristics of Ultrasonic Dispersion of Carbon Nanotubes Aided by Antifoam," *Colloids Surf., A*, vol. 322, no. 1–3, pp. 103–107, Jun. 2008.

[40] Y. A. Kim, T. Hayashi, Y. Fukai, M. Endo, T. Yanagisawa, and M. S. Dresselhaus, "Effect of Ball Milling on Morphology of Cup-Stacked Carbon Nanotubes," *Chem. Phys. Lett.*, vol. 355, no. 3–4, pp. 279–284, Apr. 2002.

[41] M. Inkyo, T. Tahara, T. Iwaki, F. Iskandar, C. J. Hogan Jr., and K. Okuyama, "Experimental Investigation of Nanoparticle Dispersion by Beads Milling with Centrifugal Bead Separation," *J. Colloid Interface Sci.*, vol. 304, no. 2, pp. 535–540, Dec. 2006.

[42] Y. Y. Huang, S. V. Ahir, and E. M. Terentjev, "Dispersion Rheology of Carbon Nanotubes in a Polymer Matrix," *Phys. Rev. B*, vol. 73, no. 12, p. 125422, Mar. 2006.

[43] T. P. Chua, M. Mariatti, A. Azizan, and A. A. Rashid, "Effects of Surface-Functionalized Multi-Walled Carbon Nanotubes on the Properties of Poly(dimethyl siloxane) Nanocomposites," *Compos. Sci. Technol.*, vol. 70, no. 4, pp. 671–677, Apr. 2010.

[44] J. Hong, J. Lee, C. K. Hong, and S. E. Shim, "Effect of Dispersion State of Carbon Nanotube on the Thermal Conductivity of Poly(dimethyl siloxane) Composites," *Curr. Appl. Phys.*, vol. 10, no. 1, pp. 359–363, Jan. 2010.

[45] R. R. Kohlmeyer, A. Javadi, B. Pradhan, S. Pilla, K. Setyowati, J. Chen, and S. Gong, "Electrical and Dielectric Properties of Hydroxylated Carbon Nanotube−Elastomer Composites," *J. Phys. Chem. C*, vol. 113, no. 41, pp. 17626–17629, Oct. 2009.

[46] J. Hwang, J. Jang, K. Hong, K. N. Kim, J. H. Han, K. Shin, and C. E. Park, "Poly(3-hexylthiophene) Wrapped Carbon Nanotube/Poly(Dimethylsiloxane) Composites for use in Finger-Sensing Piezoresistive Pressure Sensors," *Carbon*, vol. 49, no. 1, pp. 106–110, Jan. 2011.

[47] U. Subramanyam and J. P. Kennedy, "PVA Networks Grafted with PDMS Branches," *J. Polym. Sci., Part A: Polym. Chem.*, vol. 47, no. 20, pp. 5272–5277, Oct. 2009.

[48] R. C. Jaeger, "Introduction to Microelectronic Fabrication," in *Lithography*, Upper Saddle River: Prentice Hall, 2002.

[49] B. D. Gates, "Nanofabrication with Molds & Stamps," *Mater. Today*, vol. 8, no. 2, pp. 44–49, Feb. 2005.

[50] "Patterning Self-Assembled Monolayers : Applications in Materials Science." [Online]. Available: http://cat.inist.fr/?aModele=afficheN&cpsidt=4214666. [Accessed: 22-Apr-2011].

[51] Y. Xia, E. Kim, and G. M. Whitesides, "Microcontact Printing of Alkanethiols on Silver and Its Application in Microfabrication," *J. Electrochem. Soc.*, vol. 143, no. 3, pp. 1070–1079, Mar. 1996.

[52] A. P. Quist, E. Pavlovic, and S. Oscarsson, "Recent Advances in Microcontact Printing," *Anal. Bioanal. Chem.*, vol. 381, no. 3, pp. 591–600, Feb. 2005.

[53] H.-W. Li, B. V. O. Muir, G. Fichet, and W. T. S. Huck, "Nanocontact Printing: A Route to Sub-50-nm-Scale Chemical and Biological Patterning," *Langmuir*, vol. 19, no. 6, pp. 1963–1965, Mar. 2003.

[54] D. Li and L. J. Guo, "Micron-scale Organic Thin Film Transistors with Conducting Polymer Electrodes Patterned by Polymer Inking And Stamping," *Appl. Phys. Lett.*, vol. 88, no. 6, p. 063513, 2006.

[55] A. Benor, V. Wagner, and D. Knipp, "Microstructuring by Microcontact Printing and Selective Surface Dewetting," *J. Vac. Sci. Technol. B*, vol. 25, no. 4, p. 1321, 2007.

[56] H. Watanabe and M. Yamamoto, "Chemical Structure Change of a KRF-laser Irradiated PET Fiber Surface," *J. Appl. Polym. Sci.*, vol. 71, no. 12, pp. 2027–2031, Mar. 1999.

[57] H. Watanabe, T. Takata, and M. Tsuge, “Polymer Surface Modification due to Excimer Laser Radiation—Chemical and Physical Changes in the Surface Structure of Poly(ethylene terephthalate),” *Polym. Int.*, vol. 31, no. 3, pp. 247–254, 1993.

[58] D. L. Pugmire, E. A. Waddell, R. Haasch, M. J. Tarlov, and L. E. Locascio, “Surface Characterization of Laser-Ablated Polymers Used for Microfluidics,” *Anal. Chem.*, vol. 74, no. 4, pp. 871–878, Feb. 2002.

[59] C.-X. Liu and J.-W. Choi, “An Embedded PDMS Nanocomposite Strain Sensor Toward Biomedical Applications,” in *Proceedings of the 31st Annual International Conference of the IEEE Engineering in Medicine and Biology Society*, Minneapolis, MN, 2009, pp. 6391–6394.

[60] P. Sheng, E. K. Sichel, and J. I. Gittleman, “Fluctuation-Induced Tunneling Conduction in Carbon-Polyvinylchloride Composites,” *Phys. Rev. Lett.*, vol. 40, no. 18, p. 1197, May 1978.

[61] J. Gragg, Jr., “Silicon pressure sensor,” U.S. Patent 431712623-Feb-1982.

[62] D. W. Burns, “Piezoresistive Silicon Pressure Sensor Implementing Long Diaphragms with Large Aspect Ratios,” U.S. Patent 548575323-Jan-1996.

[63] A. Kulkarni, H. Kim, J. Choi, and T. Kim, “A Novel Approach to Use of Elastomer for Monitoring of Pressure Using Plastic Optical Fiber,” *Rev. Sci. Instrum.*, vol. 81, no. 4, p. 045108, 2010.

[64] D.-W. Lee and Y.-S. Choi, “A Novel Pressure Sensor with a PDMS Diaphragm,” *Microelectron. Eng.*, vol. 85, no. 5–6, pp. 1054–1058, May 2008.

[65] H. C. Lim, B. Schulkin, M. J. Pulickal, S. Liu, R. Petrova, G. Thomas, S. Wagner, K. Sidhu, and J. F. Federici, “Flexible Membrane Pressure Sensor,” *Sens. Actuators, A: Phys.*, vol. 119, no. 2, pp. 332–335, Apr. 2005.

[66] Q. Lü, H. Cao, X. Song, H. Yan, Z. Gan, and S. Liu, “Improved Electrical Resistance-Pressure Strain Sensitivity of Carbon Nanotube Network/Polydimethylsiloxane Composite Using Filtration and Transfer Process,” *Chin. Sci. Bull.*, vol. 55, no. 3, pp. 326–330, Jan. 2010.

[67] C. Gau, H. S. Ko, and H. T. Chen, “Piezoresistive Characteristics of MWNT Nanocomposites and Fabrication as a Polymer Pressure Sensor,” *Nanotechnology*, vol. 20, no. 18, p. 185503, May 2009.

[68] J. H. Kang, C. Park, J. A. Scholl, A. H. Brazin, N. M. Holloway, J. W. High, S. E. Lowther, and J. S. Harrison, “Piezoresistive Characteristics of Single Wall Carbon Nanotube/Polyimide Nanocomposites,” *J. Polym. Sci., Part B: Polym. Phys.*, vol. 47, no. 16, pp. 1635–1636, Aug. 2009.

[69] X. Yu and E. Kwon, "A Carbon Nanotube/Cement Composite with Piezoresistive Properties," *Smart Mater. Struct.*, vol. 18, no. 5, p. 055010, May 2009.

[70] H. Koerner, G. Price, N. A. Pearce, M. Alexander, and R. A. Vaia, "Remotely Actuated Polymer Nanocomposites—Stress-Recovery of Carbon-Nanotube-Filled Thermoplastic Elastomers," *Nat. Mater.*, vol. 3, no. 2, pp. 115–120, Feb. 2004.

[71] S. Sang and H. Witte, "Fabrication of a Surface Stress-Based PDMS Micro-Membrane Biosensor," *Microsyst. Technol.*, vol. 16, no. 6, pp. 1001–1008, Apr. 2010.

[72] Q. Cao, H. Kim, N. Pimparkar, J. P. Kulkarni, C. Wang, M. Shim, K. Roy, M. A. Alam, and J. A. Rogers, "Medium-Scale Carbon Nanotube Thin-Film Integrated Circuits on Flexible Plastic Substrates," *Nature*, vol. 454, no. 7203, pp. 495–500, Jul. 2008.

[73] H. Cao, Q. Lü, X. Song, Z. Gan, and S. Liu, "Fabrication and Characterization of Patterned Carbon Nanotube Flow Sensor Cell," *Chin. Sci. Bull.*, vol. 55, no. 23, pp. 2579–2583, Aug. 2010.

[74] Y. Zhao and X. Zhang, "A Novel Pressure Indicator for Continuous Flow PCR Chip Using Micro Molded PDMS Pillar Arrays," in *Proceedings of Materials Research Society Symposium*, 2005, pp. 845 AA5.10.1–AA5.10.6.

[75] H. Cao, Z. Gan, Q. Lv, H. Yan, X. Luo, X. Song, and S. Liu, "Single-Walled Carbon Nanotube Network/Poly Composite Thin Film for Flow Sensor," *Microsyst. Technol.*, vol. 16, no. 6, pp. 955–959, Jun. 2010.

[76] T. H. Kim, D.-K. Kim, and S. J. Kim, "Study of the Sensitivity of a Thermal Flow Sensor," *Int. J. Heat Mass Transfer*, vol. 52, no. 7–8, pp. 2140–2144, Mar. 2009.

[77] B. Pradhan, K. Setyowati, H. Liu, D. H. Waldeck, and J. Chen, "Carbon Nanotube−Polymer Nanocomposite Infrared Sensor," *Nano Lett.*, vol. 8, no. 4, pp. 1142–1146, Apr. 2008.

[78] W.-S. Jou, H.-Z. Cheng, and C.-F. Hsu, "The Electromagnetic Shielding Effectiveness of Carbon Nanotubes Polymer Composites," *J. Alloys Compd.*, vol. 434–435, pp. 641–645, May 2007.

[79] P. M. Ajayan and J. M. Tour, "Materials Science: Nanotube composites," *Nature*, vol. 447, no. 7148, pp. 1066–1068, Jun. 2007.

[80] "Multi-Walled Nanotubes-MWCNTs 20-30nm Specifications (Cheaptubes)." [Online]. Available: http://www.cheaptubesinc.com/MWNTs.htm#multi_walled_nanotubes-mwnts-20-30nm_specifications. [Accessed: 02-May-2011].

[81] S.-M. Yuen, C.-C. M. Ma, Y.-Y. Lin, and H.-C. Kuan, "Preparation, morphology and properties of acid and amine modified multiwalled carbon nanotube/polyimide composite," *Compos. Sci. Technol.*, vol. 67, no. 11–12, pp. 2564–2573, Sep. 2007.

[82] A. Beigbeder, M. Linares, M. Devalckenaere, P. Degée, M. Claes, D. Beljonne, R. Lazzaroni, and P. Dubois, "CH-π Interactions as the Driving Force for Silicone-Based Nanocomposites with Exceptional Properties," *Adv. Mater.*, vol. 20, no. 5, pp. 1003–1007, 2008.

[83] J. C. Kearns and R. L. Shambaugh, "Polypropylene Fibers Reinforced with Carbon Nanotubes," *J. Appl. Polym. Sci.*, vol. 86, no. 8, pp. 2079–2084, Nov. 2002.

[84] A. Mohraz, D. B. Moler, R. M. Ziff, and M. J. Solomon, "Effect of Monomer Geometry on the Fractal Structure of Colloidal Rod Aggregates," *Phys. Rev. Lett.*, vol. 92, no. 15, p. 155503, Apr. 2004.

[85] D. Fry, T. Sintes, A. Chakrabarti, and C. M. Sorensen, "Enhanced Kinetics and Free-Volume Universality in Dense Aggregating Systems," *Phys. Rev. Lett.*, vol. 89, no. 14, p. 148301, 2002.

[86] E. K. Hobbie, "Metastability and Depletion-Driven Aggregation," *Phys. Rev. Lett.*, vol. 81, no. 18, p. 3996, Nov. 1998.

[87] S. Lin-Gibson, G. Schmidt, H. Kim, C. C. Han, and E. K. Hobbie, "Shear-Induced Mesostructure in Nanoplatelet-Polymer Networks," *J. Chem. Phys.*, vol. 119, no. 15, p. 8080, 2003.

[88] P. T. Lillehei, J.-W. Kim, L. J. Gibbons, and C. Park, "A Quantitative Assessment of Carbon Nanotube Dispersion in Polymer Matrices," *Nanotechnology*, vol. 20, no. 32, p. 325708, Aug. 2009.

[89] L. L. Lebel, B. Aissa, M. A. E. Khakani, and D. Therriault, "Preparation and Mechanical Characterization of Laser Ablated Single-Walled Carbon-Nanotubes/Polyurethane Nanocomposite Microbeams," *Compos. Sci. Technol.*, vol. 70, no. 3, pp. 518–524, Mar. 2010.

[90] C.-X. Liu and J.-W. Choi, "Conductive and Flexible Nanocomposite Patterns Embedded in Elastomer Using Microcontact Printing and Cast Molding," in *Proceedings of 12th International Conference on Miniaturized Systems for Chemistry and Life Sciences (μTAS)*, San Diego, CA, 2008, pp. 1645–1647.

[91] B. Lundberg and B. Sundqvist, "Resistivity of a Composite Conducting Polymer as a Function of Temperature, Pressure, and Environment: Applications as a Pressure and Gas Concentration Transducer," *J. Appl. Phys.*, vol. 60, no. 3, p. 1074, 1986.

[92] Junyong Lu, Miao Lu, A. Bermak, and Yi-Kuen Lee, "Study of piezoresistance effect of carbon nanotube-PDMS composite materialsStudy of Piezoresistance Effect of Carbon Nanotube-PDMS Composite Materials for Nanosensors for nanosensors," in *Proceedings of the 7th IEEE Conference on Nanotechnology (IEEE-NANO 2007)*, Hong Kong, 2007, pp. 1240–1243.

[93] L. F. C. Pereira, C. G. Rocha, A. Latgé, J. N. Coleman, and M. S. Ferreira, "Upper bound for the conductivity of nanotube networks," *Appl. Phys. Lett.*, vol. 95, no. 12, pp. 123106–123106–3, Sep. 2009.

[94] A. Aldalbahi, J. Chu, P. Feng, and M. in het Panhuis, "Conducting composite materials from the biopolymer kappa-carrageenan and carbon nanotubes," *Beilstein Journal of Nanotechnology*, vol. 3, pp. 415–427, May 2012.

[95] S. Bianco, P. Ferrario, M. Quaglio, R. Castagna, and C. Fabrizio, "Nanocomposites based on elastomeric matrix filled with carbon nanotubes for biological applications," in *Carbon Nanotubes - From Research to Applications*, S. Bianco, Ed. InTech, 2011.

[96] C. -X. Liu and J. -W. Choi, "Strain-Dependent Resistance of PDMS and Carbon Nanotubes Composite Microstructures," *Nanotechnology, IEEE Transactions on*, vol. 9, no. 5, pp. 590-595, 2010.

[97] C.-X. Liu and J.-W. Choi, "Patterning conductive PDMS nanocomposite in an elastomer using microcontact printing," *J. Micromech. Microeng.*, vol. 19, no. 8, p. 085019, Aug. 2009.

[98] F. R. Wagner, *Scanning Excimer Laser Ablation of Poly(ethylene terephthalate) (PET) and its Application to Rapid Prototyping of Channels for Microfluidics*. Lausanne: EPFL, 2000.

[99] F. Wagner and P. Hoffmann, "Structure Formation in Excimer Laser Ablation of Stretched Poly(ethylene therephthalate) (PET): the Influence of Scanning Ablation," *Appl. Phys. A: Mater. Sci. Process.*, vol. 69, no. 7, pp. S841–S844, Dec. 1999.

[100] M. Ebara, J. M. Hoffman, A. S. Hoffman, and P. S. Stayton, "Switchable Surface Traps for Injectable Bead-Based Chromatography In PDMS Microfluidic Channels," *Lab Chip*, vol. 6, no. 7, pp. 843–848, May 2006.

[101] E. Miyako, H. Nagata, K. Hirano, and T. Hirotsu, "Laser-Triggered Carbon Nanotube Microdevice for remote Control of Biocatalytic Reactions," *Lab Chip*, vol. 9, no. 6, pp. 788–794, 2009.

[102] R. Turner, Y. Desta, K. Kelly, J. Zhang, E. Geiger, S. Cortez, and D. C. Mancini, "Tapered LIGA HARMs," *J. Micromech. Microeng.*, vol. 13, pp. 367–372, May 2003.

[103] C.-X. Liu and J.-W. Choi, "An Ultra-Sensitive Nanocomposite Pressure Sensor Patterned in a PDMS Diaphragm," in *Proceedings of the 16th International Solid-State Sensors, Actuators and Microsystems Conference (Transducers)*, 2011, pp. 2594–2597.

[104] H. Qi, X. Wang, T. Chen, X. Ma, and T. Zuo, "Fabrication and Characterization of a Polymethyl Methacrylate Continuous-Flow PCR Microfluidic Chip Using CO2 Laser Ablation," *Microsyst. Technol.*, vol. 15, no. 7, pp. 1027–1030, Apr. 2009.

[105] B. Li, T. Schwarz, and A. Sharon, "Implementation of Microfluidic Devices at a Transparency," *J. Micromech. Microeng.*, vol. 16, no. 12, pp. 2639–2645, Dec. 2006.

[106] H. Qi, Y. Liu, X. Wang, F. Shen, Y. Yu, T. Chen, and T. Zuo, "Micromachining of Passive Planar Micromixer on Poly (methyl methacrylate) Substrate with Excimer Laser Ablation," *Microsyst. Technol.*, vol. 15, no. 2, pp. 297–300, Jun. 2008.

[107] D. Snakenborg, H. Klank, and J. P. Kutter, "Microstructure Fabrication with a CO2 Laser System," *J. Micromech. Microeng.*, vol. 14, no. 2, pp. 182–189, Feb. 2004.

[108] W. Pfleging, W. Bernauer, T. Hanemann, and M. Torge, "Rapid Fabrication of Microcomponents - UV-Laser Assisted Prototyping, Laser Micro-Machining of Mold Inserts and Replication via Photomolding," *Microsyst. Technol.*, vol. 9, no. 1–2, pp. 67–74, Nov. 2002.

[109] H.-S. Chuang and S. T. Wereley, "Rapid Patterning of Slurry-Like Elastomer Composites Using a Laser-Cut Tape," *J. Micromech. Microeng.*, vol. 19, no. 9, p. 097001, Sep. 2009.

[110] L. W. Luo, C. Y. Teo, W. L. Ong, K. C. Tang, L. F. Cheow, and L. Yobas, "Rapid Prototyping of Microfluidic Systems Using a Laser-Patterned Tape," *J. Micromech. Microeng.*, vol. 17, no. 12, pp. N107–N111, Dec. 2007.

[111] J. S. Bergström and M. C. Boyce, "Large Strain Time-Dependent Behavior of Filled Elastomers," *Mech. Mater.*, vol. 32, no. 11, pp. 627–644, Nov. 2000.

[112] T. M. Junisbekov, V. N. Kestelman, and N. I. Malinin, *Stress Relaxation in Viscoelastic Materials*. Science Publishers, 2002.

[113] D. E. Hanson, "An Explicit Polymer and Node Network Model to Compute Micromechanical Properties of Silica-Filled Polydimethylsiloxane," *Polym.*, vol. 45, no. 3, pp. 1055–1062, Feb. 2004.

[114] R. D. Andrews, N. Hofman-Bang, and A. V. Tobolsky, "Elastoviscous Properties of Polyisobutylene. I. Relaxation of Stress in Whole Polymer of Different Molecular Weights at Elevated Temperatures," *J. Polym. Sci.*, vol. 3, no. 5, pp. 669–692, 1948.

[115] H. A. Barnes and G. P. Roberts, "The Non-Linear Viscoelastic Behaviour of Human Hair at Moderate Extensions," *Int. J. Cosmet. Sci.*, vol. 22, no. 4, pp. 259–264, Aug. 2000.

[116] R. N. Weltmann, "Breakdown of Thixotropic Structure as Function of Time," *J. Appl. Phys.*, vol. 14, no. 7, pp. 343 –350, Jul. 1943.

[117] H. S. Ramaswamy and S. Basak, "Time Dependent Stress Decay Rheology of Stirred Yogurt," *Int. Dairy J.*, vol. 2, no. 1, pp. 17–31, 1992.

[118] S. M. Clarke, F. Elias, and E. M. Terentjev, "Ageing of Natural Rubber Under Stress," *Eur. Phys. J. E Soft Matter.*, vol. 2, no. 4, pp. 335–341, 2000.

[119] M. Lagi, P. Baglioni, and S.-H. Chen, "Logarithmic Decay in Single-Particle Relaxations of Hydrated Lysozyme Powder," *Phys. Rev. Lett.*, vol. 103, no. 10, p. 108102, Aug. 2009.

[120] D. Shi and M. Xu, "Nonlinear Logarithmic Time Decay of Magnetization in a Single Crystal of Bi2Sr2CaCu2Ox," *Phys. Rev. B*, vol. 44, no. 9, pp. 4548–4552, 1991.

[121] A. V. Tobolsky, "Stress Relaxation Studies of the Viscoelastic Properties of Polymers," *J. Appl. Phys.*, vol. 27, no. 7, pp. 673 –685, Jul. 1956.

[122] J. S. Bergström and M. C. Boyce, "Constitutive Modeling of the Large Strain Time-Dependent Behavior of Elastomers," *J. Mech. Phys. Solids*, vol. 46, no. 5, pp. 931–954, May 1998.

[123] J. Yi, M. C. Boyce, G. F. Lee, and E. Balizer, "Large Deformation Rate-Dependent Stress–Strain Behavior of Polyurea and Polyurethanes," *Polym.*, vol. 47, no. 1, pp. 319–329, Jan. 2006.

[124] G. Kraus, C. W. Childers, and K. W. Rollmann, "Stress Softening in Carbon Black-Reinforced Vulcanizates. Strain Rate and Temperature Effects," *J. Appl. Polym. Sci.*, vol. 10, no. 2, pp. 229–244, Mar. 2003.

[125] S. S. Sarva, S. Deschanel, M. C. Boyce, and W. Chen, "Stress–Strain Behavior of a Polyurea and a Polyurethane From Low to High Strain Rates," *Polym.*, vol. 48, no. 8, pp. 2208–2213, Apr. 2007.

[126] G. Akay, "Non-Linear Creep of Polymers Under Superimposed Static and Dynamic Stress," *Polym. Eng. Sci.*, vol. 15, no. 11, pp. 811–816, Aug. 2004.

[127] H. . Le, T. Lüpke, T. Pham, and H.-J. Radusch, "Time Dependent Deformation Behavior of Thermoplastic Elastomers," *Polym.*, vol. 44, no. 16, pp. 4589–4597, Jul. 2003.

[128] W. Y. Zhang, G. S. Ferguson, and S. Tatic-Lucic, "Elastomer-supported cold welding for room temperature wafer-level bonding," in *Proceedings of the 17th IEEE International Conference on.Micro Electro Mechanical Systems (MEMS)* , 2004, pp. 741-744.

[129] J. H. Koschwanez, R. H. Carlson, and D. R. Meldrum, "Thin PDMS Films Using Long Spin Times or Tert-Butyl Alcohol as a Solvent," *PLoS ONE*, vol. 4, no. 2, p. e4572, Feb. 2009.

[130] C. Stampfer, T. Helbling, D. Obergfell, B. Scho1berle, M. K. Tripp, A. Jungen, S. Roth, V. M. Bright, and C. Hierold, "Fabrication of Single-Walled Carbon-Nanotube-Based Pressure Sensors," *Nano Letters*, vol. 6, no. 2, pp. 233-237, Feb. 2006.

[131] N. S. Tambe and B. Bhushan, "Micro/nanotribological characterization of PDMS and PMMA used for BioMEMS/NEMS applications," *Ultramicroscopy*, vol. 105, no. 1–4, pp. 238–247, Nov. 2005.

APPENDIX: LIST OF AUTHOR'S PUBLICATIONS

Journal papers:

1. C.-X. Liu and J.-W. Choi, "Improved dispersion of carbon nanotubes in polymers at high concentrations," *Nanomaterials*, in press.

2. C.-X. Liu and J.-W. Choi, "Embedding conductive patterns of elastomer nanocomposite with the assist of laser ablation," *Microsystems Technologies*, vol. 18, no. 3, pp. 365-371, 2012.

3. C.-X. Liu and J.-W. Choi, "Precision patterning of conductive polymer nanocomposite using a laser-ablated thin film," *Journal of Micromechanics and Microengineering*, vol. 22, no. 4, 045014 (7pp), 2012.

4. C.-X. Liu and J.-W. Choi, "Strain-dependent resistance of PDMS and carbon nanotubes composite microstructures," *IEEE Transaction on Nanotechnology*, vol. 9, issue 5, pp. 590-595, 2010.

5. C.-X. Liu and J.-W. Choi, "Patterning conductive PDMS nanocomposite in an elastomer using microcontact printing," *Journal of Micromechanics and Microengineering*, vol. 19, no. 8, 085019 (7pp), 2009.

6. C.-X. Liu, J. Park, and J.-W. Choi, "A planar lens based on electrowetting of two immiscible liquids," *Journal of Micromechanics and Microengineering*, vol. 18, no. 3, 035023 (7pp), 2008.

Conference proceedings:

7. C.-X. Liu and J.-W. Choi, "An ultra-sensitive nanocomposite pressure sensor patterned in a PDMS diaphragm," in *Technical Digest of the 16th International Conference onSolid-State Sensors, Actuators and Microsystems (Transducers 2011)*, Beijing, China, Jun 5-9, 2011, pp. 2594-2597.

8. C.-X. Liu and J.-W. Choi, "An embedded PDMS nanocomposite strain sensor toward biomedical applications," in *Proceedings of the 31th International Conference of the IEEE Engineering in Medicine and Biology Society (EMBC '09)*, Minneapolis, MN, Sep. 2-6, 2009, pp. 6391-6394.

9. C.-X. Liu and J.-W. Choi, "Conductive and flexible nanocomposite patterns embedded in elastomer using microcontact printing and cast molding," in *Proceedings of the 12th International Conference on Miniaturized Systems for Chemistry and Life Sciences (μTAS 2008)*, San Diego, CA, Oct. 12-16, 2008, pp. 1645-1647.

10. J. Park, C.-X. Liu, and J.-W. Choi, "A planar liquid lens design based on electrowetting," in *Proceedings of IEEE Sensors Conference*, Atlanta, GA, Oct. 28-31, 2007, pp. 439-442.

Conference abstracts:

11. C.-X. Liu and J.-W. Choi, "Micropatterned elastomer nanocomposite for sensor applications," *11th International Conference on Electronics, Information, and Communication (ICEIC 2012)*, Jeongseon, Korea, Feb 1-3, 2012.

12. C.-X. Liu and J.-W. Choi, "Microfabrication of conductive polymer nanocomposite for novel sensor applications," *2011 Sigma Xi Annual Meeting and International Research Conference*, Raleigh, NC, Nov. 10-13, 2011.

13. C.-X. Liu and J.-W. Choi, "Patterning of elastomer nanocomposite via laser for sensor applications," *2010 Material Research Society Fall Meeting (MRS)*, Boston, MA, Nov. 29-Dec. 3, 2010.

14. J.-W. Choi and C.-X. Liu, "A polymer nanocomposite microstructure for strain and pressure sensing," *Nanoelectronic Devices for Defense and Security Conference (NANO DDS)*, Lauderdale, FL, Sep 28 - Oct 2, 2009.

Patent related:

15. J.-W. Choi and C.-X. Liu, "Apparatus and method for nanocomposite sensors," WIPO Patent Application WO/2011/041507.

16. J.-W. Choi and C.-X. Liu, "Remote control of localized temperature via carbon based composite," invention disclosed on 4/11/2012.

VITA

Chaoxuan Liu was born in Hunan, China. He received his B.E. degree in control science and engineering from the Huazhong University of Science and Technology, Wuhan, China in 2006. He entered the doctoral program in the Department of Electrical and Computer Engineering at Louisiana State University in 2006. He obtained his Master of Science degree in electrical engineering in 2008. His research interests include micro/nano technology, carbon nanotube-based polymer nanocomposites, and physical sensors. He is expected to earn the degree of Doctor of Philosophy in December 2012.